POLITECNICO DI TORINO

Master's Degree in Biomedical Engineering

Master's Degree Thesis

Non-Rigid Motion Correction for the Walk-Through PET: A Data Driven Approach with Digital XCAT Phantom

Supervisors

Prof. Kristen M. MEIBURGER

Prof. dr. Stefaan VANDENBERGHE

Prof. dr. Christian VANHOVE

Ir. Rabia AZIZ

Dr. ir. Jens MAEBE

Candidate

Alessia TRIVISONNO

April 2026

Declaration on the use of AI tools

During the writing of this master's thesis, generative AI tools (specifically ChatGPT by OpenAI) were used for stylistic and linguistic refinement, paraphrasing suggestions, and academic tone adjustment. These tools were not used to generate technical content or data analysis. All scientific reasoning, results, and conclusions presented are my own original work.

Turin, 1 April 2026

Acknowledgments

Having reached the end of this journey, I feel both the duty and the pleasure of thanking all the people and institutions that made the realization of this thesis possible and who accompanied me throughout these intense months.
First, I would like to thank Prof. Kristen Mariko Meiburger for accepting my request to be my internal supervisor and for giving me the possibility to carry out my thesis abroad. Her trust was the starting point of this experience.
A heartfelt thanks goes to Ghent University for offering me the unique opportunity to work on a thesis project abroad. It was an extraordinary academic and human experience that has deeply enriched my personal and educational path. I will carry this experience with me forever. I would like to express my sincere gratitude to Prof. Stefaan Vandenberghe for welcoming me into his research group and allowing me to take part in this project, despite coming from another university. His support was essential at the start of this journey. A special thanks goes to Rabia and Jens, who were constant guides throughout these ten months of work. When I arrived, I had limited practical knowledge, but thanks to your guidance and availability, I was able to grow and gain new skills. I am grateful to you both for giving me the autonomy to work independently, while also being present whenever I needed support, especially during the thesis writing phase.

Abstract

The dual flat-panel Walk-Through PET (WT-PET), recently proposed by the MEDISIP group at Ghent University, offers high throughput, simplified setup, reduced personnel workload, and higher spatial resolution compared to conventional cylindrical PET scanners. In the WT-PET, patients stand upright between two detector panels, which may lead to increased motion.

Understanding motion patterns during WT-PET imaging is essential for improving image quality and diagnostic accuracy. This motion can be broadly divided into rigid motion that is characterized by rotations or translations such as head motion, and non-rigid motion that involves more complex movements such as twisting or bending such as respiratory and cardiac motion. This non-rigid motion is crucial to address because it leads to a loss of image quality and can induce artifacts.

A motion compensation method has been adopted to maintain high image resolution and compensate for these artifacts. Motion correction is obtained by non-rigid coregistration of short time-frame reconstructions, superimposing them on each other to obtain a motion-free image. This model uses data from GATE Monte Carlo simulation of digital anthropomorphic XCAT phantoms. Image reconstruction is performed using PETRecon, an in-house image reconstruction framework. The reconstructed frames are aligned with Advanced Normalization Tools (ANTs) and evaluated with AMIDE.

Several metrics for lesion detectability such as Contrast-to-Noise ratio (CNR), Contrast Recovery Coefficient (CRC), and the volume of the lesions in the liver and lungs were analyzed to quantify the effectiveness of the co-registration method. This confirms an improvement in the visualization of the lesions compared to the image without motion correction, also confirmed by the better quality of the images observed visually.

Keywords: Walk-Through PET, motion correction, non-rigid co-registration

Non-Rigid Motion Correction for the Walk-Through PET: A Data-Driven Approach with Digital XCAT Phantoms

Alessia Trivisonno, Rabia Aziz, Jens Maebe, Stefaan Vandenberghe, Christian Vanhove

Abstract - **The dual flat-panel Walk-Through PET (WT-PET), recently proposed by the MEDISIP group at Ghent University, offers high throughput, simplified setup, reduced personnel workload, and higher spatial resolution compared to conventional cylindrical PET scanners. In the WT-PET, patients stand upright between two detector panels, which may lead to increased motion. Understanding motion patterns during WT-PET imaging is essential for improving image quality and diagnostic accuracy. This motion can be broadly divided into rigid motion that is characterized as rotations or translations such as head motion, and non-rigid motion that involves more complex movements such as twisting or bending such as respiratory and cardiac motion. This non-rigid motion is crucial to address because it leads to a loss of image quality and can induce artifacts. A motion compensation method has been adopted to maintain high image resolution and compensate for these artifacts. Motion correction is obtained by non-rigid coregistration of short time-frame reconstructions, superimposing them on each other to obtain a motion-free image. This model uses data from GATE Monte Carlo simulation of digital anthropomorphic XCAT phantoms. Image reconstruction is performed using PETRecon, an in-house image reconstruction framework. The reconstructed frames are aligned with Advanced Normalization Tools (ANTs) and evaluated with AMIDE. Several metrics for lesion detectability such as Contrast-to-Noise ratio (CNR), Contrast Recovery Coefficient (CRC), and the volume of the lesions in the liver and lungs were analyzed to quantify the effectiveness of the co-registration method. This confirms an improvement in the visualization of the lesions compared to the image without motion correction, also confirmed by the better quality of the images observed visually.**

Keywords - **Walk-Through PET, motion correction, non-rigid co-registration**

INTRODUCTION

Positron Emission Tomography

Positron Emission Tomography (PET) is a medical imaging technique that allows the visualization of metabolic processes within the human body. PET plays a crucial role in medical diagnostics, particularly in oncology to detect tumors, assess disease progression, and evaluate the effectiveness of radiotherapy treatments [1].

To visualize functional processes in the body, PET imaging relies on a radiotracer, a biologically active molecule labeled with a positron-emitting radioisotope injected into the patient. After the injection, the radioactive tracer causes the emission of a positron, which interacts with a nearby electron, resulting in an annihilation event. This event generates two antiparallel gamma photons of 511 keV energy each. The PET scanner detects both photons in coincidence, forming a line of response (LOR) along which the annihilation event occurred. By combining many LORs, an image of the radiotracer distribution is reconstructed through image reconstruction algorithms. Modern improvements, such as Time-of-Flight (TOF) information, allow a better localization of the annihilation point, enhancing signal-to-noise ratio (SNR) in the final image [2].

Despite advancements in detector technology and system design, the image quality of PET is compromised by some degrading effects. These include photon attenuation within body tissue, scattered and random coincidences, introducing background noise and reducing the quantitative accuracy [3]. Finally, the limited intrinsic resolution of the detectors contributes to a degradation of the system's spatial resolution and overall image quality [4].

The current standard for PET imaging is iterative reconstruction, which produces higher quality images compared to analytical methods such as Filtered BackProjection (FBP). The most used iterative method in PET is the Maximum Likelihood Expectation Maximization (MLEM), which iteratively updates the image estimate by comparing measured and estimated projections. Image degrading effects such as attenuation, random and scattered coincidences, and the non-uniform response of PET detectors are compensated during the image reconstruction [3].

Short Axial Field-of-View PET

The earliest PET scanner was an axial ring that requires rotation around the patient to acquire a 3D image. Later, the number of detectors increased to form a full ring. Early clinical scanners featured a short axial field of view (AFOV) of 15–25 cm, also known as SAFOV, and included a limited number of detectors.

Long Axial Field-of-View PET

New technologies have been developed to increase the number of detectors, extending the scanner to a long AFOV (LAFOV) up to 106 cm. The extended AFOV enables imaging of large body areas in a single bed position. It offers improved sensitivity, image quality, and lesion quantification, allowing faster scans. Although patient acquisition time can be done in 30 s to 2 minutes, the time to position the patient on/off the bed is longer [5]. This reduces patient throughput and increases personnel workload, resulting in higher costs.

Walk-Through PET

To address these limitations, a novel approach has been proposed by the MEDISIP Group at Ghent University: the Walk-Through PET (WT-PET). The design of the WT-PET requires the patient to be scanned while standing for 30 to 60 seconds. The scanner configuration consists of two flat panels

of dimensions of 70 cm wide and 106 cm high, with a gap of 50 cm between the two panels (see Figure 1). Each panel is composed of 12 × 14 array of monolithic Lutetium–yttriumoxyorthosilicate (LYSO) detector blocks with dimensions of 16 x 50 x 50 mm^3 and coupled to an 8 × 8 array of 6 × 6 mm^2 silicon photomultipliers (SiPMs). Monolithic detectors provide better spatial resolution and depth-of-interaction (DOI) information compared to pixelated detectors, enabling detectors to be placed closer, which in turn improves system sensitivity by reducing the probability that emitted gamma photons miss the scanner.

Initially, the system used monolithic BGO (Bismuth Germanate) detectors arranged in a 14 × 20 array. BGO is cheap and has high stopping power but does not generally support TOF capability. To reduce costs when switching to LYSO detectors, gaps were introduced between detector rows, reducing the array to 12 × 14 while maintaining the same panel spacing. Although LYSO has lower sensitivity than BGO, its TOF capability compensates for this, keeping overall performance high and costs comparable. The main advantage of WT-PET design is the reduced total scanning procedure (around 5 minutes) compared to both SAFOV and LAFOV systems. This leads to a higher patient throughput and a reduced personnel workload [6].

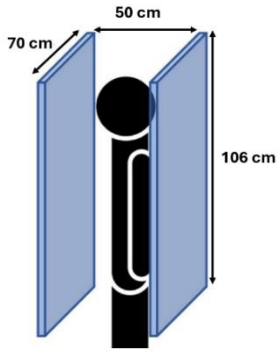

Figure 1: The WT-PET design and panel dimensions

Motion Artifacts in PET

One of the major sources of artifacts in PET imaging is patient motion, which reduces the image quality and diagnostic accuracy. Both voluntary movements, such as upper and lower limb motion controlled by the motor cortex, and involuntary movements, such as respiratory and cardiac motion, can cause blurring and distortion in the final image, compromising the visualization of lesions and anatomical structures. Several motion compensation techniques have been developed to address these artifacts, broadly classified into hardware-based and data-driven approaches. Hardware-based methods use external devices to track body movement. Examples include camera systems for recording markers placed on the patient's body, respiratory belts that measure thoracic expansion and contraction during breathing, and temperature sensors that detect breathing cycles by measuring the difference in air temperature during inhalation and exhalation. The advantage of these methods is the ability to monitor tracking in real time, but they are unable to monitor internal organ motion effectively, making them less suitable for tracking respiratory or cardiac motion. For this reason, data-driven methods have been developed. The key advantage of these approaches is that they rely solely on PET data to identify and correct motion patterns, eliminating the need for additional hardware. This makes them more affordable and flexible [7, 8]. One of the most widely used data-driven techniques is image registration. This method aligns two images into a common coordinate system by determining a geometrical transformation that maps points from one image to another. Figure 2 shows the image registration workflow, including the data acquisition, the reconstruction in short temporal frames, and the registration to a common reference frame.

There are different types of transformation, primarily classified as rigid or non-rigid, depending on the nature of the motion to be corrected. Rigid registration involves only rotations and translations without any internal deformation of the anatomical structures. This type of registration is preferable when the aim is to align bone structures and rigid objects without changing their shape. The second approach, which is the one implemented in this work, is non-rigid registration. This technique is ideal for modeling the motion of internal organs involving compression, bending and warping. It uses a local deformation field, dynamically changing the position of each point in the image, making the registration more flexible. Non-rigid registration is particularly effective for correcting respiratory and cardiac motion, allowing accurate tracking [9].

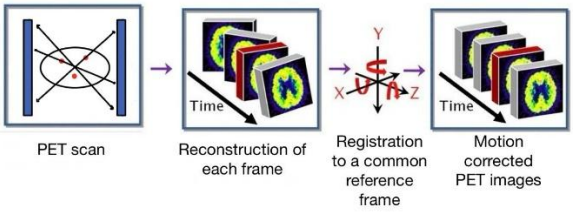

Figure 2: Image Registration workflow

In this work, the main tools adopted to perform image registration were MRtrix3 and ANTs (Advanced Normalization Tools). Both implement symmetric diffeomorphic registration to map moving images to a reference template or vice versa. However, while both frameworks apply this concept, ANTs specifically employs the Symmetric Normalization (SyN) algorithm for its registration process [10, 11].

In the present study, although MRtrix3 was initially used, a transition to ANTs was made due to its higher computational efficiency. In fact, while MRtrix3 took 15 minutes to align two PET images of size (350, 200, 500), ANTs required a significantly shorter time, 1-2 minutes.

The motion correction pipeline developed in this thesis addresses motion artifacts caused by respiration and cardiac activity by applying non-rigid registration between frames from a dynamic PET acquisition.

METHODS

PET Data Simulation

The first step of the motion correction workflow is the simulation of $^{18}F-FDG$ (fluorodeoxyglucose) PET data, performed on GATE (GEANT4Application for Tomographic Emission) software using Monte Carlo simulations. This provides a flexible and complete environment for realistic PET simulation, including physical models, geometric modeling tools, and innovative features such as the synchronization of all time-dependent components and source kinetic decay, allowing a more realistic description of the acquisition process [12].

In this study, GATE was used to simulate 60 seconds of PET data acquisition, modeling scenarios with and without respiratory and cardiac motion. The simulations were

conducted using anthropomorphic XCAT phantoms, whose activity distribution is based on $^{18}\mathrm{F}-\mathrm{FDG}$. The phantoms differ in age, weight, height, and sex, and are classified based on the Body Mass Index (BMI). They are referred to as:
- Low BMI phantom (BMI 18.64)
- Medium BMI phantom (BMI 28.22)
- High BMI phantom (BMI 37.96)
Initially, simulations were analyzed without lesions, both in static and in respiratory and cardiac motion-affected scenarios. Subsequently, four lesions of 10 mm diameter (two in the lungs and two in the liver) were inserted into each phantom for further analysis. The simulated PET data was provided as part of the available dataset.

Image Reconstruction

The second step involves PET image reconstruction. In common reconstruction algorithms, the configuration of scanners with particular geometry is difficult to achieve. Therefore, the Ghent research group developed a custom image reconstruction framework, PETRecon, written in Julia, offering high performance and efficiency. PETRecon models the complex geometry of the Walk-Through PET system using a system response matrix that incorporates geometric sensitivity, TOF, attenuation, and normalization factors. The image reconstruction is performed using the MLEM algorithm, applied to the list-mode data generated in the simulation phase. A voxel size of $2 \times 2 \times 2$ mm³ is used, and the number of iterations is set to 5. In order to evaluate the effectiveness of motion correction, multiple reconstruction strategies were implemented, differing in acquisition duration and temporal frame segmentation:
- Full 60 seconds: all data acquired in the interval 0-60 s are reconstructed in a single frame.
- Stride of 0.3125 s: data are reconstructed into consecutive frames, each of duration 0.3125 s. (e.g., 0–0.3125 s, 0.3125–0.625 s, etc.).
- Stride of 0.9375 s: frames are separated by 0.9375 s.
- Stride of 0.3125 seconds with frame length of 0.9375 s: overlapping frames of 0.9375 s are generated every 0.3125 s, resulting in temporal overlap across frames.

Motion Correction

The third step concerns the motion correction performed in ANTs. The underlying process of co-registration is as follows: reconstructed short-time frames are non-rigidly aligned to a reference frame using the Symmetric Normalization (SyN) algorithm. The reference frame is chosen corresponding to time 0 s, while all subsequent images are considered the moving images. For example, in the reconstruction with a frame length of 0.9375 s, the alignment proceeds as follows: the frame acquired at 0.9375 s is registered with respect to the frame at 0 s; the next frame (at 1.875 s) is registered to the frame 0s; and so forth. Following the co-registration, a series of spatially transformed images is obtained. Subsequently, the voxel-wise mean of the series of these corrected images is calculated.

Visualization in AMIDE

The 3D images obtained by averaging the reconstructed short-time frames were visualized using AMIDE (Amide's a Medical Image Data Examiner), an open-source software developed for the analysis of multimodal volumetric medical images, such as PET, CT (Computed Tomography), MRI (Magnetic Resonance Imaging). AMIDE was chosen for its simple and intuitive interface, the simultaneous visualization of multiple data sets, and the Region of Interest (ROI) selection functionality, useful for isolating specific lesions and conducting a detailed quantitative analysis [13]. The images were saved in NIfTI (Neuroimaging Informatics Technology Initiative) format and then were loaded into the software and displayed in transverse, coronal, and sagittal projections. It was also possible to compare different reconstructions by displaying images side by side, thus facilitating data interpretation.

Lesion Analysis

Among the datasets simulated using GATE Monte Carlo, there are cases with four thoracic lesions distributed in two anatomical locations: two in the right lung and two in the liver. The lesions are modeled as spheres of 10 mm diameter with tumor-to-background activity concentration ratio of 8:1. To characterize the lesions, image segmentation is fundamental. It consists of discerning the objects from the background, dividing the images into different regions, each with certain characteristics. This study adopts the region growing algorithm, a technique based on the selection of a seed point from which the algorithm starts. A pixel near the seed point is added to the region if it satisfies a similarity criterion. The growth of the regions ends when there are no more pixels to add [14, 15]. In this study, the region growing algorithm, implemented in Python, was applied to the resulting reconstructed images after being filtered with a median filter. Lesion segmentation was performed by first selecting a seed point based on statistical descriptions (such as maximum, mean, standard deviation) extracted from elliptical ROIs defined around each lesion using AMIDE. More in detail, the dimensions of the ROIs varied from 25-30 mm for images without motion correction to 15-20 mm for images with motion correction. For the liver, the seed point was automatically selected as the voxel with intensity equal to the maximum value of the ROI, limiting the search to the central portion of the image, anatomically corresponding to the thorax area. Region-growing was performed using 6-connectivity, with a threshold between 50%–80% of the ROI maximum. These threshold values were chosen manually for each lesion by visually ensuring that the resulting ROI accurately matched the lesion boundaries and by examining the line profiles across the lesion to better capture intensity variations. A voxel limit of 50,000 was set to prevent over-segmentation. For lung lesions, the seed point was selected as the voxel with maximum intensity within a 20-voxel radius from the lesion's location at instant 0 s, with a lower threshold of 40%. The process was repeated for all four lesions in each dataset, producing binary masks that reflect lesion volumes, which are larger in the presence of motion artifacts.

Three quantitative metrics are analysed on the lesion masks obtained from the region growing algorithm. The first metric is Contrast-to-Noise Ratio (CNR) which quantifies the lesion detectability against the background:

$$CNR = \frac{|\mu_L - \mu_B|}{\sigma_B}$$

where μ_L is the mean intensity of the lesion voxels, μ_B is the mean intensity of the background voxels and σ_B is the standard deviation of the intensity in the background. Higher CNR value indicates better lesion visibility from the background [16].

The second metric is the Contrast Recovery Coefficient (CRC), which measures the accuracy in recovering the true lesion contrast. CRC is defined as:

$$CRC = \frac{(\frac{\mu_{lesion}}{\mu_{background}} - 1)}{(\frac{a_{lesion}}{a_{background}} - 1)}$$

where μ_{lesion} is the mean intensity of the lesion voxels, $\mu_{background}$ is the mean intensity of the background voxels, and a_{lesion} and $a_{background}$ are the known activity concentrations of the phantom spheres, equal to 8 and 1, respectively. The CRC value ranges from 0 to 1, where 0 indicates no contrast, and 1 indicates perfect recovery [16].

The third metric used is the Metabolic PET Lesion Volume (MLV), which evaluates lesion size. It is calculated as the product of the number of voxels belonging to the lesion region of interest and the volume of a single voxel (8 mm³), providing a comparison with the theoretical lesion volume (524 mm³ for a 10 mm diameter sphere) [17].

RESULTS AND DISCUSSION

Simulations without lesions

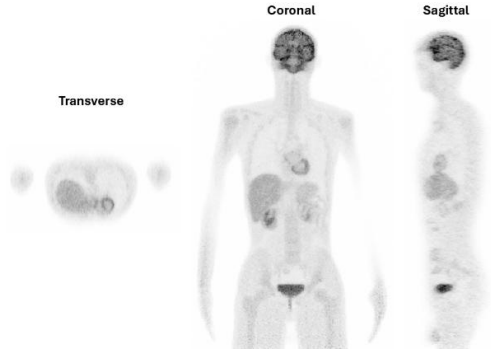

Full 60-s reconstruction without motion

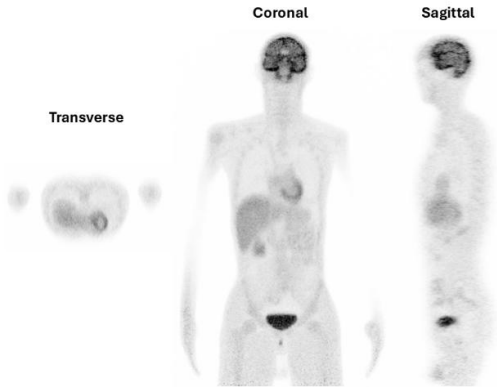

Full 60-s reconstruction with motion

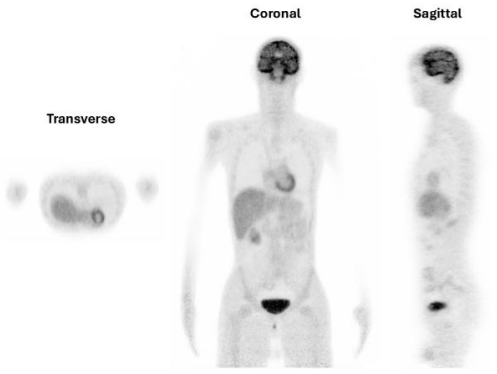

Short-time frame reconstruction after motion correction

Figure 3: Representation of motion correction effectiveness.

Cardiac and respiratory motion significantly compromised image quality, resulting in poor definition of anatomical structures and an excessively smoothed appearance of images. Therefore, motion correction is essential to correct these artifacts. As shown in Figure 3, applying motion correction improves image resolution and the definition of organ boundaries, although the result still does not fully match the ideal no-motion reconstruction.

One limitation is introduced by the averaging process used to combine short-time frames after motion correction. This step, necessary to obtain a single comparable image, reduces sharpness and introduces structured noise. Figure 4 illustrates this effect: compared to a full 60-s reconstruction, the averaged short-time frame image shows greater variations in intensities, demonstrating that this averaging process adds noise.

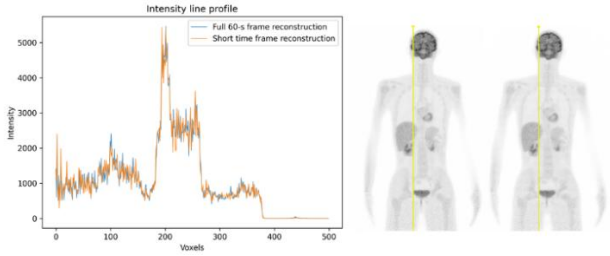

Figure 4: Line profile along the coronal plane of full 60-s reconstruction (middle) and short-time frame reconstruction (right) without motion artifacts.

The duration of frame length also affects the image quality. Shorter frames (e.g. 0.3125-s) allow a more effective motion correction with a better estimate of the motion. However, shorter stride results in noisier frames due to the reduced counts per frame, leading to less reliable motion estimation and degradation of image quality. This results in white bands artifacts as shown in Figure 5. Overall, the best reconstruction is the one with 0.9375-s frame reconstruction.

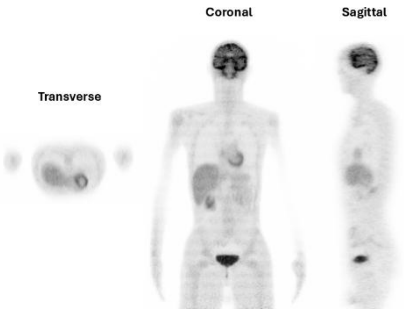

0.3125-s frame reconstruction

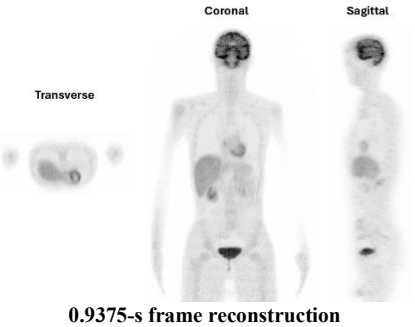

0.9375-s frame reconstruction

Figure 5: Impact of frame length.

Simulations with lesions

The motion correction pipeline was applied to three phantoms with different BMI values (low: 18.64, medium: 28.22, high: 37.96), each containing four spherical lesions (see Figure 6).

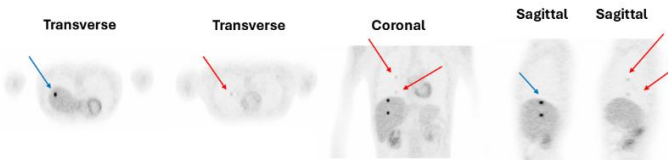

Figure 6: Location of lesions in the reference image.

Lesion segmentation was performed using a region growing algorithm, followed by calculation of three quantitative metrics: CNR, CRC, and lesion volume.

Cardiac and respiratory motion caused blurring and enlargement of the lesions compared to their known spherical shape. Lung lesions are more difficult to detect, mainly due to the overall lower background activity in the lungs compared to the liver, which reduces the absolute activity of the lesions and makes them less distinguishable. Motion correction leads to smaller, less blurred lesions, with more evident improvement in the liver than in the lungs. Among reconstruction methods, the overlapping reconstruction (frame length 0.9375 s with 0.3125 s stride) provides better lesion definition and detectability than a simple 0.9375-s frame reconstruction. The quality of PET images obtained after motion correction is improved after deblurring by applying Richardson Lucy Deconvolution. The different conditions are shown in Figure 7.

Figure 7: Impact of motion correction.

Examples of lesion segmentation masks are shown in Figure 8 and 9 for the lung and liver, respectively. Lesion masks follow the shape of lesions, indicating that the segmentation has occurred correctly. The lung lesion masks are larger than the actual inserted lesions and show little variation across different conditions. The lower lung lesion segmentation is unreliable since it incorporates part of the liver as part of the lesion due to the lung's lower background activity and increased noise, which hampers lesion discrimination. For this reason, the lower lung lesion was excluded from the analysis. As for liver lesion, the masks correctly identify the lesions, showing a reduced volume after motion correction.

To quantify the effect of motion correction, Figure 10 presents a comparison of CNR, CRC, and lesion volume before and after correction for each phantom. These results confirm that motion correction leads to improved image quality in all BMI scenarios. CNR increases in all conditions after motion correction, CRC slightly increases or remains the same, while volume decreases for low BMI phantom and increases for the other two phantoms.

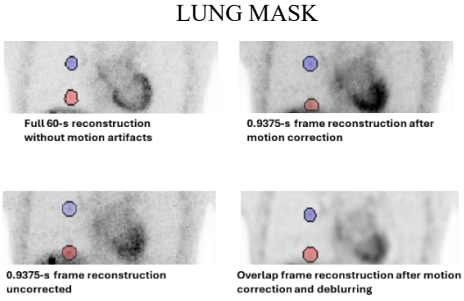

Figure 8: Example of lung lesion masks for low BMI phantom.

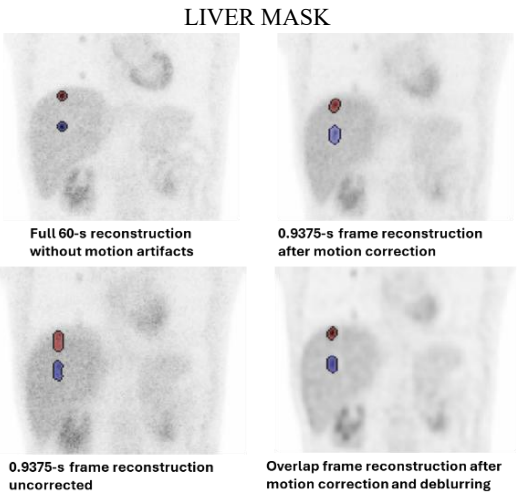

Figure 9: Examples of liver lesion masks for low BMI phantom.

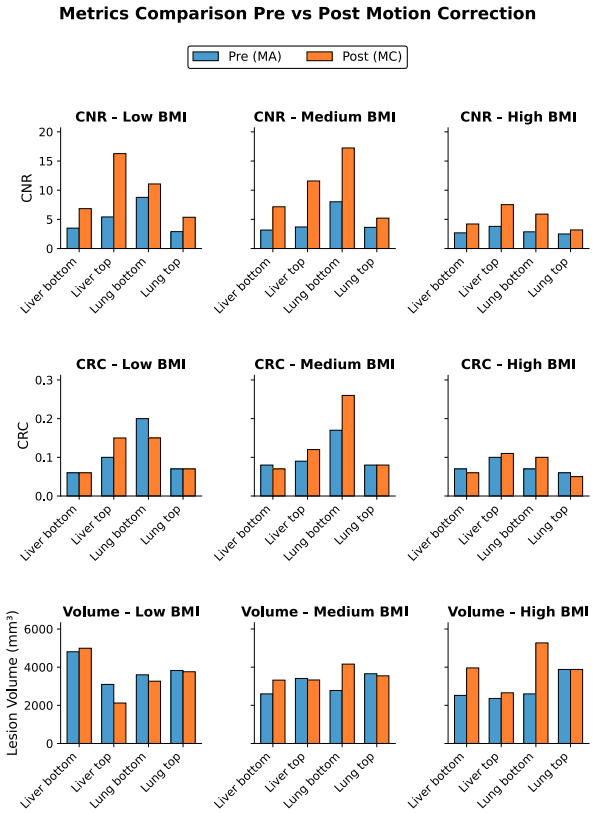

Figure 10: CNR, CRC and Volume Lesion before and after motion correction for the three phantoms.

Figures 11 and 12 compare the performance of the three BMI phantoms after motion correction. As expected, the low-BMI phantom shows the best lesion visibility, with significantly higher CRC and CNR values and lower lesion volume. Higher BMI phantoms exhibit more photon attenuation and noise, degrading lesion visibility. Although motion correction improves the lesion detectability, quantitative metrics show a limited gain compared to the low BMI phantom. CNR and CRC clearly decrease as BMI increases, suggesting that motion correction is less effective in recovering image quality in more attenuating conditions. Additionally, an increase in segmented lesion volume is observed in higher BMI cases. This is a rather counterintuitive trend, partly justified by the lower threshold used for segmentation, partly due to a lower photon counts. In particular, the most marked worsening is observed in the highest BMI phantom.

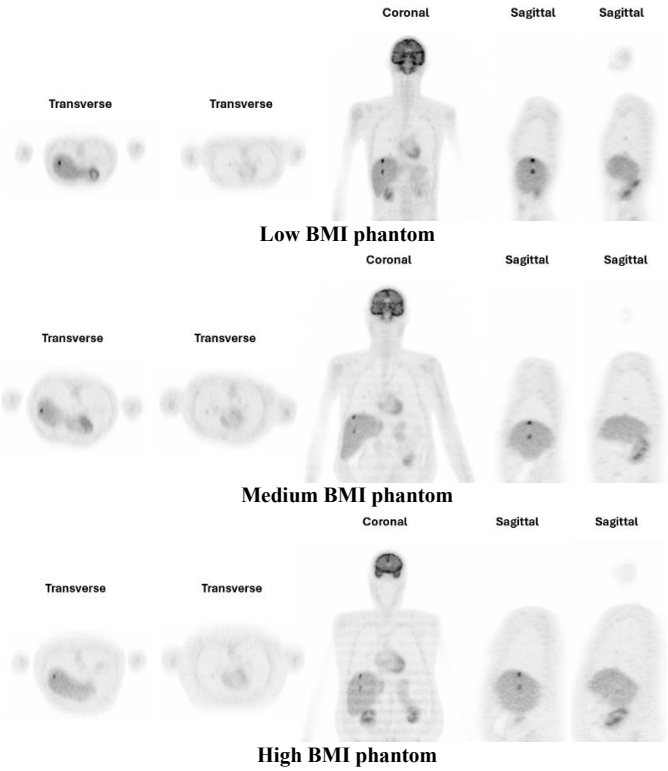

Figure 11: Impact of BMI in lesion detectability after motion correction.

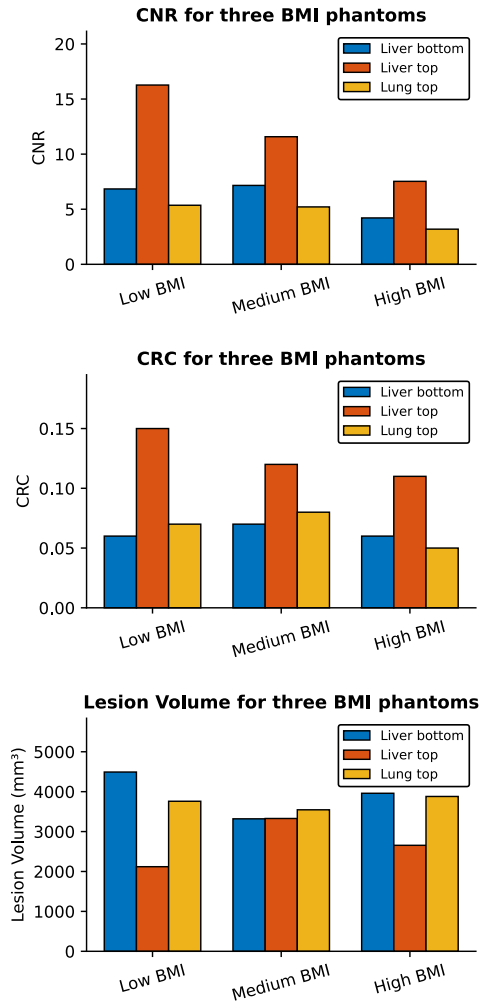

Figure 12: CNR, CRC and lesion volume for each phantom after motion correction.

CONCLUSIONS

This work aims to test a motion correction workflow for the Walk-Through PET (WT-PET), a novel dual flat-panel scanner developed by the MEDISIP Research Group at Ghent University.

The proposed method reconstructs short temporal frames and superimposes the frames with respect to the initial one (at time 0 s) to correct motion, then averages the corrected frames to produce a single image of the FDG tracer distribution. Various frame durations were tested: very short frames (0.3125 s) better follow respiratory and cardiac motion but suffer from noise and artifacts, while longer frames (0.9375 s) reduce noise but result in a reduced motion tracking accuracy. The optimal choice occurs with the overlapping reconstruction: each frame lasts 0.9375 s, with a step size of 0.3125 s between consecutive frames.

Simulations on three phantoms with different BMI demonstrate consistent improvement in image quality after motion correction, shown by increased CNR and CRC, and more accurate lesion volume estimation. However, as BMI increases, post-correction improvements are not as significant: CNR and CRC decrease with higher BMI, and lesion volume tends to be overestimated. This behavior is attributed to greater photon attenuation through human tissues and to a higher background noise.

This study represents an initial step toward motion compensation in WT-PET imaging and paves the way for future developments, both methodological and clinical.

REFERENCES

[1] F. Ul-Hassan and G. Cook, “Pet/ct in oncology,” Clinical Medicine, vol. 12, no. 4, pp. 368–72, Aug. 2012.

[2] M. M. Khalil et al., “Basic science of pet imaging,” Springer, Tech. Rep., 2017.

[3] S. R. Cherry, M. Dahlbom, S. R. Cherry, and M. Dahlbom, PET: physics, instrumentation, and scanners. Springer, 2006.

[4] T. LEWELLEN and J. KARP, “I. basic positron emission tomography principles.”

[5] A. Dimitrakopoulou-Strauss, L. Pan, and C. Sachpekidis, “Long axial field of view (lafov) pet-ct implementation in static and dynamic oncological studies,” European Journal of Nuclear Medicine and Molecular Imaging, vol. 50, no. 11, pp. 3354–3362, 2023.

[6] R. Aziz, J. Maebe, F. M. Muller, Y. D’Asseler, and S. Vandenberghe, “Quantitative analysis of patient motion in walk-through pet scanner and standard axial field of view pet scanner using infrared-based tracking,” EJNMMI physics, vol. 11, no. 1, p. 99, 2024.

[7] J. Wang, D. Bermudez, W. Chen, D. Durgavarjhula, C. Randell, M. Uyanik, and A. McMillan, “Motion-correction strategies for enhancing whole-body pet imaging,” Frontiers in Nuclear Medicine, vol. 4, p. 1257880, 2024.

[8] S. A. Nehmeh and Y. E. Erdi, “Respiratory motion in positron emission tomography/computed tomography: a review,” in Seminars in nuclear medicine, vol. 38, no. 3. Elsevier, 2008, pp. 167–176.

[9] J. M. Fitzpatrick, D. L. Hill, C. R. Maurer et al., “Image registration,” Handbook of medical imaging, vol. 2, pp. 447–513, 2000.

[10] J.-D. Tournier, R. Smith, D. Raffelt, R. Tabbara, T. Dhollander, M. Pietsch, D. Christiaens, B. Jeurissen, C.-H. Yeh, and A. Connelly, “Mrtrix3: A fast, flexible and open software framework for medical image processing and visualisation,” Neuroimage, vol. 202, p. 116137, 2019.

[11] B. B. Avants, N. Tustison, G. Song et al., “Advanced normalization tools (ants),” Insight j, vol. 2, no. 365, pp. 1–35, 2009.

[12] K. Assie, V. Breton, I. Buvat, C. Comtat, S. Jan, M. Krieguer, D. Lazaro, C. Morel, M. Rey, G. Santin et al., “Monte carlo simulation in pet and spect instrumentation using gate,” Nuclear Instruments and Methods in Physics Research Section A: Accelerators, Spectrometers, Detectors and Associated Equipment, vol. 527, no. 1-2, pp. 180–189, 2004.

[13] A. M. Loening and S. S. Gambhir, “Amide: a free software tool for multimodality medical image analysis,” Molecular imaging, vol. 2, no. 3, p. 15353500200303133, 2003.

[14] Bali and S. N. Singh, “A review on the strategies and techniques of image segmentation,” in 2015 Fifth international conference on advanced computing & communication technologies. IEEE, 2015, pp. 113–120
[15] S. Yuheng and Y. Hao, “Image segmentation algorithms overview,” arXiv preprint arXiv:1707.02051, 2017.
[16] S. K. Øen, L. B. Aasheim, L. Eikenes, and A. M. Karlberg, “Image quality and detectability in siemens biograph pet/mri and pet/ct systems—a phantom study,” EJNMMI physics, vol. 6, pp. 1–16, 2019.
[17] J. D. Schaefferkoetter, J. Yan, T. Sjöholm, D. W. Townsend, M. Conti, J. K. C. Tam, R. A. Soo, and I. Tham, “Quantitative accuracy and lesion detectability of low-dose 18f-fdg pet for lung cancer screening,” Journal of Nuclear Medicine, vol. 58, no. 3, pp. 399–405, 2017.

Table of Contents

Abstract **IV**

Extended Abstract **V**

List of Figures **XV**

List of Tables **XVII**

Acronyms **XIX**

1 Introduction **1**

2 Positron Emission Tomography **2**

2.1 Principles of PET Imaging 2

2.1.1 Radiotracers and Positron Emission 3

2.1.2 Detection and Coincidence Event 4

2.1.3 Image degrading effects 5

2.2 Image Reconstruction Techniques 8

2.2.1 Filtered BackProjection 8

2.2.2 Iterative Reconstruction Method 9

2.2.3 Correction for image degrading effects 11

2.3 Evolutions in PET 12

2.3.1 Short Axial Field of View PET 12

2.3.2 Long Axial Field of View PET 13

2.3.3 Total-Body PET 14

2.3.4 Walk-Through PET 14

2.3.4.1 Scanner Design and Detector Characteristics 15

2.3.4.2 Advantages and Challenges 16

3 Motion Artifacts in PET **18**

3.1 Sources of motion in PET 18

3.1.1 Voluntary Movement 18

3.1.2 Involuntary Movement 18

3.2 Motion Compensation Techniques 19

3.2.1 Hardware-Based Compensation 19

3.2.2 Data-driven Compensation 22

3.3 Image Registration and Motion Correction . . . 25
3.3.1 MRtrix3 for Motion Correction . . . 28
3.3.2 Advanced Normalization Tools for Motion Correction . . . 29

4 Methods 31
4.1 PET Data Simulation . . . 31
4.1.1 Simulation Methodology . . . 31
4.1.2 Data and Phantom Characteristics . . . 32
4.2 Image Reconstruction . . . 33
4.2.1 Formulation of the Reconstruction Model . . . 33
4.2.2 Implementation Framework . . . 34
4.3 Motion Correction . . . 35
4.4 Visualization on AMIDE . . . 35
4.5 Lesion Analysis . . . 36
4.5.1 Region Growing for Lesion Segmentation . . . 36
4.5.2 Detectability Metrics and Evaluation Criteria . . . 38

5 Results and Discussion 40
5.1 Demonstration of Motion Correction Effectiveness . . . 40
5.2 Simulation without lesions . . . 42
5.2.1 Impact of Motion Correction . . . 42
5.2.2 Impact of Summing Frames . . . 44
5.2.3 Impact of Frame Length . . . 45
5.3 Simulation with lesions . . . 47
5.3.1 Low BMI phantom . . . 47
5.3.1.1 Impact of Motion . . . 48
5.3.1.2 Impact of Motion Correction . . . 49
5.3.1.3 Impact of Frame Length . . . 50
5.3.1.4 Impact of Deblurring . . . 51
5.3.1.5 Lesion Analysis . . . 53
5.3.2 Medium BMI phantom . . . 61
5.3.2.1 Impact of Motion Correction . . . 61
5.3.2.2 Lesion Analysis . . . 62
5.3.3 High BMI phantom . . . 66
5.3.3.1 Impact of Motion Correction . . . 66
5.3.3.2 Lesion Analysis . . . 67
5.3.4 Cross-patient Summary and Effect of BMI . . . 70

6 Conclusions and Future Works 73
6.1 Summary of Findings . . . 73
6.2 Future Perspectives . . . 74
6.3 Societal Reflection . . . 74

A ANTs Registration Command and Parameters 76

B Threshold Values and Intensity Maxima Used for Lesion Segmentation **78**

B.1 Low BMI phantom 78

B.2 Medium BMI phantom 80

B.3 High BMI phantom 81

Bibliography **82**

List of Figures

2.1 Pet scan examples for different cancer types 2
2.2 Positron Emission and Annihilation Event 3
2.3 Time-of-Flight PET 5
2.4 Coincidences in PET 6
2.5 Iterative Reconstruction Process 9
2.6 SAFOV, LAFOV, and TB-PET 14
2.7 Panel dimensions of the Walk-Through PET scanner. 15
2.8 WT-PET Monolithic block 16
2.9 Model of the gap between detectors. 16

3.1 Effect of motion in activity concentration 19
3.2 PBG and ABG post-processing techniques 21
3.3 Types of motion compensation techniques 24

4.1 Model of the WT-PET scanner with detector gaps. 33

5.1 Motion Correction Effectiveness using MRtrix3 41
5.2 Application of the deformation fields to the activity maps 42
5.3 Motion Correction Effectiveness using ANTs 43
5.4 Impact of summing frames 44
5.5 Line profile along coronal plane 45
5.6 Imapct of frame length 46
5.7 Impact of median filtering 47
5.8 Impact of motion for low BMI phantom 49
5.9 Impact of motion correction for low BMI phantom 50
5.10 Impact of frame length for low BMI phantom 51
5.11 Impact of the number of iterations for deblurring 52
5.12 Impact of deblurring 53
5.13 Lung masks for low BMI phantom 56
5.14 Liver masks for low BMI phantom 57
5.15 Impact of motion correction for medium BMI phantom 62
5.16 Lung masks for medium BMI phantom 63
5.17 Liver masks for medium BMI phantom 64
5.18 Impact of motion correction for high BMI phantom 67
5.19 Lung masks for high BMI phantom 68

5.20 Liver masks for high BMI phantom 69
5.21 CNR, CRC, and Lesion Volume across different phantoms 72

List of Tables

2.1 Common used PET isotopes and their half-lives 4

4.1 Personal data and anthropometric parameters of the phantoms analyzed. 32

5.1 Mean, standard deviation (SD) and coefficient of variation (CV) of liver background ROIs — low BMI phantom 54
5.2 Mean, standard deviation (SD) and coefficient of variation (CV) of lung background ROIs — low BMI phantom 55
5.3 CNR – Liver and Lung Lesions for low BMI phantom 58
5.4 CRC – Liver and Lung Lesions for low BMI phantom 58
5.5 Volume (mm^3) – Liver and Lung Lesions for low BMI phantom . . . 59
5.6 Mean, standard deviation (SD) and coefficient of variation (CV) of liver background ROIs — medium BMI phantom 63
5.7 Mean, standard deviation (SD) and coefficient of variation (CV) of lung background ROIs — medium BMI phantom 63
5.8 CNR – Liver and Lung Lesions for medium BMI phantom 64
5.9 CRC – Liver and Lung Lesions for medium BMI phantom 64
5.10 Volume (mm^3) – Liver and Lung Lesions for medium BMI phantom 65
5.11 Mean, standard deviation (SD) and coefficient of variation (CV) of liver background ROIs — high BMI phantom 68
5.12 Mean, standard deviation (SD) and coefficient of variation (CV) of lung background ROIs — high BMI phantom 68
5.13 CNR – Liver and Lung Lesions for high BMI phantom 69
5.14 CRC – Liver and Lung Lesions for high BMI phantom 69
5.15 Volume (mm^3) – Liver and Lung Lesions for high BMI phantom . . 69

B.1 Threshold for Bottom Liver Lesion — low BMI phantom 78
B.2 Threshold for Top Liver Lesion — low BMI phantom 79
B.3 Maximum Value for Top Lung lesion — low BMI phantom 79
B.4 Maximum Value for Bottom Lung Lesion — low BMI phantom . . . 79
B.5 Threshold for Bottom Liver Lesion — medium BMI phantom 80
B.6 Threshold for Top Liver Lesion — medium BMI phantom 80
B.7 Maximum Value for Top Lung Lesion — medium BMI phantom . . 80
B.8 Maximum Value for Bottom Lung Lesion — medium BMI phantom 80
B.9 Threshold for Bottom Liver Lesion — high BMI phantom 81

B.10 Threshold for Top Liver Lesion — high BMI phantom 81
B.11 Maximum Value for Top Lung Lesion — high BMI phantom 81
B.12 Maximum Value for Bottom Lung Lesion — high BMI phantom . . 81

Acronyms

ABG	Amplitude-Based Gating.
AFOV	Axial Field-of-View.
AMIDE	Amide's a Medical Image Data Examiner.
ANTs	Advanced Normalization Tools.
BGO	Bismuth Germanate.
BMI	Body Mass Index.
CC	Cross Correlation.
CNR	Contrast-to-Noise Ratio.
COM	Center of Mass.
CRC	Contrast Recovery Coefficient.
CT	Computed Tomography.
CV	Coefficient of Variation.
DOI	Depth-of-Interaction.
FBP	Filtered BackProjection.
FDG	fluorodeoxyglucose.
FOV	Field-of-View.
FWHM	Full Width at Half Maximum.
GATE	GEANT4 Application for Tomographic Emission.
IMU	Inertial Measurement Unit.
ITK	Insight Toolkit.
LAFOV	Long Axial Field-of-View.
LOR	Line of Response.
LYSO	Lutetium–yttriumoxyorthosilicate.
MI	Mutual Information.
MLEM	Maximum Likelihood Expectation Maximization.

MRI	Magnetic Resonance Imaging.
MSD	Mean Squared Diffference.
MSQ	Mean Squares.
PBG	Phase-Based Gating.
PCA	Principal Compnent Analysis.
PET	Positron Emission Tomography.
PMT	Photomultipliers Tubes.
PSF	Point Spread Function.
RGSC	Respiratory Gating for Scanners.
ROI	Region of Interest.
RPM	Real-Time Position Management.
SAFOV	Short Axial Field-of-View.
SiPM	Silicon Photomultipliers.
SNR	Signal-to-Noise Ratio.
SPECT	Single Photon Emission Computed Tomography.
SRM	System reponse matrix.
SUV	Standardized Uptake Value.
SyN	Symmetric Normalization.
TB-PET	Total-Body PET.
TBR	Target Lesion-to-Background Ratio.
TOF	Time-of-Flight.
WT-PET	Walk-Through PET.
XCAT	Extended Cardiac-Torso.

Chapter 1

Introduction

Positron Emission Tomography (PET) is a medical imaging technique that allows the visualization of metabolic processes within the human body. PET plays a crucial role in medical diagnostics, particularly in oncology, where it is widely used to detect tumors, assess disease progression, and evaluate the effectiveness of radiotherapy treatments, especially in cancers such as breast and lung cancer. Other applications concern neurodegenerative disorders such as Alzheimer's disease and epilepsy [1].
PET is a sensitive technique that obtains three-dimensional images of a tracer distribution within the body [2]. Improvements such as the introduction of Time of Flight (TOF) information, which enhances spatial localization along the line of response, and the use of long Axial Field-of-View (LAFOV) systems, which enable the detection of a greater number of events, translate into better image quality and improved clinical applicability [3, 4]. A recent advancement is the development of a new flat-panel LAFOV scanner, the Walk-Through PET (WT-PET), which is the focus of this dissertation [5]. Despite its advancements, PET remains affected by several issues. An important challenge is chest motion caused by breathing and heartbeat, resulting in image artifacts [6]. The aim of this dissertation is to compensate for this motion by superimposing short reconstruction frames. Removing these artifacts would greatly improve image visualization and help with lesion detectability.

This dissertation is divided into five chapters. After this first introductory chapter, the second chapter describes the principles of PET imaging, focusing on image reconstruction methods. Two improvements in PET imaging are discussed: LAFOV PET scanners and the Walk-Through PET (WT-PET). The next chapter focuses on the motion artifacts in PET and methods to deal with them. The fourth chapter addresses the methodology to achieve the objectives of the thesis. The fifth chapter presents the results of the model evaluation, including a comparison between various image reconstructions, a quantitative analysis of detectability metrics and noise reduction by filtering. Finally, the dissertation concludes with a section summarizing the main findings, followed by a discussion of future research directions.

Chapter 2

Positron Emission Tomography

2.1 Principles of PET Imaging

Positron Emission Tomography (PET) is a widely used molecular diagnostic imaging procedure to acquire physiological information. Unlike purely anatomical imaging modalities, PET provides information about metabolism and function at the cellular and molecular level [1]. This is particularly relevant because many diseases cause alterations in biochemistry and physiology before anatomical changes become visible. PET can detect such functional abnormalities at an early stage, allowing for earlier diagnosis and more accurate treatment planning. In oncology, PET plays a central role in tumor detection, staging, therapy response assessment, and monitoring for recurrence. It also provides valuable diagnostic support in neurology and cardiology, becoming a routine diagnostic tool for several neurological disorders such as Alzheimer's disease and myocardial viability assessment. By offering high-sensitivity functional imaging, PET complements anatomical imaging techniques and contributes to more effective and personalized care [7]. An example is shown in Figure 2.1, where the different uptake of two radiotracers, ^{18} F-FDG and ^{68} Ga-FAPI, is evident in several tumors.

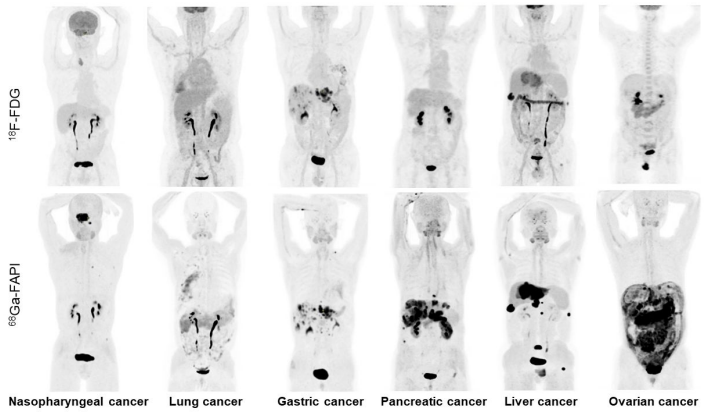

Figure 2.1: Examples of ^{18}F-FDG and ^{68}Ga-FAPI PET/CT for different cancer types [8].

2.1.1 Radiotracers and Positron Emission

PET imaging is used to study and visualize functional processes in the body through the use of a radiotracer. This is a biologically active molecule labeled with a positron-emitting radioisotope. Since it behaves chemically like a normal molecule, its distribution reflects physiological processes such as metabolism, allowing for the identification of functional abnormalities prior to the onset of anatomical alterations [9]. Therefore, PET imaging is based on the radioactive tracer principle. The injected radiopharmaceutical is labeled with a positron-emitting radionuclide. The nucleus of the isotope contains a surplus of positive charge, causing it to decay. During this process, a proton is converted into a neutron by emitting a positron, the positively charged antiparticle of the electron, and a neutrino, a chargeless and massless particle. This process is translated into the following formula:

$$p \rightarrow n + e^{+} + v \tag{2.1}$$

where p is a proton, n is a neutron, e^{+} is a positron, and v is a neutrino.
After decay, the positron interacts with a nearby electron in an annihilation event. The annihilation event transfers the energy mass of the positron to create two antiparallel photons of 511 keV energy each. The PET scanner is able to detect both photons within a short time frame of each other, forming a line of response (LOR) along which the annihilation event occurred. [1, 2, 10]. Figure 2.2 shows the process explained above: the emission of the positron from the radionuclide, its interaction with an electron, and the subsequent production of two gamma photons.

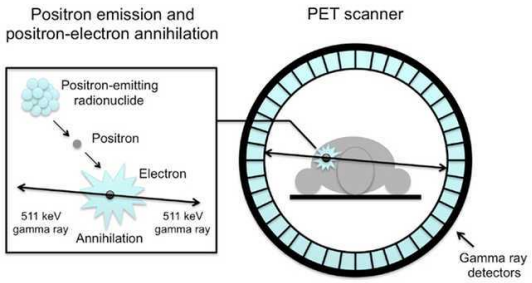

Figure 2.2: Positron Emission and Annihilation [11]

The most common PET radioisotopes are ^{15}O,^{13} N,^{11} C,^{18} F. Since they are found in biomolecules, their use as a labeled target does not interfere with the biological activity and metabolic processes. This ability differentiates PET from other techniques, which rely on the use of relatively large molecules that, when attached to the targeting species, may alter its bioactivity. [2, 10].

An important difference between all radioisotopes is their decay time. The half-life of a radionuclide $T_{1/2}$ is the time during which the amount of radioactivity decreases about 50% of its original value, depending on the isotope [12]. Since each radioisotope has a specific decay time and is produced in a cyclotron before being transported to the imaging site, it is crucial to select an isotope with a half-life appropriate enough to ensure that a sufficient level of radioactivity remains for clinical use at the time of

administration to the patient. Some of the most common radioisotopes are shown in Table 2.1.

Table 2.1: Half-life of isotopes commonly used in PET [13].

Isotope	**Half-Life (min)**
^{11}C	20.3
^{13}N	9.97
^{15}O	2.03
^{18}F	109.8
^{68}Ga	67.8
^{82}Rb	1.26

Among all these radioisotopes, ^{18}F-fluorodeoxyglucose, (^{18}F-FDG), is the most widely used tracer for evaluating disease, especially in oncology. It shows glucose metabolism, a process present in many organs that, in most cancers, has higher uptake due to the high expression and activity of glycolytic enzymes [1]. The half-life of ^{18}F-FDG, which is around 110 min, allows for the transport of the tracer to imaging centers that are distant from the cyclotron from which the radiotracer is produced [1]. In contrast, isotopes with shorter half-lives must be produced and administered to patients within a much narrower time window [2]. Once the radiotracer is administered and accumulates in the target tissue, the positron emission and subsequent annihilation generate gamma photons, which are then detected by the PET scanner.

2.1.2 Detection and Coincidence Event

The detectors are made of a scintillator crystal that absorbs high-energy gamma photons and produces an energy-proportional light signal. The optical light is converted into an electrical signal by Photomultiplier Tubes (PMT) or Silicon Photomultipliers (SiPM) which determine the energy, time and position of the incoming gamma ray. In a PET scanner, events are localized based on the principle of coincidence detection. A coincidence event occurs when both detectors detect a 511 keV photon at the same time. The detection is based on two assumptions:

- **Colinearity:** the path of the photons and the annihilation point are on the same LOR;
- **Simultaneity:** the photons arrive on the detectors around the same time.

As soon as the first photon arrives at the first detector, a coincidence window of a few nanoseconds is opened. During this window, an event occurs when another photon is detected. The events are stored in a listmode format, referring to the line of response that connects the coordinates of both detectors. By registering all the lines of response in a certain time, the PET image is formed through image reconstruction algorithms [10].

An important improvement to the detection of gamma photons is the introduction of time-of-flight (TOF) information. The time difference Δt between the interactions occurring in the two detectors is measured and related to the location of the annihilation Δx relative to the center of the line of response. The following equation describes the TOF principle, where c is the light speed:

$$\Delta x = \frac{\Delta t \cdot c}{2} \tag{2.2}$$

The current accuracy of timing resolution is around 200-600 ps. Although the TOF information is insufficient to exactly localize the annihilation point, it provides a position constraint that reduces the uncertainty along the line of response. This reduction in spatial uncertainty leads to an enhancement of the signal-to-noise ratio (SNR) in the final image reconstruction [10, 3]. Indeed, Figure 2.3 illustrates how TOF information increases the probability of identifying the annihilation site more precisely; without TOF, the event is equally probable along the entire line of response.

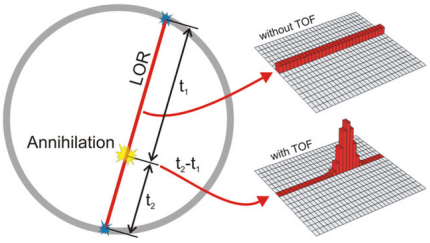

Figure 2.3: Time-of-Flight PET [3].

2.1.3 Image degrading effects

Despite the high sensitivity and spatial accuracy achieved through modern detection techniques such as TOF, the image quality of PET is compromised by some degradation effects. Some of them are corrected during image reconstruction, as explained in 2.2.3.

The first degrading effect is attenuation because 511 keV gamma photons must pass through the body before being detected. As described in [14], this process of interaction, which can be caused by absorption or scattering of photons, is described by an exponential equation:

$$I(x) = I_0 e^{-\mu x} \tag{2.3}$$

where I(0) is the flux of 511 keV photons incident on the medium, x is the thickness of the medium, I(x) is the flux of 511 keV photons passing through the medium without interaction, and μ is the linear attenuation coefficient, representing the probability of an interaction per unit distance. For 511 keV photons, the linear attenuation coefficient is given by two main components:

$$\mu \approx \mu_{\text{Compton}} + \mu_{\text{photoelectric}} \tag{2.4}$$

The first term accounts for Compton scattering, while the second corresponds to photoelectric absorption. In PET imaging, the interaction with body tissues accounts for the majority of signal attenuation, resulting in a reduced number of detected events and, consequently, a degraded signal. To compensate for this effect, attenuation correction techniques are applied during image reconstruction, often using anatomical data from Computed Tomography (CT) scans in PET/CT systems [14].

Another degrading effect of PET images is due to photon detection. Ideally, the PET system detects only true coincidences. These are the events in which the two gamma photons are produced by the same annihilation event and travel an undisturbed trajectory to the detectors. However, photons can undergo interactions before reaching the detectors, producing random and scattered coincidences (see Figure 2.4). Both reduce the image quality by introducing a background noise, reducing the SNR and the quantitative accuracy. Therefore, the aim is to increase the number of true coincidences while minimizing the others [14, 13].

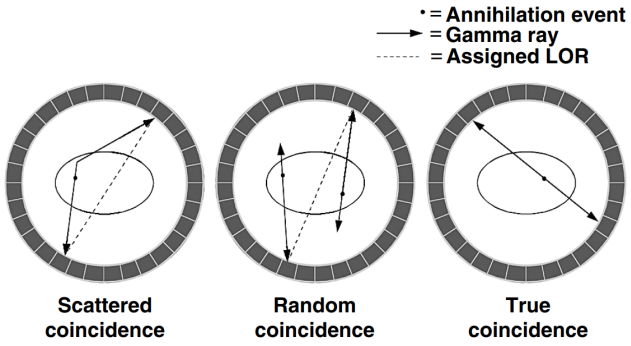

Figure 2.4: Coincidences in PET imaging: true, random and scattered [13].

Random coincidences occur when photons from two separate decay events are mistakenly identified as originating from the same one. Ideally, the two 511-keV photons produced during positron annihilation are emitted simultaneously and arrived at the detector at the same time. However, due to the finite temporal resolution of the system, a coincidence time window is defined: only the photons arriving within the window are considered to be part of the same annihilation event. It can occur that two uncorrelated photons are erroneously considered to be part of the same annihilation event. When such an event is recorded, the coincidence is called random or accidental. These types of events do not bring any spatial information to the image, resulting in a noisier image. It is possible to calculate how many random coincidences there are by knowing the counts per second for each detector, using the following equation:

$$N_R = 2\tau N_1 N_2 \tag{2.5}$$

where 2τ is the coincidence timing window, N_1 and N_2 are the individual detection rates of each detector. This formula clearly shows that the number of random events is directly proportional to the width of the timing window. Therefore, it is essential to

keep the window as narrow as possible, while still accounting for timing uncertainties in true events [14].
The second type of erroneous coincidences is scattered coincidence. As random coincidences, these also degrade the quality of PET images. These events originate from a real annihilation event, in which one or both photons have undergone a deviation of trajectory due to the Compton scatter interaction with the patient. As a result, the photons lose some of their energy, dropping below 511 keV. This change in trajectory causes the scattered photons to be mispositioned during image reconstruction, producing a low spatial frequency background that reduces image contrast. However, this energy loss can be exploited to reject many scattered coincidences by applying an energy window during data acquisition. The distribution of the tracer within the body and the size and space of the patient determine the presence of scattered coincidences [14].

Finally, the last degrading aspects of PET imaging concern those that limit spatial resolution, including the positron range, acolinearity, and the characteristics of the detectors. When a positron is emitted by a radionuclide, it has a certain kinetic energy and travels a certain distance through human tissue, losing energy before undergoing annihilation with an electron. Once the positron reaches thermal energies, it can interact with an electron in an annihilation event. The positron range is defined as the distance between the point of emission of the positron and the location where the annihilation occurs. Its value depends on the energy of the radionuclide [13].
The second aspect concerns acolinearity. PET imaging is based on the assumption that, after the annihilation, the two gamma photons are emitted in opposite directions 180° with zero angular momentum. However, due to a residual angular momentum of the positron, it is possible that the two gamma photons are no longer antiparallel. As a result, there is a slight angular deviation, approximately around 0.23°. While this value remains constant for all detector types, its impact on the system resolution increases with the diameter of the PET scanner, due to a greater mismatch between the assumed and actual annihilation positions [13].
The third and final aspect related to spatial resolution concerns the intrinsic resolution of the detectors. PET detectors are composed of small scintillator crystals, and it is generally assumed that the annihilation occurs at the center of the crystal. It may happen that this assumption does not correspond to the real position, resulting in a localization error which contributes to a reduced spatial resolution and a lower quality of the final image. Each detector is characterized by a Point Spread Function (PSF), which describes how a point-like source is spatially distributed in the detection process. For a single crystal, the PSF can be approximated by a step function of width equal to the size of the crystal. Since PET systems use pairs of detectors, the overall system PSF arises from the convolution of the two individual step-function PSFs, resulting in a triangular-shaped PSF, and its Full Width at Half Maximum (FWHM) corresponds to half the size of the crystal. Therefore, the use of smaller crystals al-

lows for better spatial resolution, improving the accuracy of image reconstruction [13].

All of these degrading effects have a direct impact on the quality of the reconstructed PET images. For this reason, appropriate image reconstruction techniques are required to reduce such artifacts and obtain an accurate representation of the radiotracer distribution.

2.2 Image Reconstruction Techniques

The aim of PET image reconstruction is to offer cross-sectional views of the radiotracer distribution within an object [15]. After the tracer injection and the annihilation between positrons and electrons, gamma photons are detected in pairs by detectors in the scanner ring. The output PET data consist of a series of points that represent the coincidence events that are singularly memorized as two point coordinates through which the line of response can be drawn. These LORs are acquired simultaneously from multiple angles using a ring of detectors surrounding the subject; through image reconstruction, it is possible to convert these LORs into a 3D image representing the distribution of the tracer within the body. Image reconstruction can be performed through two approaches. The first method is analytical reconstruction, which uses explicit mathematical formulas, originally developed in the context of CT to relate line integral measurements to the activity distribution in the object. The most common analytical approach is the Filtered BackProjection (FBP). The second approach is the iterative reconstruction method, which models the data acquisition process and, through subsequent iterations, compares the measured and estimated data until convergence is achieved. The most widely used is the Maximum Likelihood Expectation Maximization (MLEM) algorithm [14].
In the following sections, the two main reconstruction approaches will be discussed in more detail, starting with the analytical method.

2.2.1 Filtered BackProjection

FBP is the first approach to image reconstruction, widely used in CT for its simplicity and speed. This method reconstructs an image by back-projecting the source projections at different angles in order to obtain a good approximation of the initial object. During back-projection, all the activity is spread along the entire LOR. This leads to artifacts such as blurring. A ramp filter is commonly applied to eliminate this effect. The process is mathematically described by the inverse Radon transform:

$$f(x,y) = \int_0^{\pi} \left[\mathcal{F}^{-1}\left(|\omega| \cdot \mathcal{F}\{g(s,\theta)\}\right)\right]_{s=x\cos\theta+y\sin\theta} d\theta \tag{2.6}$$

In this equation, $g(s,\theta)$ is the projection over each angle θ, $\mathcal{F}$ is the Fourier transform of the projection multiplied by the ramp filter $|\omega|$, $\mathcal{F}^{-1}$ is the inverse Fourier transform to go back to the spatial domain. The final reconstructed image $f(x,y)$ represents the tracer distribution at each spatial position (x,y) [16].

Although FBP is computationally efficient, some approximations limit its use. First, it is based on the assumption that the source activity in the projections is equally distributed over the entire response line, decreasing the spatial resolution. Furthermore, FBP assumes that the starting projections are not noisy. Therefore, if the projections are noisy or if they do not cover all angles, the image quality is reduced by the presence of artifacts. As a result, iterative reconstruction methods have been increasingly adopted to overcome these limitations, allowing for a more accurate modeling of the physical processes involved in PET imaging and leading to improved image quality [16].

2.2.2 Iterative Reconstruction Method

Iterative reconstruction has become the standard method used in PET imaging. The fundamental concept of this method is summarized in Figure 2.5. The iterative process starts with an initial estimation of the tracer distribution, which is usually an image initialized to 1. This image is forward-projected to obtain the projection data of the radioactivity distribution of the initial guess. Forward projection, the inverse of backprojection, consists of summing up all the activities in pixels that are intersected by the line of response that corresponds to the measured sinogram element. Once the projected data is obtained, it is compared to the measured projection data. Based on this comparison, a correction factor is derived, which is backprojected into the image space. The initial estimate is then corrected with this factor according to a certain criterion. The whole process is repeated until the initial estimate closely resembles the true image. There are various types of iterative algorithms, each differing in some aspect of their formulation and implementation. One of the key components is the cost function, which gives a measure of the difference between the estimated and measured projection data. It is also the function maximized or minimized during reconstruction. The other important component is the criterion for updating the image at each iteration step [14, 16, 15].

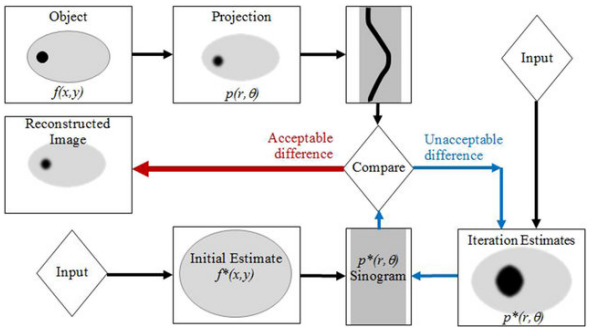

Figure 2.5: Scheme of the iterative reconstruction process [17].

The most frequently used iterative reconstruction algorithm method in PET imaging is the Maximum Likelihood Expecation Maximization (MLEM) algorithm. It is divided into two phases:

- **Expectation step (E)**: calculates the likelihood of a reconstructed image

based on the measured data;

- **Maximization step (M)**: updates the image estimate to maximize this likelihood.

Thus, the EM algorithm is an iterative algorithm that maximizes the likelihood under a Poisson data model. It implicitly treats the projection data as following a Poisson distribution, determined by the counting statistics in each projection bin, taking into account the statistical noise in the data.

The MLEM algorithm for PET can be written as:

$$f_j^{k+1} = \frac{f_j^k}{\sum_{i=1}^{m} h_{ij}} \sum_{i=1}^{m} \frac{p_i}{\sum_{l=1}^{n} h_{il} f_l^k} h_{ij} \tag{2.7}$$

This equation shows how the pixel intensity f_j at iteration $k+1$ is calculated based on the estimated image pixel intensity f_j at iteration k and the measured projection counts p_i. The algorithm can be seen as a set of successive projections and backprojections. The factor:

$$\frac{p_i}{\sum_{k=1}^{m} h_{ik} f_k^k} \tag{2.8}$$

is the ratio of the measured number of counts p_i to the current estimate of the mean number of counts in bin i; while the factor:

$$\sum_{i=1}^{n} \frac{p_i}{\sum_{k=1}^{m} h_{ik} f_k^k} h_{ij} \tag{2.9}$$

is the backprojection of the Equation 2.8 for pixel j into the image domain. It is then weighted by a sensitivity factor, which corresponds to $\sum_{i=1}^{m} h_{ij}$, altogether providing a correction term for the current image estimate. Finally, the current image estimate f_j^k is multiplied by the correction term, generating the new estimate f_j^{k+1} [14, 16, 15].

In summary, compared to analytical reconstruction, iterative reconstruction produces higher quality images. The main advantages are a better spatial resolution, a higher SNR, and a reduction in artifacts, resulting in sharper images with greater diagnostic value, especially in situations with high noise or missing data. One of the main drawbacks of iterative reconstruction is the high computational cost: it requires long processing times to obtain an image similar to the true object, especially when the images are 3D. However, given the current computational power of modern computers, iterative reconstruction algorithms have become more feasible for the routine clinical use. While FBP remains commonly used in CT, iterative reconstruction is the standard method in PET imaging [14, 16, 15]. Although modern reconstruction algorithms significantly improve image quality, PET images remain affected by several degrading factors, as explained in Subsection 2.1.3. Therefore, specific correction methods are applied to minimize these effects.

2.2.3 Correction for image degrading effects

Image degrading effects can be compensated by applying corrections to the data before analytical reconstruction or by integrating them in iterative reconstruction.

Due to the interaction between gamma photons and body tissues, photons may be attenuated. Different techniques are employed to compensate for this effect. First, attenuation correction factors were calculated using an external source. This approach required two scans: a blank scan in which the field-of-view (FOV) was empty and a transmission scan performed with the subject in the scanner. The correction factors were then computed as the ratio between the raw data and the transmission data. Since the transmission scan had a short acquisition time, the resulting SNR could be low, reducing the precision of the correction factors. Therefore, a new method was proposed, which involves calculating the attenuation correction factors based on the projection of a CT image that represents the attenuation coefficients in the body. In addition to providing a fast and low-noise alternative to traditional transmission scans, CT imaging is also often acquired to provide anatomical reference, which improves the localization and interpretation of functional PET data [10].

In addition to attenuation, another major image degrading effect is the presence of scattering. Scattered events in the 3D PET images also account for 30%-50% of all events found, a very high percentage that contributes to a smooth background in the reconstructed image. Since scattered photons tend to have an energy lower than 511 keV as explained in Subsection 2.1.3, these events can be reduced by imposing a threshold on the energy value of the photons. However, even with the energy window applied, some scattered coincidences remain within the accepted energy range and must be corrected during image reconstruction. Recent studies estimate the scatter distribution using Single Scatter Simulation.
Besides scatter, random coincidences also reduce image quality, although their correction is generally easier than dealing with scatter coincidences. Random coincidences depend on the amount of activity in the body and can be significant for studies using large amounts of radioactivity. The most common method involves using a "delayed window", which estimates the number of random events that fall into it. Since this window does not record true coincidences, it allows for an estimation of the random event contribution, which can then be subtracted from the acquired data [10].

Finally, the last correction concerns the non-uniform response of the PET detectors. It depends on the intrinsic properties of the detector itself as sensitivity and geometry. Normalization is employed to compensate for these variations. In modern PET scanners, component-based approaches are mostly used to minimize these artifacts. For example, they rely on the efficiency of the detectors, the geometry, and the arrangement of the detectors. These measurements are performed using a known source and the number of ideal coincidences is compared with the number of

actually measured coincidences. Normalization factors can be estimated sequentially or simultaneously. In the first case, the detector efficiency is estimated first, then the data is corrected and the other corrections are estimated on the corrected data. In the second case, all factors are estimated together using a statistical estimate. This second method significantly reduces the number of events needed for normalization scans [10].

All these corrections remove artifacts and improve image quality, obtaining a better SNR [10].

2.3 Evolutions in PET

PET is the most widely used imaging system for tumor detection due to its high sensitivity and non-invasiveness. Initially, the scanner was an axial ring with a limited number of detectors covering a single horizontal section, requiring rotation around the patient to obtain a 3D image. Later, the number of detectors increased to form a full ring, eliminating the need for rotation, although patient movement along the scanner was still necessary to cover a larger volume. The next step was to design a scanner that took multiple slices at the same time, increasing sensitivity and being able to investigate a larger part of the body. The field of view has increased from Short Axial Field of View (SAFOV) to Long Axial Field of View (LAFOV). New advancements are currently under development, such as the Walk-Through PET (WT-PET), a LAFOV scanner that relies on vertical panels [18].

2.3.1 Short Axial Field of View PET

The first PET scanners had a limited axial field of view (AFOV), of about 3 cm, allowing investigation exclusively of small animals. For clinical use, PET scanners featured an AFOV of about 15 cm, restricting the investigation to a part of the human body, focusing on a single organ. However, scanning more parts of the body was still feasible by translating the bed during the acquisition process, allowing an examination of lesions and tumors throughout the body. In fact, the most common case for PET/CT is oncological imaging, which typically covers the area from the base of the skull to the mid thighs to capture potential disease sites [18].
Since then, with the advent of new technologies, many developments have taken place. First of all, there has been a significant increase in FOV. From the first scanners with a few centimeters AFOV, the technological advancement has extended it to 25 cm, allowing the acquisition of images covering a larger portion of the body. These conventional PET scanners are also called SAFOV, featuring an AFOV in the range of 15-25 cm. However, to obtain a full-body image, it is necessary to use techniques such as step-and-shoot, in which the bed is moved between acquisitions, or continuous bed motion, in which the bed moves without interruptions. SAFOV scanners are characterized by low efficiency since most of the body (80%-90%) is outside the standard-axial FOV. This means that they can collect only 3%-5% of the

total signal emitted by the patient, thus limiting the sensitivity of the acquisition [19, 20].

2.3.2 Long Axial Field of View PET

To overcome the limitations of SAFOV systems, the FOV has been further increased, reaching values between 1 and 2 meters. This system is called LAFOV. The most widely used commercial LAFOV device at present is the Biograph Vision Quadra (Siemens Healthineers), featuring a 106 cm AFOV. LAFOV scanners are devices with an AFOV greater than 100 cm, which is sufficient to complete most of the oncologic and non-oncologic studies [19, 20].
Whereas SAFOV PET typically require multiple bed positions to image the region from vertex to thighs in most subjects, LAFOV PET allows coverage of the same anatomical range in a single-bed position for the majority of the population.
LAFOV PET scanners present several advantages. They lead to a substantial improvement in sensitivity, image quality, and lesion quantification, allowing a significant reduction in acquisition time and low-dose examination protocols. As a consequence of the extended field of view, it is possible to simultaneously observe how the radiopharmaceutical is distributed and metabolized in the various organs and tumor lesions. This is essential since it allows to see in real time how the tracer moves in the body, without interruptions caused by the bed's movement [21].
The improved image quality is attributed to the high sensitivity of the new system, which allows for a higher SNR. This is also reflected in a better detectability of lesions compared to the background and a better lesion quantification. In this regard, the study conducted by Alberts et al. compare the performance of the LAFOV Biograph Vision Quadra PET/CT system with the SAFOV Biograph Vision 600 PET/CT, both designed by Siemens Healthineers [22]. The results showed that the LAFOV system has better image quality than the SAFOV system, regardless of the acquisition times. The main advantage of LAFOV is that it is possible to obtain acceptable quality and identification of all lesions even with short scanning times. This is confirmed by the SNR values, which, in the case of 10-minute LAFOV acquisitions, produce the highest values. Regarding lesion detectability, all lesions are detectable with the LAFOV system, while the Target Lesion-to-Background Ratio (TBR) does not appear to be particularly different between LAFOV and SAFOV, not even with very short LAFOV acquisitions (0.5 min) [22].
An additional advantage of the LAFOV system is the possibility of performing scans while significantly reducing the dose of radiopharmaceutical while maintaining the same image quality. The study shows that this can be reduced even 6 times compared to the SAFOV system while maintaining the same visual quality [22].
The results highlight how the introduction of the LAFOV system not only improves image quality and detectability of lesions, but also reduces the dose of radiopharmaceutical, which is particularly important for the health of the patient. In fact, low dose reduces the risks related to tracer radioactivity and shortens the time for which

the patient is radioactive [22].
Finally, reducing the scan time due to increased sensitivity results in faster acquisitions, enabling the scanning of a greater number of patients within the same period, up to 6-8 patients per hour [4].

2.3.3 Total-Body PET

A further step from LAFOV PET is the Total-Body (TB) PET scanner. This is still a LAFOV scanner allowing whole-body imaging in a single bed position, featuring an AFOV greater than 188 cm. An example of TB-PET is the uEXPLORER (United Imaging) [23], currently the largest commercially available PET scanner, with an AFOV of 194 cm [19, 20].

A graphical representation of the three PET systems are shown in Figure 2.6.

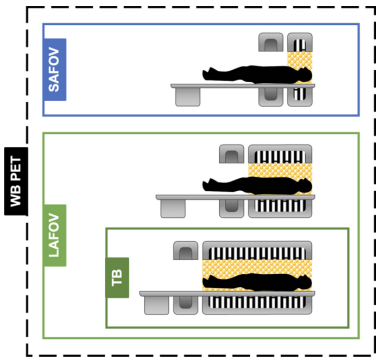

Figure 2.6: Graphical representation of different PET scanners based on axial field-of-view: SAFOV, LAFOV and TB-PET [19].

In conclusion, the LAFOV system offers superior performance compared to the SAFOV, with shorter scan times (under 2 min) and reduced radiopharmaceutical dose, while maintaining excellent image quality and adequate contrast between lesion and background. These advantages make it particularly suitable for clinical settings where rapid or low-dose protocols are required.

2.3.4 Walk-Through PET

Although LAFOV PET systems have shown numerous advantages in terms of fast acquisitions and lower dose while maintaining high sensitivity, they are rarely used in routine controls in nuclear medicine departments due to the high cost. The latter is due to the number of detectors used, 4–8 times greater than the standard PET-CT. Furthermore, although patient acquisition time can be done in 30 s to 2 minutes, the time to position the patient on/off the bed is longer.

To overcome these challenges, the MEDISIP research group at Ghent University is currently developing a new LAFOV PET device: the Walk-Through PET (WT-PET). This is a novel and cost-effective system, consisting of dual flat panel, specifically designed to perform PET imaging on patients in upright standing position.

2.3.4.1 Scanner Design and Detector Characteristics

The design of the WT-PET requires the patient to be scanned while standing for 30 to 60 seconds. The positioning of the patient is less complicated than the positioning on the PET/CT table, as the patient enters and stands in the designated area for scanning.
The WT-PET is composed of two vertical flat panels, each with dimensions of 70 cm wide and 106 cm high, with a gap of 50 cm between the two panels as represented by Figure 2.7. Since it is a vertical design, the dependence on the height of the patient must be compensated. To overcome this problem, a panel that can be moved up and down is used. This also allows to scan the legs and feet in a different position [5]. The panel dimensions come from a study conducted on 40 randomly selected patients from the University Hospital (CHU) of Liège (Belgium) and from the study conducted by Pheasant et al. on body space, ergonomics and Anthropometry [24].

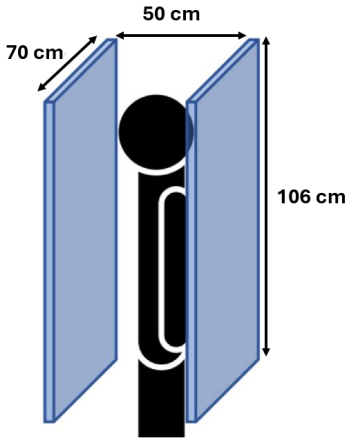

Figure 2.7: Panel dimensions of the Walk-Through PET scanner.

Each panel is composed of 12 × 14 array of monolithic Lutetium–yttrium oxyorthosilicate (LYSO) detector blocks that are 50 × 50 × 16 mm^3 in size and are coupled to an 8 × 8 array of 6 × 6 mm^2 SiPMs, as shown in Figure 2.8. Monolithic detectors offer better spatial resolution than pixelated detectors due to their inherent technology, which provides improved two-dimensional resolution along with depth-of-interaction (DOI) information. DOI capabilities allows the detectors to be positioned closer to the patient, which in turn improves system sensitivity by reducing the probability that emitted gamma photons miss the scanner.

The cost of a PET/CT device depends mainly on the scintillators, the photosensors (Silicon Photomultipliers), and the readout electronics. The first idea of the WT-PET system used monolithic BGO (Bismuth Germanate) detectors, arranged in a flat panel. This configuration allowed the detectors to be placed closer to the patient, resulting in fewer detectors needed for the same sensitivity. As a result, the area of the detector surface has been decreased by a factor of 1.9, which in turn reduced the component costs by 3.3 times compared to the LAFOV system. However, the cost

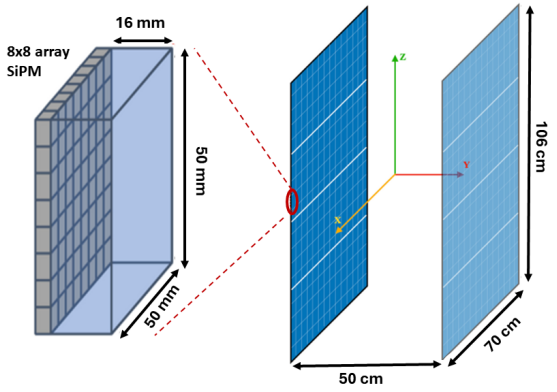

Figure 2.8: The monolithic block on the left and its integration in the flat panels on the right [25].

of the WT-PET system remained approximately 1.2 times higher than the SAFOV system. BGO is a less expensive material than LYSO for the same volume and offers higher stopping power but does not generally support TOF. With the use of LYSO detectors, the panel spacing remained the same as in BGO configuration, but the detector design was changed to further reduce costs: gaps were introduced between detector rows to reduce the number of detectors per row, resulting in a 12 x 14 LYSO system instead of 14 x 20 BGO configuration (see Figure 2.9). Although the sensitivity of LYSO detector is lower than BGO, the TOF capability of LYSO compensates for this loss. In the end, the overall cost of the 12 x 14 LYSO system is similar to that of the 14 x 20 BGO system, due to the lower cost of BGO [26, 5].

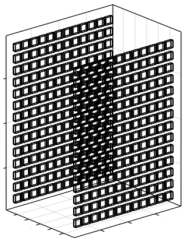

Figure 2.9: Model of the gap between detectors.

2.3.4.2 Advantages and Challenges

Among many advantages of this new design, the first is the improvement in workflow efficiency. The patient positioning time in WT-PET is shorter than traditional systems like SAFOV or LAFOV. The total acquisition time for the WT-PET is about 5 minutes per patient, compared to 17 minutes for the SAFOV and 8 minutes for the LAFOV [5, 26]. This translates into a higher patient throughput: approximately 87 patients are scanned in an 8-hour workday, compared to 28 patients for the SAFOV and 53-60 patients for the LAFOV [5]. This is an important advantage for the entire nuclear medicine department, as it allows the patient to perform more tasks independently, which in turn reduces some of the workload for the personnel. A second advantage is the reduction of the injected dose required per patient. Thanks to

the high sensitivity and scanning speed, the required radiotracer activity per patient can be drastically reduced by up to 66% with WT-TB-PET compared to a SAFOV system, and by 45% with LAFOV. In addition, a small footprint is required to install the PET system. In contrast to traditional LAFOV system, which requires an area of 35-40 m^2, the WT-PET setup needs only 2-6 m^2. This leads to the possibility of reorganizing the PET room space in which the part dedicated to the old scanner becomes the waiting room for the new design [5].

Despite the clear advantages such as (i) lower radiation dose, (ii) faster, and (iii) low cost imaging, (iv) less personnel involvement, some aspects remain challenging such as its non-applicability to patients with mobility or walking impairments. Not all patients (estimated at $< 10\%$-20%) can stand to perform the scan, leading to the use of other alternatives. Although the design aims to perform fast imaging of 30 seconds or at most 1 minute, motion artifacts are present. These are more pronounced than in a lying position as the patient is less stable. Motion correction techniques can be used to minimize this problem [5].

Chapter 3

Motion Artifacts in PET

3.1 Sources of motion in PET

Patient movement is one of the major sources of artifacts in PET images, reducing image quality and diagnostic accuracy. During PET acquisitions lasting several minutes—particularly with high-resolution PET systems—even minimal patient movement can cause blurring and distortions in the final image, compromising the visualization of lesions or body structures. Patient movements are divided into voluntary and involuntary types, primarily including respiration and cardiac motion [6].

3.1.1 Voluntary Movement

Voluntary movements are defined as intentional actions governed by the motor cortex. They mostly involve movements of the upper/lower limbs and the head, often caused by the discomfort during scanning and its excessive duration. Since they are under voluntary control, these movements are inherently unpredictable and challenging to correct. These movements can lead to misalignment between PET and CT scans (in hybrid PET/CT systems), introducing significant attenuation correction errors. Moreover, the distribution of the tracer, which changes over time, could be compromised, resulting in an increased or decreased apparent concentration. This can impact the precise measurement of lesions and potentially result in incorrect diagnoses, either missing true abnormalities or indicating false ones.
Although such movements can be prevented to some extent by asking the patient to remain still, their unpredictable nature always remains a persistent challenge [6, 27]. Specific strategies and technologies aimed at compensating for such voluntary movements are discussed in detail in Section 3.2.

3.1.2 Involuntary Movement

Involuntary movements significantly degrade the quality of PET images. They are not controlled by the patient's will, including breathing and heartbeat. They involve the lungs, chest, and abdomen, which are generally regarded as having the greatest

need for motion correction. In fact, they are the parts of the human body that are most often scanned to investigate lesions.
Cardiac and respiratory motions may lead to organ distortions, posing a significant challenge in medical diagnostics. Breathing causes the appearance of blurred lesions, leading to the interpretation of a larger volume as a lesion than it actually is, and to a reduced contrast between diseased and healthy tissue. By overestimating the lesion volume, therapy may involve the irradiation of healthy tissue, which is not the intended goal of the treatment.
Figure 3.1 shows the concentration distribution between a stationary point and a point affected by motion. In the latter case, all the activity is spread across the entire range of motion, resulting in an underestimation of both the activity concentration and the Standardized Uptake Value (SUV), a semi-quantitative measure used in PET scans to assess tracer uptake in tissues. [6, 28]

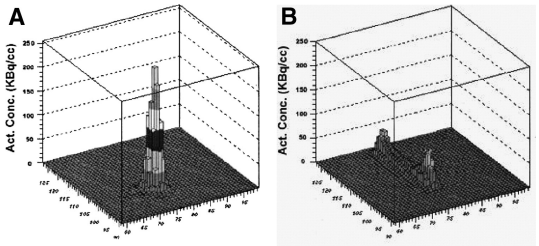

Figure 3.1: (A) Apparent activity concentration for a stationary point source. (B) Apparent activity concentration for oscillating point source caused by motion [28].

To overcome these problems, several correction strategies have been developed, allowing for better visualization of the lesions and better image quality.

3.2 Motion Compensation Techniques

Motion artifacts can significantly compromise PET image quality by introducing blurring, reduced contrast, and errors in lesion localization and quantification. As a result, tracer uptake may be underestimated, misinterpreting the pathology. Several motion compensation techniques have been developed to address these problems, broadly classified into hardware-based and data-driven approaches.

3.2.1 Hardware-Based Compensation

Hardware-based methods use external devices to track the patient's motion during PET data acquisition. In recent years, various solutions have been proposed depending on the motion artifact to be addressed [6]. These devices operate mainly in two ways:

- Generating a signal used to synchronize data acquisition (also called gating)
- Guiding retrospective correction

Regarding head motion, most systems rely on an optical mechanism: cameras record the motion of specific points marked by markers fixed on the subject's face. Some-

times, facial features may serve as indicators for motion tracking [29]. This approach offers simplicity and immediacy; however, it often requires longer scan time and may introduce errors stemming from camera acquisition. Another device to measure real-time triaxial acceleration and velocity is the inertial measurement unit (IMU), built upon an accelerometer and a gyroscope [30]. The IMU is attached to the subject and operates similarly to the optical tracking camera [6].

For cardiac motion correction, the most widely adopted method is the electrocardiogram (ECG), which enables gating based on this physiological signal [31]. Nonradiopaque electrodes are used throughout the scan to avoid interference with the CT component in the hybrid PET/CT system [6].

Respiratory motion introduces a greater number of artifacts in PET images, making it one of the most significant challenges. For this reason, several methods have been developed to address this motion source. The more straightforward technique is marker tracking, which consists, as in the case of head motion, of a camera capturing the movements of the tracker positioned on the patient's chest. To obtain a depth profile, multiple cameras can be used in order to integrate distinct profiles and reconstruct the 3D image. Other types of cameras are thermal or infrared. These devices are easy to implement, but require more time to process the data, making it less practical [6].
Another optical tracking system is the Real-Time Position Management (RPM) system commercialized by Varian Medical Systems (Palo Alto, CA). It includes a video camera that tracks the vertical displacement of two infrared reflective markers positioned on a plastic block placed on the patient's thorax. This system has demonstrated high reproducibility and precision in generating the respiratory signal [28]. The next generation version of RPM is the Respiratory Gating for Scanners (RGSC) system as described in [32], which obtains the 3D positions of the markers, unlike the 2D information of RPM. Moreover, RGSC employs a shielded camera that minimizes background noise and stabilizes the camera. For healthy patients, both methods have demonstrated the same effectiveness, while, for patients with irregular breathing patterns, there are doubts about their actual validity [6].
One well-known technique to track respiratory motion is to use a respiratory belt that patients wear around their chest or abdomen. This non-invasive instrument detects variations of thoracic or abdominal circumference with the respiratory cycle. It consists of a strain gauge that measures the volume-change signal in real-time and transmits it to the PET scanner for respiratory-triggered gating. Correct positioning of the device is essential to obtain a valid correction. An example of this device is the AZ-733V system (Anzai Medical) [28], capable of detecting pressure changes during breathing. This signal, digitized by an analog-to-digital converter (ADC), is used for synchronization with PET or CT data.
In addition to optical methods, temperature sensors such as the BioVET CT1 system produced by Spin Systems or spirometers such as the PMM spirometer from Siemens

have also been investigated [28]. While the former measures the difference between room and air temperature during inspiration and expiration, the latter measures the airflow entering and exiting the lungs. Both have an air tube in the patient's nose or mouth and the acquired data are transmitted to a computer for post-processing. The presence of this tube may render these systems invasive or uncomfortable for patients, particularly during prolonged acquisitions [28].
Finally, IMUs based on microelectromechanical systems (MEMS) ([33]) and continuous-wave radar systems ([34]) have emerged as promising technologies for motion tracking. The advantages are low cost and non-invasiveness; however, their main limitations involve error accumulation and signal processing [6].

All of the hardware-based devices mentioned above require post-processing techniques to effectively remove motion artifacts. There are two possible methods: phase-based gating (PBG) and amplitude-based motion gating (ABG), both shown in Figure 3.2. PBG involves the definition of a periodic motion cycle, whether cardiac or respiratory. This motion cycle is the physiological signal corresponding to the motion and it is recorded and synchronized with imaging data. After synchronization, it is divided into multiple phases, each representing a unique gate. Only selected phases, typically the most stable ones at the end of exhalation, are retained for image reconstruction. In contrast, ABG considers the amplitude of the physiological signal. Looking at the amplitude, only a part of the motion cycle is selected, all the rest is discarded. The choice of the amplitude band is made considering the most relevant and stable part of the respiratory or cardiac cycle. This method greatly reduces artifacts, enhancing image clarity and accuracy.

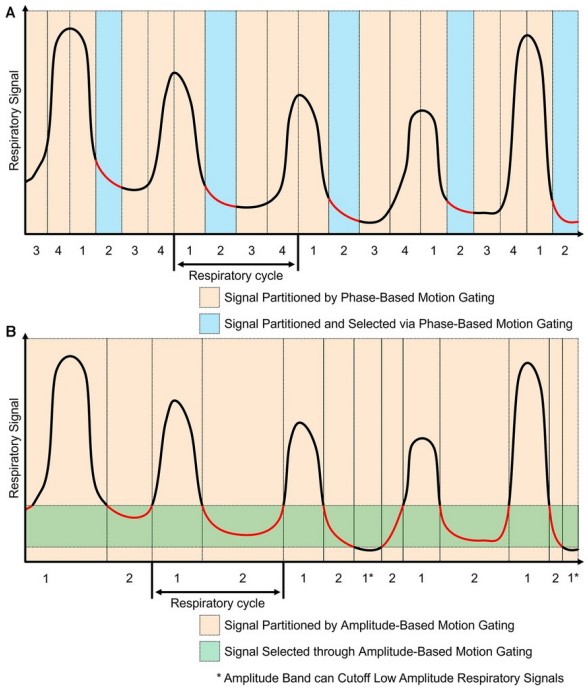

Figure 3.2: The motion signal is separated in different patterns: (A) Phase-based gating; (B) Amplitude-based gating [6].

In conclusion, phase-based motion gating is the most appropriate choice for cardiac and respiratory motion since both have a cyclic pattern, which is easy to analyze by dividing it into phases. Amplitude-based motion gating is preferable when the motion is more unpredictable, either in situations where the amplitude varies greatly or when there are multiple sources of motion [6].

3.2.2 Data-driven Compensation

A non-invasive alternative to hardware-based systems is data-driven gating methods. These methods retrospectively analyze PET data to identify and correct physiological motion in patients, without the use of external devices. The analysis can be done in a variety of ways including motion estimation, image registration, or machine learning, improving the quality and accuracy of the acquired images.

Regarding head motion, one of the main methods to address it is the 3D Center of Mass (COM), which calculates the center of distribution of the tracer along all three dimensions for each reconstruction frame, allowing the estimation of the direction of motion [35]. Results have shown that this method is comparable in effectiveness to the breathing belt system. The COM solution performs best with slow and gradual movements, such as those of the head.
Another type of solution is based on image registration, a simple approach that is very often used to estimate motion. First, the images are reconstructed in very short frames (about 1 second), then they are aligned to a reference frame. This is done for the entire scan duration. By modifying the frame reconstruction duration, it is possible to obtain a higher or lower SNR: to have better SNR, the temporal resolution must be lower. This is also an advantage of motion estimation, which is improved by frame durations shorter than 1 second [6, 28].
The third option is dimensionality reduction, and more precisely, Principal Component Analysis (PCA) [36]. PCA decomposes PET data into principal components, isolating the components that best identify head motion. This method has proven effective in identifying motion and producing motion-free images, achieving up to 97% in image sharpness compared to uncorrected images (79%-82%) and reducing the number of reconstructions required by approximately 3.4 times. The suggested approach improves the precision of PET scans for neurological disorders.
Direct motion modeling is another strategy to characterize motion, being directly integrated into the image reconstruction process [6].
Finally, deep learning models such as DL-HMC (Deep Learning for Head Motion Correction) have been developed [37]. This method accepts as input 3D representations of the tracer reconstructed in 1-s windows and returns the six rigid transformation parameters that characterize the motion. The model is trained in a supervised manner using optical tracking data as a reference, optimizing the mean square error between the estimate and the actual measurement. Another approach employs a conditional generative adversarial network (cGAN), trained on Magnetic Resonance Imaging

(MRI)-corrected PET data as described in [38]. The model generates low-noise images from high-noise initial frames, which are subsequently registered to the reference frame to estimate 3D motion vectors. This strategy has demonstrated improvements in image quality and quantification of brain metabolism [6].

For cardiac and respiratory movements, the compensation is more challenging. These motions involve the thorax simultaneously, rendering it complex to analyze the two movements independently. Consequently, in most cases, only respiratory compensation is implemented. Various approaches have been proposed.
PeTrack (Positron Emission Tracking) is very similar to a hardware-based gating method, described in [39]. It utilizes the trajectory of an internal emission source as a marker to estimate movement. It has been shown to be effective under irregular respiration patterns, though it potentially introduces an additional dose of radiopharmaceuticals.
Dimensionality reduction is done with two subcategories: PCA as applied to the head and Laplacian eigenmaps. Both are based on the decomposition of PET data and the subsequent classification into multiple bins from which the images are then reconstructed, but, while PCA works with linear equations, Laplacian works in a non-linear way. The COM method is similarly applied to respiratory motion. By monitoring the movement of the COM, it is possible to estimate respiratory motion, which can then be applied to adjust the PET data in the process of image reconstruction. The results show an improvement in lesion contrast compared to uncorrected images [6].
A different method in data-driven gating involves assessing the counts obtained from the unprocessed PET data. Motion artifacts would indeed create variations in PET data: there is a correlation between the movement of the motion sources and the fluctuations of the counts. There are two options: frequency-based or adaptive binning. Frequency-based techniques analyze the periodicity of the PET signal to identify the respiratory component, while adaptive binning selects only stable frames based on the amplitude of the breath [6].
As an alternative to multi-bin gating, the Deep-Inspiration Breath Hold (DIBH) method has been proposed in [40], whereby patients hold their breath during deep inspiration during the simultaneous acquisition of PET and CT images. This method facilitates perfect anatomical-functional correspondence and precise attenuation correction [28].
One of the most commonly used techniques is image registration. It is based on the alignment of each frame of the reconstruction to the first or reference frame. Registration may be rigid or non-rigid. Rigid registration consists of considering the transformations that occur along the X, Y, Z axes and it is mainly applied to the head. However, it proves insufficient for the heart and lungs, which exhibit more complex deformations. Non-rigid registration, in addition to considering translational and rotational movements, incorporates bending, compression, and stretching. Examples include the software Q.Freeze (GE) and OncoFreeze (Siemens) [41], which use elastic

transformations between the respiratory phases to obtain a stable final image. This significantly improves the visual and quantitative quality of PET imaging.
In recent years, machine learning techniques have been applied to thoracic breathing, enabling a better estimate of the motion patterns. Furthermore, these methods show an improvement in the levels of image quality and accuracy [6, 28].

Figure 3.3 shows a summary diagram of the different motion compensation techniques for each organ. Hardware-driven gating methods have the advantage of monitoring tracking in real-time, providing direct feedback of the patient's breathing and cardiac cycle, making the approach the gold standard in dynamic or time-sensitive imaging protocols. The major limitation of these techniques is the inability to monitor internal organ movements, which makes them less useful for tracking respiratory motion. In contrast, data-driven gating techniques rely on PET data to identify motion patterns and correct them. They do not require additional devices or sensors, thus rendering them more cost-effective and versatile. However, they are highly sensitive to noise and irregular movements. Furthermore, the success of motion correction relies on how good and accurate the collected data is: if the image contains a lot of noise, the method for data-driven gating does not produce great outcomes. A limitation common to both techniques is their limited capacity to incorporate multiple organs and, consequently, multiple motion sources in these compensation approaches [6, 28].

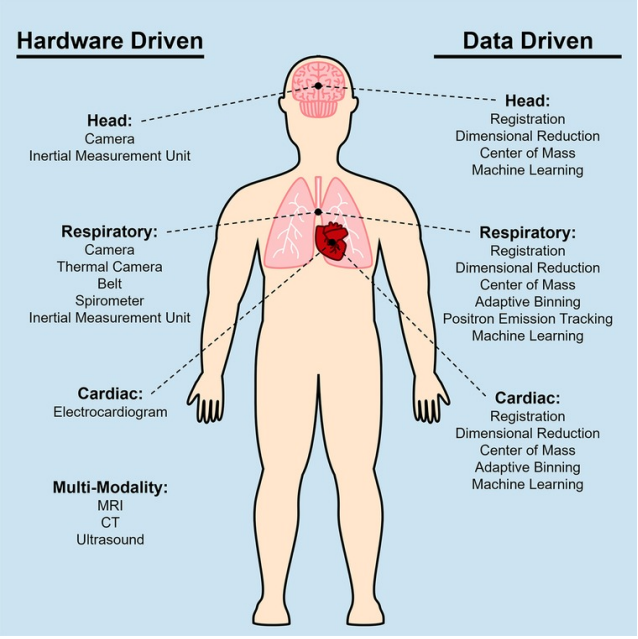

Figure 3.3: Types of motion compensation techniques for PET imaging [6].

3.3 Image Registration and Motion Correction

Motion artifacts caused by respiratory and cardiac movements significantly degrade the quality of the reconstructed PET images, leading to inaccurate diagnoses. Various motion compensation techniques have been presented to compensate for these artifacts. Most of them require external devices around the scanner, such as a camera or markers attached to the patient's body to track motion. However, due to the difficulty in accurately estimating internal organ movement, this type of approach remains secondary. Data-driven approaches are mostly implemented because they do not require additional setup, as they extract the necessary information directly from the data, with image registration being one of the main methods employed.

Image registration is mainly used to address motion artifacts and to integrate or compare images obtained from different imaging modalities (MRI, CT, PET, etc.). Registration is an alignment process of two images into a common coordinate system by determining a geometrical transformation that maps points from one image to another. After the alignment, a reoriented version is obtained. These reoriented images can then be combined into a fusion version of them, which consists of simply summing all the intensity values across the images [42].

There are many types of registration methods that differ from each other based on their characteristics. The main criteria for classifying them are the following:

- **Image dimensionality**: the number of geometrical dimensions of the image spaces involved, typically 3D, although sometimes 2D applications are possible;
- **Registration basis**: the aspect of the two views utilized to achieve registration. This can be extrinsic (involving an external object within the image), intrinsic (derived from the image data), or non-image based (matching the imaging coordinates from both devices);
- **Nature of transformation**: rigid, affine, projective, or nonlinear;
- **Domain of transformation**: global or local based on the part of the images registered;
- **Degree of interaction**: the extent of control a human operator has over the registration process. It may be interactive, automatic, or semi-automatic;
- **Optimization procedure**: a standard method where the quality of registration is continuously assessed during the process by applying a function related to the images and their mapping;
- **Modalities**: the various forms of image capturing. If both images are from the same modality, it is termed "monomodal"; if they differ, it is "multimodal";
- **Subject**: the participation of the patient in the registration process. If both images depict the same patient, it is referred to as "intrasubject" registration; if they represent different patients, it is "intersubject" registration;

- **Object**: the specific anatomical area that is being registered. [42, 43]

Regardless of the classification, image registration is based on a geometric transformation process from a point in X space to the same point in Y space. When the transformation T is applied to a point x in X, a new transformed point x' is obtained, described by the following formula:

$$x' = T(x) \tag{3.1}$$

If a point x in the space of the first image corresponds to the point x' in the second image, then a successful registration will cause x and x' to coincide or be approximately equal.
Geometric transformations can be divided into two main approaches: rigid and non-rigid, depending on the nature of the images and the motion to be corrected.
Rigid registration is based on transformations that involve only rotations and translations without any internal deformation of the anatomical structures. This type of registration maintains the alignment of lines, the flatness of surfaces, and the spacing between anatomical features. Rigid registration is preferable when the aim is to align bone structures and rigid objects without changing their shape. Mathematically, the rigid transformation can be represented as:

$$\mathbf{x}' = R\mathbf{x} + \mathbf{t} \tag{3.2}$$

where $\mathbf{x}$ refers to the original coordinates of the point, R is the 3×3 orthogonal rotation matrix, and $\mathbf{t}$ is the translation vector. This approach is particularly useful when images are acquired under similar conditions, but may exhibit slight variations in orientation or position. In such cases, rigid registration can correct for both translation and rotation. However, when local deformations are present, rigid registration becomes insufficient [42].
The second approach, which better performs in local deformations, is non-rigid registration. This is ideal for modeling the movement of internal organs involving compression, bending and warping. It is a more complex method to implement as it accounts for local deformations of individual anatomical structures. Non-rigid registration uses a local deformation field, dynamically changing the position of each point in the image, making the registration more flexible. It works very well in cases of respiratory and cardiac motion, allowing for accurate tracking [42].
The simplest non-rigid transformation is the scaling transformation. Mathematically, it is represented as follows:

$$\mathbf{x}' = RS\mathbf{x} + \mathbf{t} \tag{3.3}$$

where $S = \text{diag}(s_x, s_y, s_z)$ is a diagonal matrix, and each diagonal entry represents a scale factor along the x, y, and z axes. If the scale factors are identical, the scaling is isotropic; otherwise, it is anisotropic. Scaling transformations modify the dimensions of objects along the three axes, making them an ideal method for correcting calibration errors in imaging systems. Scaling transformations are a particular case of affine

transformations [42].
Affine transformations preserve straight lines and planarity, but angles and lengths can change. They are used when the object in the image is not only scaled and translated but also rotated and sheared. The affine transformation is described by the formula:

$$\mathbf{x}' = A\mathbf{x} + \mathbf{t} \tag{3.4}$$

where A is a generic matrix, not necessarily diagonal.
The third option is the projective transformation, that, in contrast to scaling and affine transformations, maintains the straightness of lines and flatness but does not keep parallel lines. Projective transformations have the following form:

$$\mathbf{x}' = \frac{A\mathbf{x} + \mathbf{t}}{p\mathbf{x} + \alpha} \tag{3.5}$$

It is often written more simply using homogeneous coordinates, which combine rotation and translation into a single matrix [42].
Another possibility is the perspective transformation, which relates three-dimensional anatomy to two-dimensional planar images acquired via a pinhole camera, where a small hole substitutes for a lens system. Perspective transformation is usually used when tomographic images are combined with X-ray projection or photography. The concept is described by the following equation:

$$\mathbf{x}' = f\mathbf{x}/(\mathbf{x} \cdot \hat{\mathbf{p}} + \alpha f) \tag{3.6}$$

The value f is referred to as the focal length or "camera constant". The term "focal length" comes from optical lens systems [42].
The final choice is the curved transformation, which does not maintain the linearity of lines. The model is of polynomial type, in which the $\mathbf{x}'$ component is calculated considering the parameter c_{ijk}, a three-element vector of coefficients for the i, j, k terms corresponding to x', y', and z', respectively:

$$\mathbf{x}' = \sum_{ijk}^{IJK} c_{ijk} x^i y^j z^k \tag{3.7}$$

Splines (especially cubic B-splines) are often used to manage curved transformations smoothly [42].

In summary, rigid registration is simpler and faster but is limited by its inability to handle local deformations. Non-rigid registration, being more complex and computationally intensive, is essential for aligning images that require modeling of local deformations, such as those associated with motion or physiological changes.
Both rigid and non-rigid registrations are performed with imaging software tools. MRtrix3 and Advanced Normalization Tools (ANTs) are two of the most commonly used software to perform registration. For both, the focus is on the nonlinear

registration, since this is the object of discussion in this dissertation.

3.3.1 MRtrix3 for Motion Correction

MRtrix3 is an open-source software for medical image analysis and visualization, providing a set of tools to perform various types of diffusion MRI (DWI) analysis. While the software is developed primarily for MR imaging, the image registration tools can also be used for other imaging modalities. The software primarily works on image processing, including image filtering and calculation, statistics, denoising, intensity normalization, and diffeomorphic image registration. MRtrix3 employs a method based on symmetric diffeomorphic registration, which aligns images while preserving anatomical topology and producing invertible transformations [44].
During image registration, the two images are compared using metrics such as:

- **Mean Squared Difference (MSD)**: based on the quadratic difference of the spherical harmonic coefficients;
- **Cross-Correlation (CC)**: adjusted to accommodate local variations in intensity in inter-subject recordings.

MRtrix3 implements this algorithm in the mrregister command, returning a voxel-wise vector field from which the Jacobian matrix J is derived. This matrix describes the local deformations of each voxel with respect to the reference image. The Jacobian determinant can be used to quantify structural changes: a value greater than 1 indicates local expansion, while a value less than 1 indicates contraction. This registration strategy enables highly sensitive alignment to local image geometry and can be applied not only to MRI but also to other imaging modalities, such as PET [44, 45, 46].

In practice, image registration in MRtrix3 was performed using the "mrregister" command. This command allows to co-register two images, a moving one and a reference one called "template" using rigid, affine, and non-linear models. The most used pipeline is the one that involves the application of an affine transformation followed by a non-linear one. All transformations work in the same way: both reference and moving images are matched in a 'midway space' in order to maximize the morphological correspondence between them. The basic form of implementation described in [47] is the following:

```
mrregister [options]  image1 image2 [contrast1 contrast2...]
```

where image1 is the moving image and image2 is the template; contrast1 and contrast2 are additional input images used as additional contrasts; options depend on the registration performed. One of the fundamental aspects of the nonlinear transformation concerns the prediction of the two deformation fields: the first that maps the moving image on the reference image, while the other does the inverse [47].

Although MRtrix3 is widely used for MRI images, it is not the best software for other types of analysis such as CT or PET. Its main disadvantage concerns the excessive computational time required to register images, making it a non-optimal choice. Other software such as ANTs are better for image registration, especially non-rigid registration, due to the low computational cost required.

3.3.2 Advanced Normalization Tools for Motion Correction

To perform deformable image registration, this work uses the Advanced Normalization Tools (ANTs) framework, an open-source software widely adopted in biomedical image processing. The main advantage of ANTs lies in its low computational cost: the time required to align two images of size (350, 200, 500) voxels is about 1-2 minutes, compared to the 15 minutes required by MRtrix3 without compromising registration quality.
ANTs uses the standard ITK toolkit format to define images, specifying orientation, direction, voxel spacing, and origin. It is based on the same mechanism as MRtrix3: it maps moving images to the template or vice versa through symmetric diffeomorphic registration. However, while both frameworks use this principle, ANTs specifically relies on the Symmetric Normalization (SyN) algorithm for its registration process [48].
SyN is one of the most advanced and robust algorithms for deformable registration, since it preserves the topology of anatomical structures during transformation. The principle behind SyN consists of the optimization of a stationary velocity field, from which invertible deformations between the fixed and moving image are generated. This makes it particularly useful for images that contain moving organs, such as the lungs [49].

ANTs supports several similarity metrics to evaluate alignment quality during the optimization process:

- **Cross Correlation (CC)**: measures the linear relationship between voxel intensities and it is suitable for intra-modality image registration;
- **Mutual Information (MI)**: captures statistical dependence between intensity distributions. It is effective for both intra-modality and inter-modality registration;
- **Mean Squares (MSQ)**: computes the average squared intensity difference between corresponding voxels. It is limited to only intra-modality registration due to its sensitivity to intensity mismatches and noise [49].

The image registration performed using ANTs toolkit employed the SyN transformation model and MI as the similarity metric, suitable for intra-modality alignment. A multi-resolution optimization scheme with smoothing and progressive downsampling was used to improve convergence and accuracy. Full implementation details and parameter settings are provided in Appendix A.

In summary, the implementation of the ANTs framework for image registration has proven to be the best choice in terms of accuracy, flexibility, and speed. For this reason, although MRtrix3 was initially used, ANTs was adopted for the rest of the thesis. The SyN algorithm combined with MI metric guarantees precision and consistency even when there are considerable differences between images. The combination of multi-resolution techniques and parameter flexibility contributes to the achievement of realistic and smooth deformations in minimal time. Such characteristics enhance the reliability of ANTs as a component in complex biomedical image processing pipelines [48].

Chapter 4

Methods

In this section, the workflow of the proposed method for performing motion correction due to respiratory motion in the WT-PET is presented. The steps include PET data simulation, image reconstruction process, motion correction achieved through frame alignment, and visualization and assessment of lesions using detectability metrics.

4.1 PET Data Simulation

4.1.1 Simulation Methodology

In the past years, the evaluation of imaging devices was mainly based on commercial devices. Later, several methods have been developed to predict and evaluate their performance. The ability to simulate the imaging process mechanisms has become increasingly important in order to evaluate system performance prior to its physical construction. Among these methods, the Monte Carlo method is the most widely adopted to design and optimize imaging systems such as PET and SPECT (Single Photon Emission Computed Tomography). Some packages have been developed to support such simulations, which are GEANT3, EGS4, MCNP, GEANT4. These packages are highly accurate since they incorporate robust and validated physics simulations, geometry design tools, and advanced visualization modules. These packages are highly sophisticated and require a very long learning time in order to effectively utilize them [50]. Therefore, GATE (GEANT4 Application for Tomographic Emission) has been developed as an evolution of GEANT4, encapsulating all its libraries while adapting them to the field of nuclear medicine. GATE Monte Carlo combines the positive aspects of GEANT4 such as the sophisticated ability to model geometry with 3D tools and physical models, and more innovative features such as the synchronization of all time-dependent components and source kinetic decay, allowing a more realistic description of the acquisition process [50].
One of the main advantages of using GATE software is its combination of accessibility, reusability, and modularity. In fact, it does not require C++ knowledge, and its components adapt to different clinical scenarios. A major feature is the management of time-dependent phenomena. The synchronization of the radioactive

source kinetics and geometry movements, such as scanner rotation or respiratory and cardiac movements, allows obtaining a realistic simulation of the image acquisition conditions. The frame acquisition times are divided into smaller time steps and the synchronization between the movements and the evolution of the source activities is performed for each time step. This approach also enables the modeling of realistic temporal variations of the activity distribution, leading to a more accurate estimation of count rates over time [51].
The source in GATE is defined by the particle type (e.g. positrons, radionuclides, gamma photons), spatial and angular distributions, energy, and activity. For PET systems, two simulation methods are incorporated: the first uses the von Neumann algorithm that generates positrons according to the measured $\beta+$ spectra; the second simulates the acollinearity of the annihilation photons by applying a Gaussian blur. Photoelectric absorption and Compton scattering are simulated, as they contribute significantly to image degradation. The materials are specified, including density, elemental composition, and atomic number. Interactions between radiation and body tissues are also accounted for. Even for coincidences in PET, simulations include true, scatter and random coincidences. This is achieved by defining a coincidence window that discriminates simultaneous events and discards non-true coincidences. The output data are saved as a list of events (PET list-mode) in which each event includes the position, time, energy, and type of interaction [51].
GATE thus provides a flexible and complete environment for realistic PET simulations.

4.1.2 Data and Phantom Characteristics

In the present study, GATE is used to simulate 60 seconds of PET data acquisition, modeling scenarios with and without respiratory and cardiac motion. These simulations provide a realistic framework for evaluating the impact of motion and the effectiveness of subsequent correction strategies. The resulting list-mode data are then used as input for image reconstruction, as described in Section 4.2. The data are simulated with anthropomorphic XCAT phantoms, whose activity distribution is based on FDG. The different phantoms differ in their characteristics, including age, weight, height, sex. For the purpose of this study, the phantoms identified as numbers 71, 164, and 184, with BMI of 18.64, 28.22, and 37.96 respectively, are considered. The characteristics of each phantom are summarized in Table 4.1:

Table 4.1: Personal data and anthropometric parameters of the phantoms analyzed.

Code	Sex	Age	Gender	Weight (kg)	Height (cm)	BMI
71	Female	27	F	55.6	172.7	18.64
164	Male	67	M	89.9	178.5	28.22
184	Male	50	M	120	177.8	37.96

4.2 Image Reconstruction

In Section 2.2, the topic of image reconstruction was addressed, analyzing the two main techniques: analytical reconstruction using FBP and iterative reconstruction based on the MLEM algorithm. The second approach is the one currently used in PET devices, given the better spatial resolution, better SNR and better accuracy, despite the higher computational cost.

4.2.1 Formulation of the Reconstruction Model

Before performing the actual reconstruction, it is necessary to configure the reconstruction software, adapting it to the new WT-PET design compared to the conventional cylindrical PET scanner. One of the reconstruction algorithms used for PET, SPECT, and CT images is the CASToR (Customizable and Advanced Software for Tomographic Reconstruction) framework implemented in C++. Although this has demonstrated high performance without compromising the computational cost, it does not offer good adaptability for Walk-Through PET [52].
For this reason, Ghent research group has developed a custom image reconstruction framework, PETRecon, which offers high performance and efficiency, written in Julia, an high-level programming language featuring just-in-time (JIT) compilation. The most computationally expensive parts are done in GPUs (Graphic Processing Units), using NVIDIA's CUDA toolkit [53].
First, the setup is virtualised: the scanner configuration consists of two flat panels of dimensions 70 x 106 cm composed of scintillators with dimensions 16 x 50 x 50 mm^3. Figure 4.1 illustrates how the WT-PET scanner is modeled, showing the geometric configuration of the panels and the presence of gaps between the detectors.

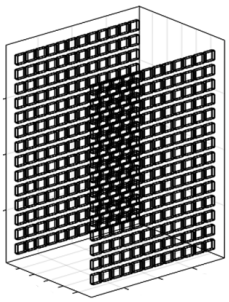

Figure 4.1: Model of the WT-PET scanner with detector gaps.

Subsequently, the acquired data is stored in list-mode format, where each event corresponds to a single detected LOR. This format is particularly suitable when the number of possible LORs is large. Importantly, only true coincidences are considered for reconstruction, as the simulated data allow the removal of scatter and random events before the reconstruction step. Consequently, scatter and random corrections are not required during the reconstruction process. The image reconstruction problem

can be formulated as:

$$\lambda_j^{(k+1)} = \frac{\lambda_j^{(k)}}{\sum_{i \in I} H_{ij}} \sum_{i \in E} \frac{H_{ij}}{\sum_{j' \in J} H_{ij'} \lambda_{j'}^{(k)} + e_i} \tag{4.1}$$

where the sum over I is a sum over all potential LORs, the sum over E is a sum over the detected LORs, the sum over J is a sum over the voxels, H is the system matrix response, and e is the additive noise [53].
The system response matrix (SRM) models the probability that an emission from voxel j is detected along LOR i, based on a virtual scanner geometry. It takes into account multiple components such as geometric sensitivity, TOF information, attenuation in the object, detector attenuation, and normalization. In this way, the reconstruction process ensures that different physical effects contribute to image formation. The image reconstruction process involves iteratively updating the image estimate using the SRM components described above. Before the reconstruction, the list-mode data undergo several pre-processing steps, such as spatial and time blurring to account for the scanner's physical properties. Specifically, the detector resolution includes both 2D transverse resolution of 1.3 mm FWHM in both the x and y directions, and a DOI resolution of 2.0 mm, while the time resolution used in the TOF model corresponds to 300 ps FWHM [53]. The approach is the MLEM algorithm, which updates the image by maximizing the likelihood of the observed data given the model. A voxel size of $2 \times 2 \times 2$ mm^3 is used, and the number of iterations is set to 5.

4.2.2 Implementation Framework

In order to evaluate the effectiveness of motion correction, different types of reconstructions are performed, varying by the acquisition duration and the segmentation in temporal frames. In particular, the following approaches are performed:

- **Full 60 s**: all the raw data acquired in the interval 0-60 s are reconstructed in a single frame;
- **Stride of 0.3125 s**: the data are divided and reconstructed into consecutive frames, each of duration 0.3125 s. For example, the first frame corresponds to the interval 0–0.3125 s, the second to 0.3125–0.625 s, and so on;
- **Stride of 0.9375 s**: similar to the previous case, but with a temporal separation of 0.9375 s between one frame and the next;
- **Stride of 0.3125 s with frame length of 0.9375 s**: combines the second and the third approach. The length of each frame is 0.9375 s, but each frame is generated 0.3125 s after the previous one. This results in a temporal overlap between successive frames: each frame shares 0.625 s with the previous.

These reconstructions are performed under different conditions. Initially, simulated data are analyzed without the presence of lesions, both in static conditions and in the

presence of respiratory and cardiac motion. Subsequently, the attention is focused on datasets containing four lesions with a diameter of 10 mm, two of which in the lung and two in the liver. The lesions are inserted into three different phantoms, corresponding to simulated subjects with different BMI (Body Mass Index) values, in order to evaluate the impact of the body type on reconstructive quality.

4.3 Motion Correction

After performing the PET data simulation and the short-frame reconstruction, it was possible to proceed with motion correction. The simulated PET data was provided as part of the available dataset, while the short-time frame reconstruction was carried out using the available software tools. This correction was performed using the ANTs software, as described in Subsection 3.3.2. The underlying process of co-registration is as follows: reconstructed short-time frames are non-rigidly aligned to a reference frame using the SyN algorithm. The reference frame was chosen corresponding to time 0 s, while all subsequent images are considered the moving images. For example, in the reconstruction with stride 0.9375 s, the alignment occurs as follows:

- The frame (acquired at 0.9375 s) is registered with respect to the frame at 0 s;
- The next frame (at 1.875 s) is also registered with respect to the frame at 0 s;
- This process continues for all subsequent frames, always aligning them to the initial template.

Following the co-registration, a series of spatially transformed images is obtained. The next step is the calculation of the voxel-wise mean of the series of such corrected images. To this end, the "mrcalc" command of MRtrix3 was used, which sums the images voxel by voxel and divides the result by the total number of images, thus obtaining the mean for each voxel. This approach allows synthesizing in a single mean image the spatial information coming from multiple iterations or subsets of the reconstruction process, reducing noise and facilitating subsequent quantitative analysis. Furthermore, the voxel-wise mean allows a direct comparison between the different simulations, clearly highlighting the difference between the cases in which the motion correction was applied and those in which it was not performed. Finally, this average image also made it possible to directly compare the short-time frame reconstructions with the complete 60-s reconstruction, in which a single image is obtained that encompasses the entire temporal acquisition.

4.4 Visualization on AMIDE

The 3D images obtained are visualized using AMIDE (Amide's a Medical Image Data Examiner), an open-source software developed for the analysis of multimodal volumetric medical images, such as PET, CT, and MRI. This choice is motivated by many advantages offered by the software, including a simple and intuitive interface,

the simultaneous visualization of multiple data sets and an immediate comparison between them, and the Region of Interest (ROI) selection functionality, useful for isolating specific lesions and conducting a detailed quantitative analysis [54].
The images obtained by averaging the reconstructed short-time frames were saved in the NIfTI format (Neuroimaging Informatics Technology Initiative), a widely used file format for medical imaging data. These NIfTI images were then loaded into the software, allowing the different projections to be displayed: transverse, coronal, and sagittal. By changing the coordinates along the three directions, it was possible to explore various details and sections of the acquisitions. One of the most useful features for this study was the ability to directly compare the images, displaying them side by side. The differences between them were visually examined, adjusting the color range in case of overlap. These features of AMIDE were fundamental in the image analysis and comparison phase, facilitating the interpretation of the simulation data.

4.5 Lesion Analysis

4.5.1 Region Growing for Lesion Segmentation

Among the datasets simulated using GATE Monte Carlo, there are cases with four thoracic lesions distributed in two anatomical locations: two in the right lung and two in the liver. The lesions are modeled as spheres of 10 mm diameter with tumor-to-background activity concentration ratio of 8:1. The identification of pathologies is the basis of the medical imaging process to allow the start of the diagnostic-therapeutic process. Image segmentation is the basis of the lesions' characterization. Segmentation is a method that divides images into different regions that have the same characteristics such as texture, intensity, or gray level, allowing to effectively distinguish anatomical or functional structures from the background [55]. To this end, this study adopted the region growing algorithm, a technique based on the division of images into homogeneous regions with similar properties. The algorithm is divided into the following steps:

- **Selection of the seed point:** starting point from which the algorithm starts, selectable manually or automatically;
- **Similarity criterion:** a pixel near the seed point is added if it satisfies a similarity criterion, defined in terms of intensity (or color) with respect to the seed;
- **Iterative growth:** it includes voxels until they satisfy the criterion;
- **Stop criterion:** the growth ends when there are no more pixels to add or a predefined maximum limit is reached.

The main advantages are its intuitiveness and ease of implementation. It is mainly based on a pixel comparison mechanism, which makes the algorithm straightforward

to develop. However, the computational cost is high. Other limitations are the sensitivity to noise and the choice of the seed. Based on criteria chosen independently, the parameters must be empirically optimized. Furthermore, if the images are noisy or the contrast between regions is not clear, it is difficult to find a good segmentation [56, 55].

In this study, the algorithm was implemented in Python and applied to the images obtained after co-registration of the reconstructed short-frames and after reconstruction in 60 s. In both cases, the resulting images were first filtered with a median filter, using the filtering tool integrated in AMIDE, to reduce noise and remove outliers. To perform lesion segmentation, it is essential to select the seed point, which is chosen based on the statistical description extracted from each lesion. This information is obtained by defining in AMIDE four elliptical ROIs that contained the entire volume of the lesions. The dimensions of the ROIs varied from 25–30 mm for images without motion correction to 15–20 mm for images with motion correction. For each of the identified ROIs, the descriptive statistics (maximum, mean, median, standard deviation, volume) are calculated using the "ROI Statistics" function of AMIDE. Once these parameters were obtained, the next step is to select the seed point.

For the liver, the seed point was automatically selected as the voxel with intensity equal to the maximum value of the ROI, limiting the search to the central portion of the image, anatomically corresponding to the thorax area. It was not necessary to specify many other parameters to be sure to obtain the correct seed point, since the liver, due to its high uptake of the FDG tracer, has significantly higher intensities than other tissues. The result is that the seed point found is exactly the one searched for inside the lesion. The expansion of the region is performed by evaluating the 6 adjacent voxels. Each voxel is included in the region if its intensity is greater than the threshold, which is manually selected based on the mask obtained and by examining line profiles across the lesion to better capture intensity variations. For the liver, the threshold values generally vary from 50% of the maximum value of the ROI in cases with motion correction to 80% in cases without. To avoid excessive growth due to noise or adjacency to highly active tissues, the procedure is forcibly stopped if the number of included voxels exceeds 50,000, as a computational safety measure. This results in a binary mask for liver lesions.

For the lung, the seed point has always been chosen as the voxel with intensity equal to the maximum of the ROI, with a further spatial restriction: the point must be within the radius of 20 voxels with respect to the position of the lesion inserted at time 0 s. The union of these two conditions ensures that the seed point is correctly selected within the searched area. This is essential in the case of the lung in which the activity distribution is low and the contrast with respect to the background is reduced. Also in this case, the expansion occurs for connectivity 6 and ends when the maximum number of voxels is exceeded. However, the threshold is equal to 40% of the maximum value of the ROI. This results in a binary mask for the lung.

This procedure is manually repeated for each of the four lesions in each dataset. The resulting binary masks accurately represent the volume of the simulated lesions, with a greater extension in cases where motion artifacts are present. Further details on the quantitative segmentation results are discussed in Chapter 5.

4.5.2 Detectability Metrics and Evaluation Criteria

After obtaining the lesion masks using the region growing method described in Subsection 4.5.1, it is possible to proceed with the quantitative analysis. The objective is to verify that the segmented masks faithfully reflect the expected characteristics in terms of size and intensity, and to evaluate the quality of the reconstructed image through quantitative metrics. Detectability metrics allow us to have knowledge of the size of the lesions, how distinguishable they are from the background and healthy tissues, and how noisy the image is.
To perform quantitative analysis, three different metrics are analyzed to compare the different image reconstruction methods, with particular attention to the effect of motion correction. The application of motion correction is expected to improve the metric values, indicating a higher image quality and better identification of the lesions. Detectability metrics were also useful to compare reconstructions obtained from different short-time frames, with the aim of identifying the optimal trade-off between temporal resolution and noise. Theoretically, shorter frames are expected to allow better motion tracking but are more sensitive to noise.
The first metric analyzed is Contrast-to-Noise Ratio (CNR), which quantifies the lesion detectability against the background. It is calculated as follows:

$$\mathrm{CNR} = \frac{|\mu_L - \mu_B|}{\sigma_B} \tag{4.2}$$

where μ_L is the mean intensity of the lesion voxels, μ_B is the mean intensity of the background voxels and σ_B is the standard deviation of the intensity in the background. A higher CNR value indicates that the lesion is more easily distinguishable from the background [57].
The second metric is the Contrast Recovery Coefficient (CRC), which measures the accuracy in recovering the true lesion contrast. It does not directly measure visibility, but contrast fidelity. CRC is defined as follows:

$$\mathrm{CRC} = \frac{\left(\frac{\mu_{\mathrm{lesion}}}{\mu_{\mathrm{background}}} - 1\right)}{\left(\frac{a_{\mathrm{lesion}}}{a_{\mathrm{background}}} - 1\right)} \tag{4.3}$$

where μ_{lesion} is the mean intensity of the lesion voxels, $\mu_{\mathrm{background}}$ is the mean intensity of the background voxels, and a_{lesion} and $a_{\mathrm{background}}$ are the known activity concentrations of the phantom spheres, equal to 8 and 1, respectively. The CRC value ranges from 0 to 1, where 0 indicates no contrast recovery (lesion similar to background), and 1 indicates perfect recovery (lesion eight times more intense than background) [57].

The third metric used is the Metabolic PET Lesion Volume (MLV), which evaluates lesion size. It is calculated as the product of the number of voxels belonging to the lesion region of interest and the volume of a single voxel ($2 \times 2 \times 2$ mm^3 = 8 mm^3). Considering that the lesions inserted into the phantom are spherical with a diameter of 10 mm, the theoretical expected volume is about 524 mm^3. This reference value is useful for evaluating the accuracy of lesion segmentation in volumetric terms, comparing the volume obtained with the expected volume [58].

In summary, the entire methodological framework consists of PET data simulation, image reconstruction, motion correction and lesion segmentation. Detectability metrics are used to evaluate both lesion detectability and segmentation, focusing on the differences between the different reconstructions performed. The results derived from these evaluations are presented and interpreted in the following chapter.

Chapter 5

Results and Discussion

Chapter 4 described the motion correction workflow, including PET data simulation, image reconstruction process, motion correction through image registration, and visualization and analysis of lesions. This chapter analyzes the results obtained, illustrating the impact of motion in WT-PET images, the effect of motion artifact correction, and lesion detectability. The following analyses are conducted on three different phantoms, highlighting the influence of BMI on image quality. Section 5.1 reports the results of MRtrix3, while the rest of the chapter employs ANTs.

5.1 Demonstration of Motion Correction Effectiveness

In Chapter 3, the description of MRtrix3 has been proposed. The software used the 'mr-register' command for performing image co-registration. To visually illustrate the effect and importance of motion correction, a simple test was conducted using two frames from a 60-second PET simulation. The template corresponds to the frame at instant 0 s, while the moving image is the frame at the subsequent instant, i.e. 1 s. Figure 5.1 shows the result of the image registration process. The difference between the two is minimal because of the graininess of the image, which causes a lack of clarity in its visualization. However, it can be noted that in the image with registration, the structures appear better superimposed, indicating that they match better than in the case in which registration does not occur. This is noted by observing mainly the liver, where the effect is more intuitive. In the first case, slight misalignments are present in the chest and pelvic area, where the distribution of red points (frame 0 s) and blue points (frame 1 s) do not coincide perfectly. In part B both components appear together, without a clear recognition of the prevalence of one over the other, almost as if there had been a fusion.

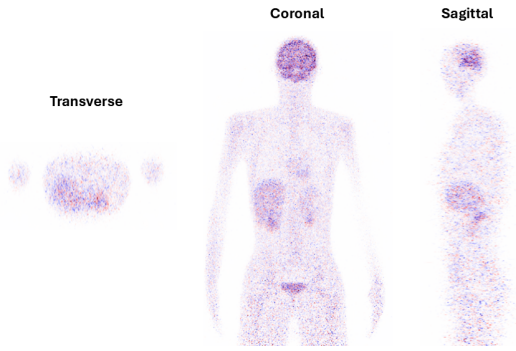

(A) No image registration

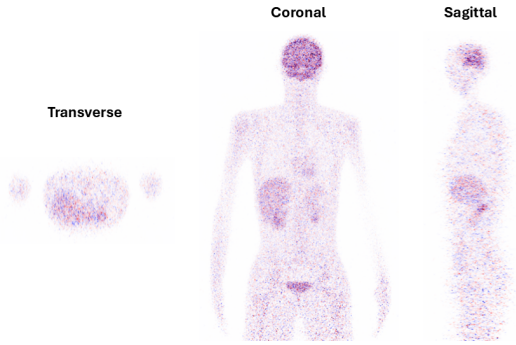

(B) With image registration

Figure 5.1: (A) shows the superposition of two frames at 0 s and 1 s without the image registration process. (B) shows the superposition of two frames at 0 s and 1 s after the second frame has been registered on the first one. The reference frame is shown in blue, the motion frame in red.

In addition, during the registration, the deformation field was also saved and used to map the moving image to the reference image. This field was then applied to the two frames of the same time instants (0 s and 1 s) of the activity maps, which represent the ground-truth metabolic or functional activity distributions used in the simulation to generate the PET images, with the built-in MRtrix3 function "mrtransform". This function applies any type of spatial transformation to an image [59]. In part B of Figure 5.2, thanks to the applied transformation, the anatomical structures appear to be well superimposed, suggesting the effectiveness of the registration. In contrast, in part A, which shows the untransformed version, misalignments are evident, in particular in high-activity areas such as the liver, heart, and pelvis, where the signal distribution is less coherent between the two moments.

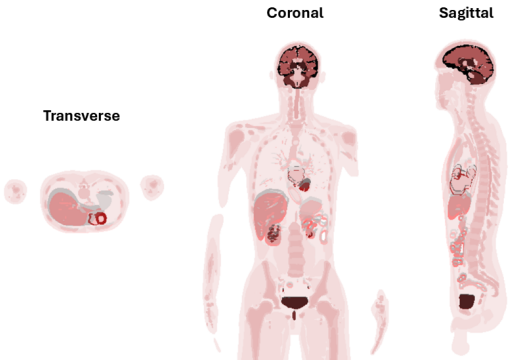

(A) No image registration

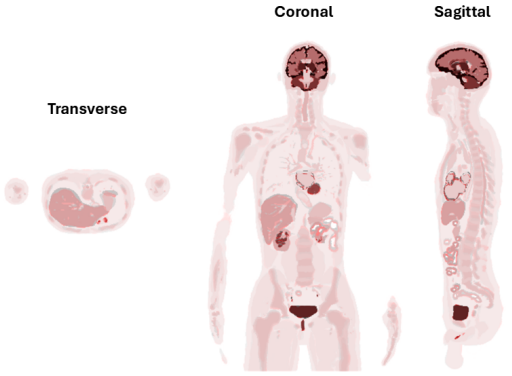

(B) With image registration

Figure 5.2: (A) shows the superposition of two activity maps at 0 s and 1 s. (B) shows the same superposition after applying the deformation field obtained from image registration process. The reference frame is shown in grey, the motion frame in red.

This initial demonstration confirms the usefulness of motion correction before evaluating its impact on diagnostic metrics and image quality in the full simulated datasets.

5.2 Simulation without lesions

5.2.1 Impact of Motion Correction

Cardiac and respiratory motion compromise image quality, resulting in poor definition of anatomical structures, an excessively smoothed appearance of images, and inaccurate localization of lesions, which can lead to either interpreting pathological tissues as healthy or classifying healthy tissues as pathological. In this context, motion correction is essential to address this motion artifact. The impact of motion on the image is illustrated in Figure 5.3. Part A of the figure shows the simulation of 60 seconds of PET data without any simulated motion, representing the ground truth that the motion correction technique aims to achieve. Part B of the figure represents a simulation of the same duration, in which breathing and cardiac motion is present but uncorrected. It is clear that, when motion is present, the image is

blurry and the anatomical structures are less defined: in particular, this is noticeable at the lung-liver edges. The result of motion correction is evident in Figure 5.3, part C, where a short-time frame reconstruction was performed with a stride of 0.9375 s between frames. The displayed image corresponds to the voxel-wise mean of the 64 reconstructed frames. With motion correction, image resolution improves and the boundaries of the organs are more defined compared to part B. The motion correction is therefore effective, even though the image is not as sharp as in the ground truth.

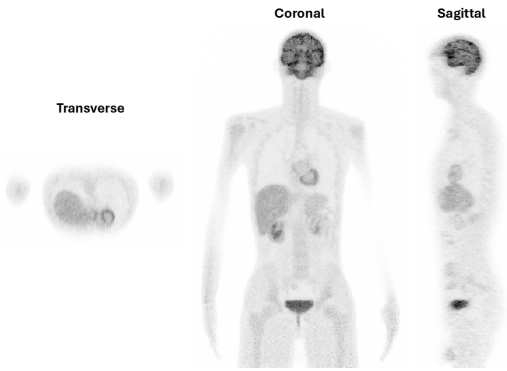

(A) Full 60-s reconstruction without motion

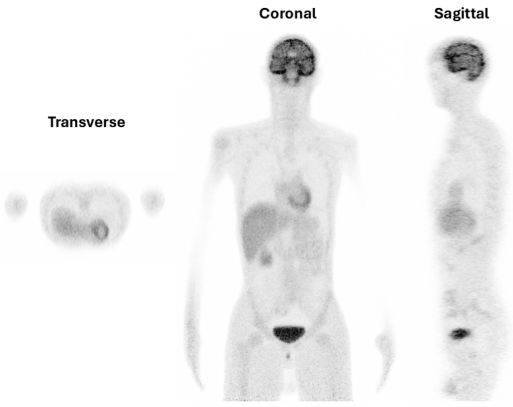

(B) Full 60-s reconstruction with motion

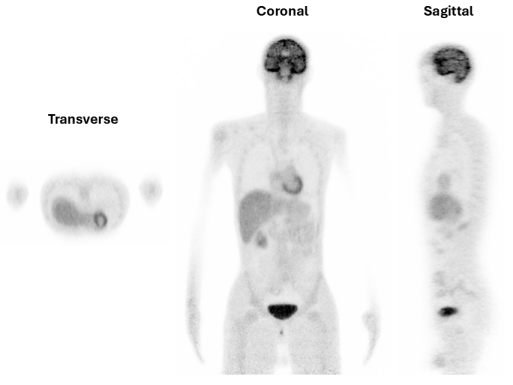

(C) Short-time frame reconstruction with motion correction

Figure 5.3: Representation of motion correction effectiveness. (A) 60-second reconstruction without respiratory and cardiac motion. (B) full 60-second reconstruction with respiratory and cardiac motion, but without correction. (C) 0.9375-second frame reconstruction after motion correction.

5.2.2 Impact of Summing Frames

The effectiveness of motion correction has been demonstrated in Subsection 5.2.1. Although it has proven to be effective, the image is still not as well-defined as when the motion is not present. This is mainly due to the choice of frame duration in image reconstruction and to the effect of averaging the frames to obtain a final image. However, the main reason is that the motion correction workflow is not perfect, and residual motion is still present in the final image. As described in Chapter 4, after performing the short-time frame reconstruction, all the frames are averaged voxel by voxel in order to obtain an average image that can be more easily compared with other reconstructions. However, this averaging process reduces image quality. In Figure 5.4 the simulations without motion of full 60 s reconstruction (A) and short-time frame reconstruction of 0.9375 s stride (B) are compared. It is evident that, beyond the regions where the edges appear smoother, the overall image quality is poorer.

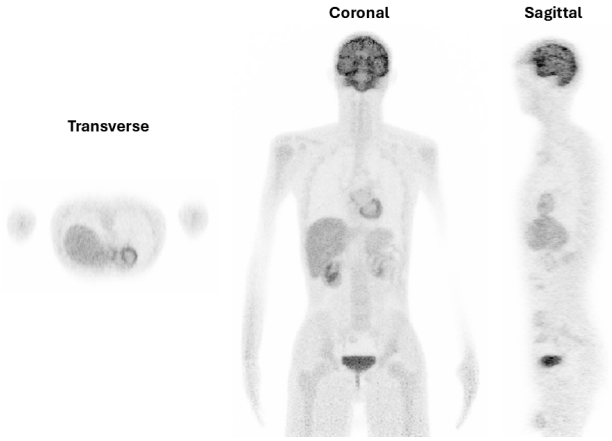

(A) Full 60-s reconstruction

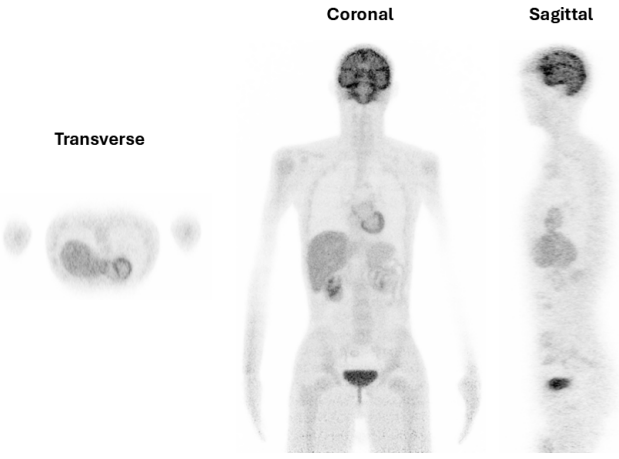

(B) 0.9375-s frame reconstruction

Figure 5.4: Impact of summing frames. (A) is the full 60-s reconstruction. (B) is 0.9375-s frame reconstruction (average of 64 frames). Both are without motion.

This effect is also confirmed by the line profile analysis obtained by AMIDE in Figure 5.5. The two curves, one from the full 60-s reconstruction (blue) and one from the 0.9375-s frame summation (orange), appear largely similar in shape and intensity. However, the orange curve exhibits slightly more local fluctuations, which is consistent with the increased noise expected from shorter frame reconstructions. Although the overall intensity profiles are comparable, these subtle variations suggest a modest degradation in local image stability due to residual noise.
Despite this, the calculation of the global standard deviation of the two images shows a similar value, around 337 in both cases. This result may seem counterintuitive, but it is explained by considering that the standard deviation, as a global metric, is not sensitive to local variations or structured noise. Therefore, visible artifacts such as white line artifacts, which are linear bright bands caused by detector gaps, have a marginal impact on the overall value of the standard deviation. These will be discussed in more detail in the Subsection 5.2.3. In conclusion, although the metric does not show variations, reconstruction with shorter frame length are visually worse due to the appearance of artifacts.

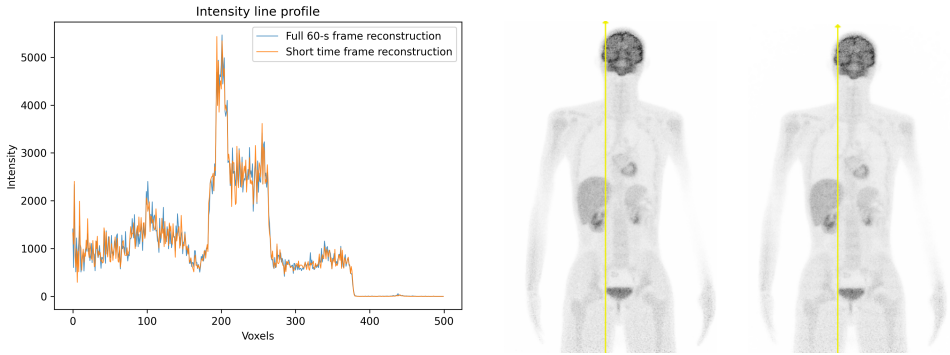

(A) (B) (C)

Figure 5.5: Line profile along the coronal plane of all reconstructions without respiratory and cardiac motion. (A) is the line profile along coronal plane, (B) is the full 60-s reconstruction, and (C) is the short-time frame reconstruction.

5.2.3 Impact of Frame Length

The effect of motion correction depends mainly on the choice of the duration of the stride between consecutive frames. It is expected that, by choosing a shorter time frame, the effect of motion correction is more effective, since it is possible to have a better estimate of the motion. However, shorter strides result in noisier frames due to the reduced counts per frame, leading to less reliable motion estimation and degradation of image quality. As demonstrated in Subsection 5.2.2, the summation of noisy frames can reduce the image quality: the shorter the frames, the noisier the individual frames are, and thus the lower the final image quality after summation. Figure 5.6 shows two reconstructions: part A has a frame length of 0.3125 s, part B a frame length of 0.9375 s. Although with 0.3125 s it is easier to follow the path and estimate and correct the motion, white line artifacts appear due to the gaps between

the detectors (see Figure 4.1), which cause non-uniform noise. These artifacts become more noticeable with shorter strides because the noise has a greater impact.

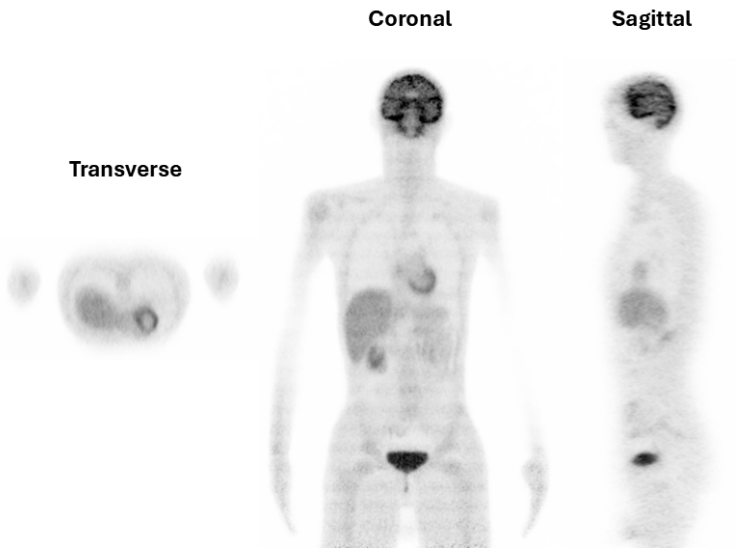

(A) 0.3125-s frame reconstruction

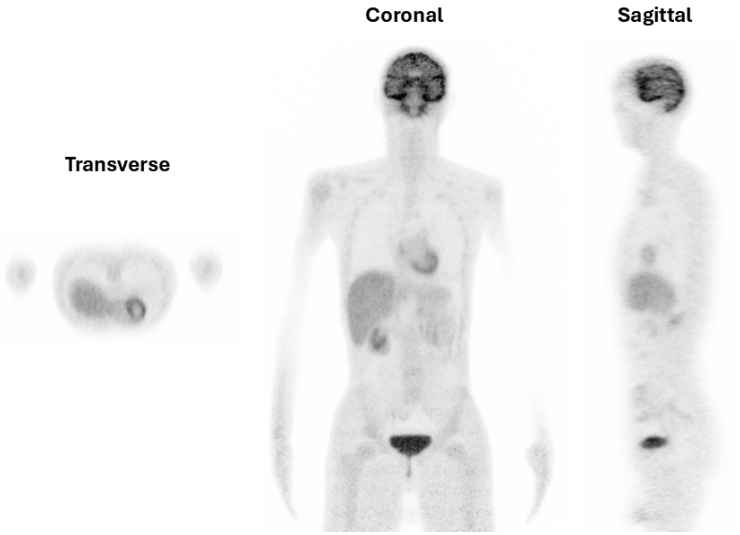

(B) 0.9375-s frame reconstruction

Figure 5.6: Impact of frame length. (A) is the 0.3125-s frame reconstruction after motion correction. (B) is the 0.9375-s frame reconstruction after motion correction.

To reduce this artifact, it is possible to apply a median filter to all the frames of the reconstruction before adding them. By replacing the value of each voxel with the median of the values present in its surroundings, the filter effectively removes white line artifacts from the images. Although the median filter is particularly effective for impulsive noise, it also proves to be useful in reducing localized noise, such as in areas with fewer detected events, such as those affected by gaps between detectors [60]. The result is shown in Figure 5.7. However, the artifacts in the lower part of the body persist.

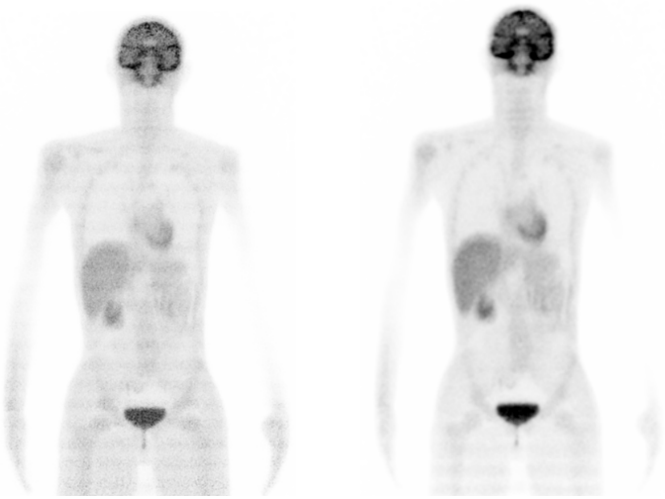

(a) 0.3125-s frame reconstruction without filtering

(b) 0.3125-s frame reconstruction with median filtering

Figure 5.7: Impact of median filtering. (a) is the 0.3125-s frame reconstruction. (b) is the 0.3125-s frame reconstruction. Both of them are referring to the simulation with motion that is not corrected.

From the comparison between the reconstruction with 0.9375 s frame duration and 0.3125 s frame duration after median filtering, the former is preferable because it is more computationally efficient: it requires less memory and less processing time, while still providing good results.

5.3 Simulation with lesions

PET imaging has become a cornerstone in several oncologic procedures such as tumor staging, treatment efficacy assessment during or after treatment and radiotherapy planning [61]. Therefore, it is essential to be able to correctly identify lesions within the body to avoid incorrectly classifying healthy and pathological tissues, compromising diagnosis and treatment. In order to validate motion correction for the WT-PET scanners, several PET data acquisitions were simulated in the presence of four lesions: two in the liver and two in the right lung. The data were simulated for three different types of phantoms: low BMI phantom, medium BMI phantom, and high BMI phantom. These labels are used throughout this work for clarity, although the corresponding phantom IDs in the XCAT software (from which they were derived) are different.

5.3.1 Low BMI phantom

The first phantom is identified by the number 71; its BMI is 18.64.

5.3.1.1 Impact of Motion

Adding lesions leads to a greater awareness of cardiac and respiratory motion that compromises the images. Figure 5.8 shows the difference between two simulations obtained in different conditions: without respiratory and cardiac motion (A) and with respiratory motion (B). Both acquisitions were obtained in 60 seconds and reconstructed with a full 60 s reconstruction. It is clear from the comparison that the lesions in the second case appear larger. Instead of well-defined, circular, and small lesions as in part A of Figure 5.8, in part B all lesions are blurred. In particular, there is a large difference between liver and lung lesions, which is also reflected in the evaluation of lesion detectability. Although the tumor-to-background concentration is 8:1, lung lesions are more difficult to detect. This is mainly due to the overall lower background activity in the lungs compared to the liver, which reduces the absolute activity of the lesions and makes them less distinguishable. In addition, respiratory and cardiac motion worsen detectability by causing partial overlap and blurring between the lower lung lesion and the upper part of the liver. To further highlight this effect, an additional sagittal view has been added showing the lung lesions. From the second sagittal view in part B, it is clearly evident that the lung lesions are almost invisible and difficult to detect, especially the lesion near the liver.

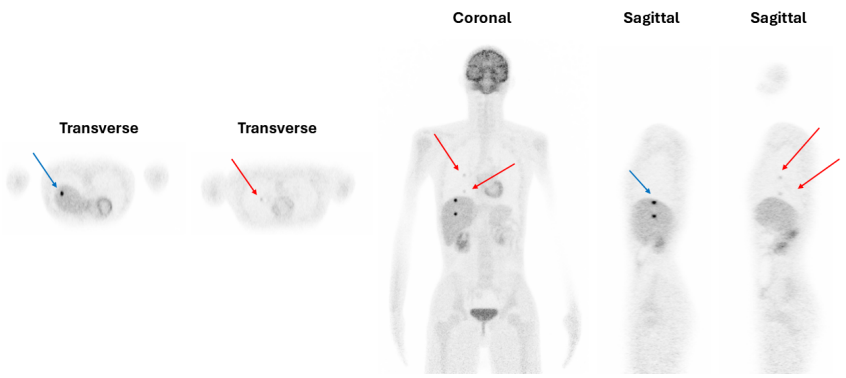

(A) Full 60-s reconstruction without motion

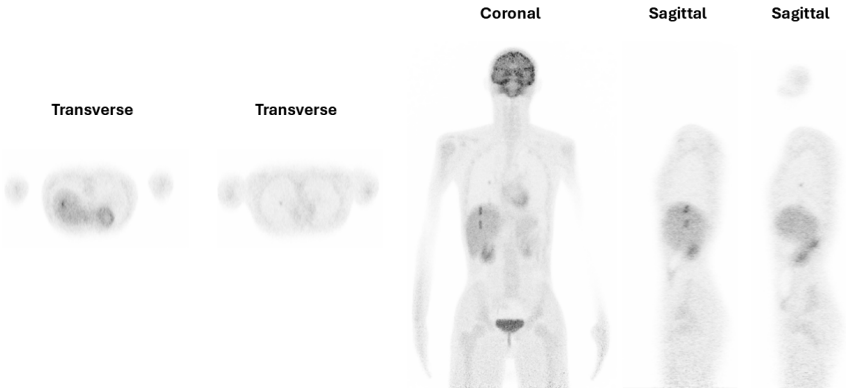

(B) Full 60-s reconstruction with motion

Figure 5.8: Impact of motion. (A) is the full 60-s reconstruction without respiratory motion. (B) is the full 60-s reconstruction with motion artifacts but uncorrected. Two sagittal and transverse planes are shown to visualize both two lesions in the liver and in the lung. In (A), the lesions are identified by arrows.

5.3.1.2 Impact of Motion Correction

Figure 5.9 shows how motion correction is effective in compensating for motion artifacts. The lesions appear smaller and less blurry, demonstrating how motion compensation has benefited their visualization. The effect in the liver is certainly more easily visible than in the lungs, where visualization is compromised by the low background activity of the lung itself. While part A shows a full 60-s reconstruction with motion but uncorrected, part B shows a 0.9375-s frame reconstruction with motion and motion correction.

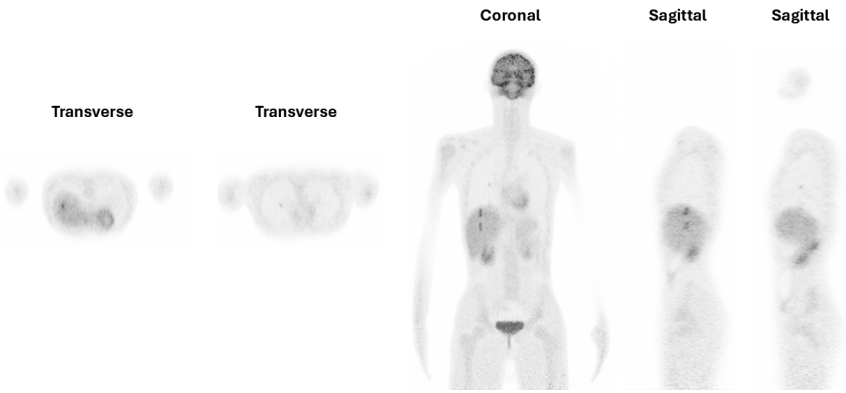

(A) Full 60-s reconstruction with motion

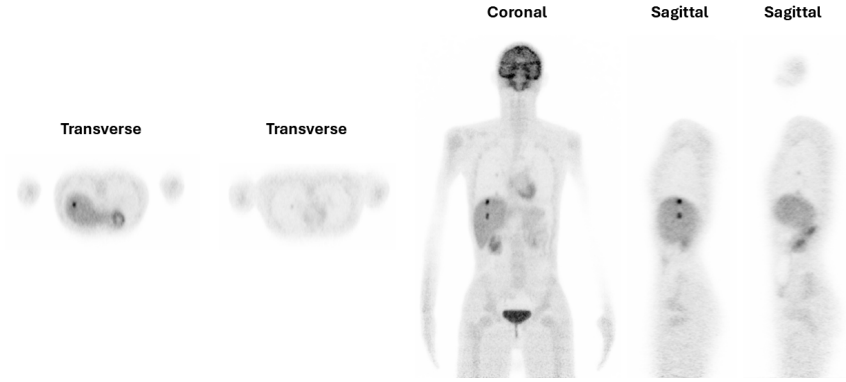

(B) Short-time frame reconstruction after motion correction

Figure 5.9: Impact of motion correction. (A) is the full 60-s reconstruction with motion artifacts but uncorrected. (B) is 0.9375-s frame reconstruction after motion correction. Two sagittal and transverse planes are shown to visualize lesions in both the liver and the lung.

5.3.1.3 Impact of Frame Length

As in Subsection 5.2.3, two different frame lengths are tested to show which of the two is more effective. It had been demonstrated in the simulations without lesions that the reconstruction with a stride equal to 0.9375 s was better both in terms of computational cost and better quality. The reconstruction with a stride of 0.3125 s, although better at following the path of the movement, was compromised by artifacts; therefore, it was discarded. Therefore, starting from the assumption that 0.9375 s offers a good result, a new condition that is a compromise between the two previous ones is tested. This is a reconstruction that has a frame length of 0.9375 s and a stride of 0.3125 s between successive frames. The result is that 0.625 s are shared between two consecutive frames. This reconstruction will henceforth be referred to as 'overlapping reconstruction'. Figure 5.10 shows in part A the 0.9375-s frame reconstruction, in part B the overlapping reconstruction. The quality of the two images is quite similar. With the overlap, it is possible to obtain more identifiable and more defined lesions compared to the 0.9375-s reconstruction. However, it is noticeable that the white line artifacts begin to appear, suggesting that the 0.3125-s

stride amplifies the noise but follows the movement better.

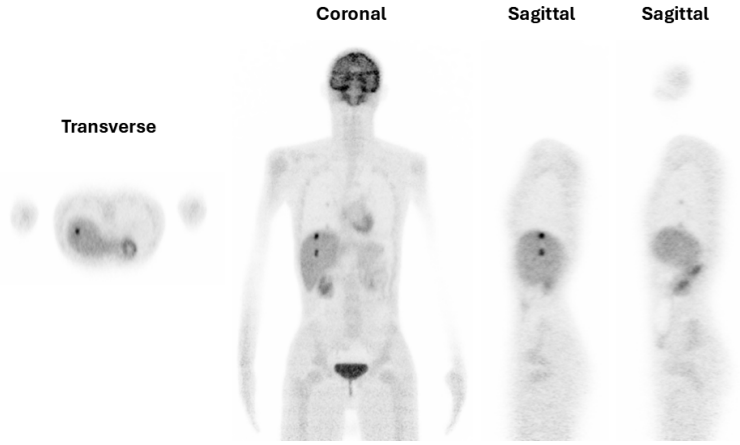

(A) 0.9375-s frame reconstruction

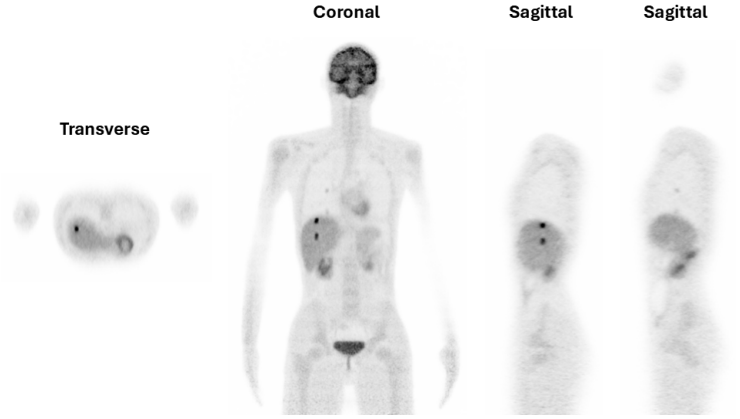

(B) Overlapping reconstruction

Figure 5.10: Impact of frame length. (A) is 0.9375-s frame reconstruction. (B) is the overlapping reconstruction. Both are after motion correction. Two sagittal planes are shown to visualize both two lesions in the liver and in the lung.

5.3.1.4 Impact of Deblurring

The goal of deblurring is to improve the quality of PET images obtained after motion correction. Different methods exist to perform deblurring, divided into non-blind deconvolution and blind deconvolution. The former are based on a known Point Spread Function (PSF); the latter on an unknown PSF. In this work, Richardson-Lucy Deconvolution, a type of non-blind deconvolution, has been implemented. The advantages of this technique are the ease of implementation and the ability to recover fine details, resulting particularly useful in the identification of lesions. The principle behind deblurring is the following: the blur profile (the PSF) that has degraded the image is known, and this information is used to attempt to reconstruct the original image through an iterative deconvolution process. The PSF has been modeled as a three-dimensional Gaussian filter with anisotropic sigma values of (1.5, 2.5, 1.5) voxels, corresponding to a FWHM of approximately (7.1 mm, 11.8 mm, 7.1 mm) along the x, y, and z directions respectively. This kernel is applied across the entire

PET volume after motion correction. Both the image and the PSF were normalized to avoid numerical distortions and ensure stability in the process. The Lucy-Richardson algorithm is iterative: higher number of iterations highlights the details better, but risks amplifying the noise [62].

Deblurring was applied to both reconstructions analyzed in the previous Subsection 5.3.1.3. Figure 5.11 shows three cases of deconvolution compared to the overlapping reconstruction: in part A, the number of iterations is 5; in part B, it is 10; and in part C, it is 30. The second and third show less blurred and more defined lesions but there is a dotting effect: the image loses quality overall. The image of part A presents a better compromise between sharpness and noise. This comparison highlights the importance of a calibrated choice of the number of iterations depending on the type of detail to highlight and the noise tolerance. In this study, a number of iterations equal to 5 is chosen.

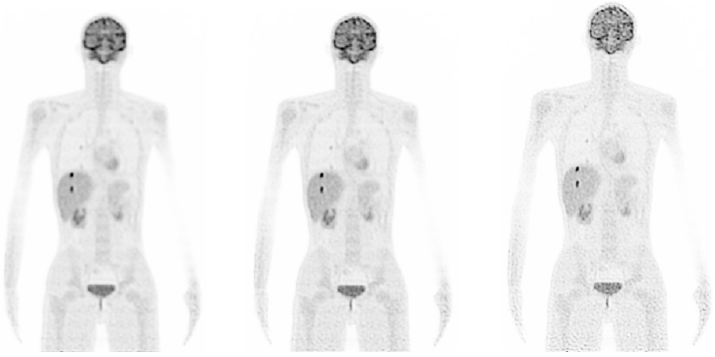

(a) 5 iterations **(b)** 10 iterations **(c)** 30 iterations

Figure 5.11: Impact of the number of iterations. All the reconstructions are the overlapping reconstructions after motion correction. (a) is obtained after 5 iterations, (b) after 10 iterations, and (c) after 30 iterations.

Figure 5.12 shows the difference between the PET image after motion correction (A) and the PET image corrected and deblurred with 5 iterations (B). It is now possible to compare the effect of deblurring with respect to the initial image. Deblurring allows to obtain an image in which the lesions and organs are defined and clearer.

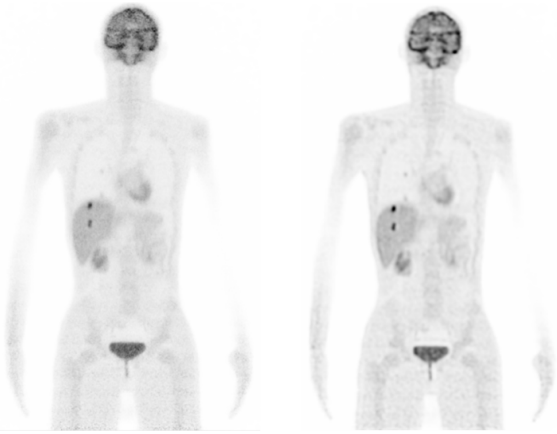

(a) 0.9375-s reconstruction without deblurring

(b) 0.9375-s reconstruction with deblurring after 5 iterations

Figure 5.12: Impact of deblurring. Both reconstruction are after motion correction.

5.3.1.5 Lesion Analysis

After comparing the reconstructions of the low BMI phantom simulations under different conditions, a quantitative analysis of the detectability of the four lesions was conducted. Through motion correction and deblurring, it was possible to visually evaluate the effectiveness of the two techniques, resulting in a better definition of the contours and in reduced dimensions. The next step is to quantify the four thoracic lesions using the analyses described in Chapter 4. For each lesion, eight different reconstruction conditions were considered:

- Full 60-s reconstruction without motion artifacts
- Full 60-s reconstruction with motion artifacts
- 0.9375-s frame reconstruction without motion correction
- 0.9375-s frame reconstruction with motion correction
- 0.9375-s frame reconstruction with motion correction and deblurring
- Overlapping reconstruction without motion correction
- Overlapping reconstruction with motion correction
- Overlapping reconstruction with motion correction and deblurring

Quantification by detectability metrics must first be preceded by lesion segmentation using the region growing algorithm. Starting from the ROI of the selected lesion in AMIDE, the maximum value was calculated and a specific percentage threshold was applied for each condition. This procedure was repeated to obtain the lesion masks for all reconstructions on the filtered images. The threshold values and the corresponding intensity maxima for the two liver lesions are reported in Appendix

B. For lung lesions, additional spatial information regarding the insertion of the lesion in the phantom was used to facilitate the identification of the seed point, while the threshold was equal to 40% for all reconstructions. The segmented images obtained with the region growing algorithm are reported in Figures 5.13 and 5.14. Once the lesion masks were obtained, the CRC, CNR and lesion volume metrics were calculated. For this purpose, the mean and standard deviation of the background were calculated on the original (unfiltered) images of each reconstruction on the basis of the ROIs in the free-lesion regions. ROIs were defined as spheres with equal dimensions of 15 mm along each axis. The results are shown in Tables 5.1 and 5.2, for the liver and lung, respectively. The mean and standard deviation presented in the tables could be misleading because they show very different values. This is because some reconstructions are based on averaging frames, while others consider the sum of all voxels. Therefore, the coefficient of variation (CV), defined as the ratio of the standard deviation to the mean, was calculated to provide a normalized measure of variability. To improve table readability, the following abbreviations are used throughout this chapter:

- **MA** = motion artifacts ("no MA" indicates that no motion was included in the simulation; "+ MA" indicates that motion artifacts were present, but no correction was applied).
- **MC** = motion correction (applied in cases labeled "+ MC").
- **DB** = deblurring (applied in cases labeled "+ DB").

The final step consists of computing the metrics on the unfiltered images in order to faithfully represent the real reconstructive conditions. The metrics for lesions of low BMI phantom are presented in Tables 5.3, 5.4 and 5.5 for CNR, CRC, respectively.

Background ROIs Analysis

Table 5.1: Mean, standard deviation (SD) and coefficient of variation (CV) of liver background ROIs — low BMI phantom

Reconstruction Type	**SD**	**Mean**	**CV**
Full 60-s (no MA)	369.77	2789.36	0.132
Full 60-s + MA	323.04	2748.84	0.118
0.9375-s + MA	5.16	42.99	0.120
0.9375-s + MC	3.15	43.60	0.072
0.9375-s + MC + DB	0.01	0.22	0.045
Overlap + MA	5.40	43.63	0.124
Overlap + MC	2.84	44.34	0.064
Overlap + MC + DB	0.01	0.23	0.060

Table 5.2: Mean, standard deviation (SD) and coefficient of variation (CV) of lung background ROIs — low BMI phantom

Reconstruction Type	**SD**	**Mean**	**CV**
Full 60-s (no MA)	84.10	630.70	0.133
Full 60-s + MA	92.81	642.90	0.144
0.9375-s + MA	1.93	10.76	0.179
0.9375-s + MC	0.92	10.88	0.085
0.9375-s + MC + DB	0.00	0.05	0.060
Overlap + MA	1.73	11.03	0.157
Overlap + MC	1.01	10.72	0.094
Overlap + MC + DB	0.00	0.05	0.080

Segmented lesion masks: Lung

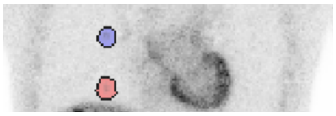

(a) Full 60-s (no MA)

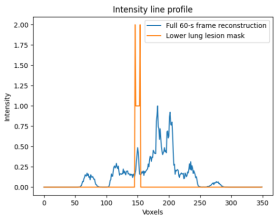

(b) Lower lesion profile

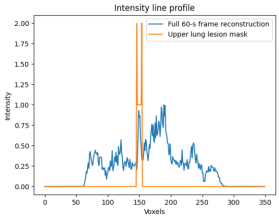

(c) Upper lesion profile

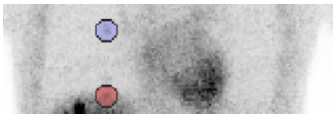

(d) 0.9375-s + MA

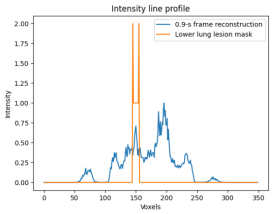

(e) Lower lesion profile

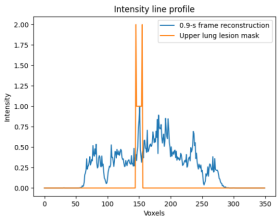

(f) Upper lesion profile

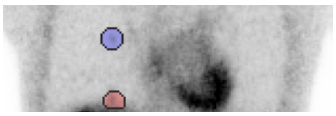

(g) 0.9375-s + MC

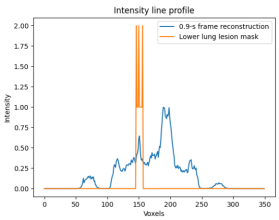

(h) Lower lesion profile

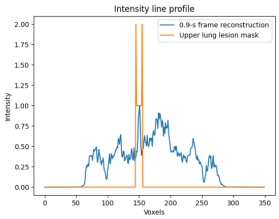

(i) Upper lesion profile

(j) Overlapping + MC + DB

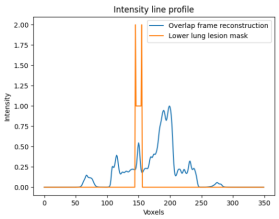

(k) Lower lesion profile

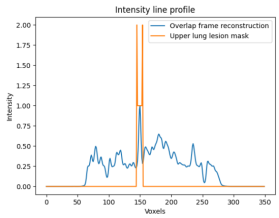

(l) Upper lesion profile

Figure 5.13: Masks of lung lesions in four reconstruction conditions. The top lesion is blue, the bottom lesion is red. For each mask on the left column, there are the corresponding intensity line profiles for the lower (middle) and upper (right) lesions.

Segmented lesion masks: Liver

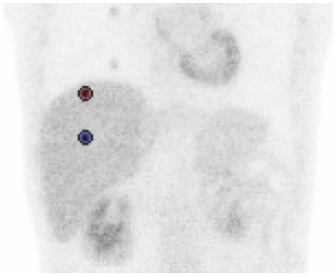

(a) Full 60-s (no MA)

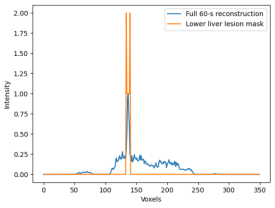

(b) Lower lesion profile

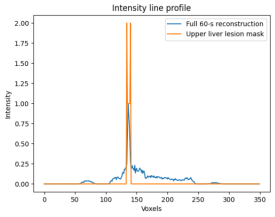

(c) Upper lesion profile

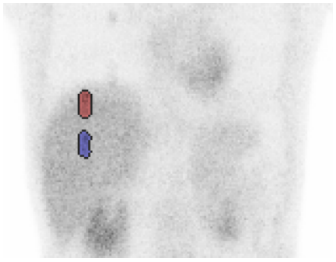

(d) 0.9375-s + MA

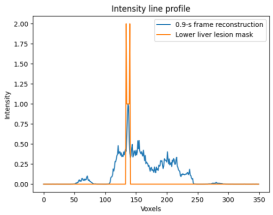

(e) Lower lesion profile

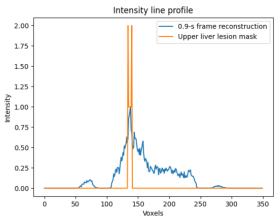

(f) Upper lesion profile

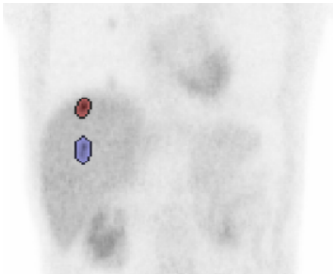

(g) 0.9375-s + MC

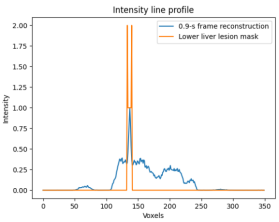

(h) Lower lesion profile

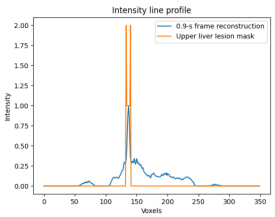

(i) Upper lesion profile

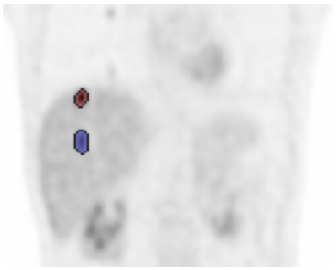

(j) Overlapping + MC + DB

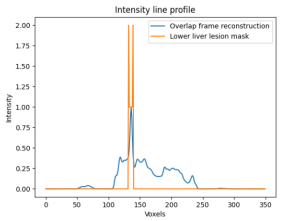

(k) Lower lesion profile

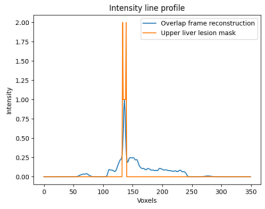

(l) Upper lesion profile

Figure 5.14: Masks of liver lesions in four reconstruction conditions. The bottom lesion is blue, the top lesion is red. For each mask on the left column, there are the corresponding intensity line profiles for the lower (middle) and upper (right) lesions.

Detectability Metrics

Table 5.3: CNR – Liver and Lung Lesions for low BMI phantom

Reconstruction	Liver bottom	Liver top	Lung bottom*	Lung top
Full 60-s (no MA)	14.67	17.92	4.88	5.87
Full 60-s + MA	4.17	5.57	5.83	4.29
0.9375-s + MA	4.73	5.60	8.11	2.43
0.9375-s + MC	6.34	14.59	12.13	5.00
0.9375-s + MC + DB	19.27	37.18	18.64	14.84
Overlap + MA	3.50	5.42	8.77	2.90
Overlap + MC	6.84	16.27	11.07	5.36
Overlap + MC + DB	13.47	28.09	11.42	12.94

**Values for the bottom lung lesion are considered unreliable due to segmentation errors that caused the region-growing algorithm to expand into the liver.*

Table 5.4: CRC – Liver and Lung Lesions for low BMI phantom

Reconstruction	Liver bottom	Liver top	Lung bottom*	Lung top
Full 60-s (no MA)	0.28	0.34	0.09	0.11
Full 60-s + MA	0.07	0.09	0.12	0.09
0.9375-s + MA	0.08	0.10	0.21	0.06
0.9375-s + MC	0.07	0.15	0.15	0.06
0.9375-s + MC + DB	0.13	0.25	0.16	0.13
Overlap + MA	0.06	0.10	0.20	0.07
Overlap + MC	0.06	0.15	0.15	0.07
Overlap + MC + DB	0.12	0.26	0.12	0.14

**Values for the bottom lung lesion are considered unreliable due to segmentation errors that caused the region-growing algorithm to expand into the liver.*

Table 5.5: Volume (mm^3) – Liver and Lung Lesions for low BMI phantom

Reconstruction	Liver bottom	Liver top	Lung bottom*	Lung top
Full 60-s (no MA)	656.00	600.00	3504.00	2808.00
Full 60-s + MA	3336.00	3160.00	2632.00	3704.00
0.9375-s + MA	3128.00	3320.00	3824.00	3880.00
0.9375-s + MC	5016.00	2072.00	3440.00	3880.00
0.9375-s + MC + DB	2616.00	1312.00	3744.00	2872.00
Overlap + MA	4808.00	3096.00	3600.00	3824.00
Overlap + MC	4992.00	2120.00	3264.00	3760.00
Overlap + MC + DB	2656.00	1304.00	3832.00	2568.00
Ground-truth	523.60	523.60	523.60	523.60

**Values for the bottom lung lesion are considered unreliable due to segmentation errors that caused the region-growing algorithm to expand into the liver.*

Discussion

The segmented images obtained with the region growing algorithm are reported in Figures 5.13 and 5.14. Each figure illustrates the effect of the different reconstruction conditions on the appearance and size of the lesions. The images highlight how motion correction and deblurring progressively improve the delineation of lesion borders, making their identification clearer and easier to interpret. Figure 5.13 shows the bottom and top lung lesions in five reconstruction conditions: (i) full 60-s without motion artifacts, (ii) 0.9375-s without motion correction, (iii) 0.9375-s with motion correction, and (iv) overlapping with motion correction and deblurring. These reconstructions summarize the analyzed cases, presenting both the target image and the intermediate steps required to achieve a better result. Although deblurring improves segmentation, the visual detectability slightly changes. Moreover, the lower lesion shows an unreliable shape. Figure 5.14 shows the two liver lesions under the same reconstruction conditions.

The metrics confirm that reconstructions affected by motion artifacts (both full 60-s and short-time frame reconstructions) present significantly underestimated values of CNR and CRC, as well as overestimated volumes compared to the ideal 60-s without motion artifacts. Motion correction modestly improves the values obtained, while deblurring provides an even greater gain. Regarding the lower liver lesion, the CNR increases from 4.73 (in the uncorrected 0.9375-s frame reconstruction) to 6.34 after motion correction, reaching 19.27 after deblurring, exceeding even the ideal motion-free reconstruction (14.67). The same trend is observed for the CRC. Although the value increases from 0.08 of the motion corrected image to 0.13 of the deblurred image, it remains below the reference value (0.28), suggesting that the tumor-to-background ratio is actually impossible to recover. This outcome is expected and is explained by the partial-volume effect, in which part of true lesion activity blurs into the surrounding tissue due to the limited spatial resolution. This effect is particularly evident in small lesions, leading to an underestimation of the

activity ratio and a larger reconstructed lesion volume than the ground truth. In terms of volume, improvements are observed across reconstructions. The segmented volume decreases from 3128.00 mm^3 (0.9375-s frame reconstruction) to 2616.00 mm^3 (0.9375-s frame after motion correction and deblurring), suggesting a greater accuracy in the definition of the borders. However, the ideal value of the inserted lesion is about 523.60, suggesting that a large portion of the voxels in healthy tissue are misclassified as pathological. The deblurring step also contributes to reducing the segmented lesion volume, further improving boundary accuracy. The top liver lesion shows an even better trend, with higher CNR and CRC values and lower segmented volumes. For example, after deblurring, the CNR reaches 37.18, while the CRC 0.25 (versus 0.34 in the ideal reconstruction). Volume decreases from 3000 mm^3 to 1312 mm^3, about three times the ground truth but clearly improved. These results state that combining motion correction with deblurring not only improves visibility but also partially restores contrast and reduces the segmented region, better approximating the true lesion size.

Lung lesions present additional challenges. The background activity of the lung is lower than that of the liver, resulting in fewer detected events in the lesion and in the surrounding tissue. This leads to increased image noise, making it more difficult to distinguish lesions from the surrounding tissue. This is evident both visually and in the metrics. In particular, the lower lesion was excluded from the quantitative analysis because the seed point (chosen as the voxel of maximum intensity inside the ROI defined in AMIDE) was likely still within the lesion, but the region-growing algorithm expanded preferentially into the liver, whose higher uptake values attracted the growth. Even greatly reducing the size of the ROI, chosen in AMIDE on which the choice of the seed point is based, does not change the results. In addition, even looking at the initial image, it is not possible to locate it at all. Therefore, the results for the lower lesion should be considered unreliable. By contrast, the region growing algorithm is able to identify the upper lesion correctly. CNR increases from 2.43 (uncorrected) to 14.84 after deblurring. CRC is also recovered up to a value of 0.13 after deblurring, higher than the ideal 60-s reconstruction (0.11), highlighting the potential of deblurring to improve contrast recovery even in the presence of dynamic acquisitions and with short frames. In general, reconstructions affected by motion artifacts tend to overestimate lesion volumes and underestimate contrast metrics. Motion correction yields a moderate improvement, but deblurring produces the most significant results. Although, as discussed in Subsection 5.3.1.3, the overlapping reconstruction offer better visual identification of lesions, the quantitative metrics did not show significant improvements compared to the 0.9375-s reconstruction. Nevertheless, since the overlapping reconstruction better follows both cardiac and respiratory motion, thanks to a stride of 0.3125 s, it is considered a preferable choice. In all conditions, images post-processed with both techniques show significantly higher CNR and CRC, both for liver and lung lesions. These findings confirm that the proposed processing pipeline represents an effective strategy to enhance the diagnostic quality of PET images in physiological motion conditions. The impact is

particularly strong for liver lesions in terms of volume and contrast recovery, while for lung lesions, the main benefit is improved CNR. The results obtained for this phantom suggest that the WT-PET system, supported by adequate correction and post-processing algorithms, can allow accurate detection even under realistic and dynamic acquisition conditions.

5.3.2 Medium BMI phantom

The second phantom is identified by the number 164; its BMI is 28.22.

5.3.2.1 Impact of Motion Correction

The same procedures validated for low BMI phantom were also applied to the subsequent phantoms, medium and high BMI phantoms. In particular, having already found the reconstruction that performed best (overlapping reconstruction), it was selected for testing on these other simulations to see its effectiveness in different circumstances. Medium BMI phantom, as well as the high BMI phantom, present differences in terms of BMI compared to the first phantom analyzed. Specifically, they present higher BMI, which translates into lower image quality. The lesions appear more compressed and less defined. The comparison shown in Figure 5.15 illustrates the full 60-s reconstruction with motion artifacts but without correction (A) and the overlapping reconstruction with motion correction (B). It is immediately noticeable that, in the first image, the lesions are less defined and smoother; the overall image has a very poor resolution, mainly due to the acquisition of the simulated data. As BMI increases, image quality decreases due to a greater photon absorption, leading to a lower number of detected events. This effect is particularly noticeable in short-time frame reconstruction, where data is already limited. As a result, white line artifacts become more pronounced due to the combined effect of attenuation and increased noise. Part B, on the other hand, shows the effectiveness of motion correction in visualizing lesions, especially in the liver. The second lesion in the lung, located near the liver, does not show an improvement in the second case either.

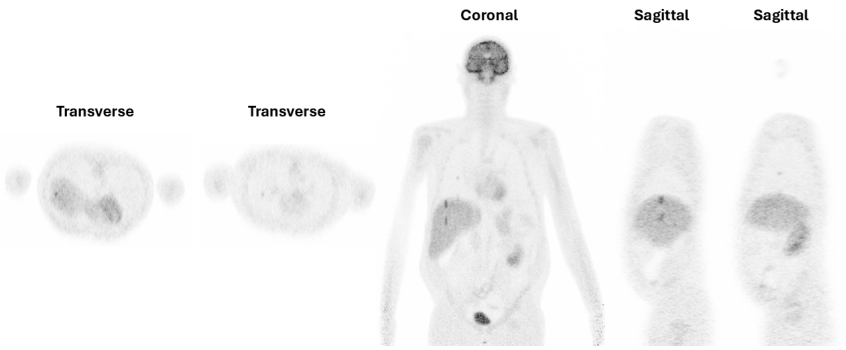

(A) Full 60-s reconstruction with motion

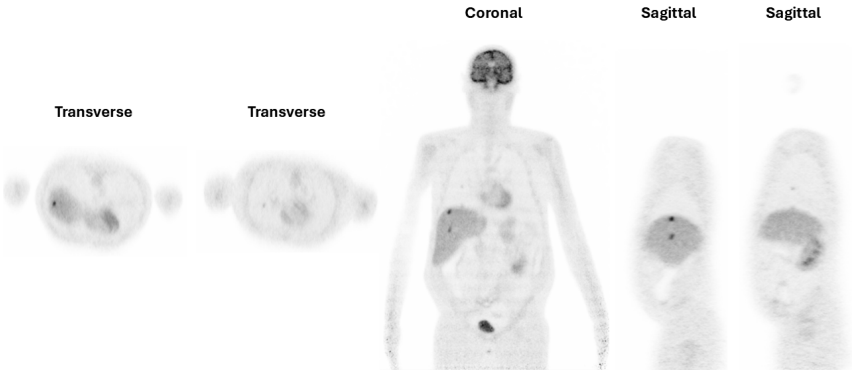

(B) Short-time frame reconstruction after motion correction

Figure 5.15: Impact of motion correction. (A) is the full 60-s reconstruction with motion artifacts but uncorrected. (B) is the overlapping reconstruction after motion correction.

5.3.2.2 Lesion Analysis

The calculation of detectability metrics is implemented in the same way as for the first phantom. A median filter is applied to the images obtained from the various reconstructions, ROIs are identified on it, and their maximum value is calculated. Based on the type of reconstruction, a different threshold is chosen to apply to the maximum value to find the seed point from which the region growing algorithm starts. Once the mask has been found, it is superimposed on the unfiltered image and the metrics are calculated. In this case, a reduced set of reconstruction is considered:

- Full 60-s reconstruction with motion artifacts
- Overlapping reconstruction without motion correction
- Overlapping reconstruction with motion correction

The 0.9375-s reconstruction is not performed, since visually the overlapping reconstruction provides better image quality. The reference image is the same as in the previous analysis. Although it refers to a different phantom, it is still useful to make a comparison to get an idea of how much the identification of the lesions improves or not. The threshold values and the corresponding intensity maxima are reported in

Appendix B. For lung lesions the threshold is 40% for each condition. The segmented lesion masks are shown in Figure 5.16 and Figure 5.17. The metrics were calculated as done for the low BMI phantom. The means, standard deviations, and CVs of the background are present in Tables 5.6 and 5.7, for the liver and lung, respectively. The metrics are reported in Tables 5.8, 5.9, and 5.10 for CNR, CRC and lesion volume, respectively.

Background ROIs Analysis

Table 5.6: Mean, standard deviation (SD) and coefficient of variation (CV) of liver background ROIs — medium BMI phantom

Reconstruction Type	SD	Mean	CV
Full 60-s (no MA)	369.77	2789.36	0.132
Full 60-s + MA	387.06	2664.67	0.145
Overlap + MA	6.84	40.11	0.170
Overlap + MC	2.83	40.46	0.070

Table 5.7: Mean, standard deviation (SD) and coefficient of variation (CV) of lung background ROIs — medium BMI phantom

Reconstruction Type	SD	Mean	CV
Full 60-s (no MA)	84.10	630.70	0.133
Full 60-s + MA	109.19	588.16	0.186
Overlap + MA	1.42	9.55	0.149
Overlap + MC	1.03	9.66	0.107

Segmented lesion masks: Lung

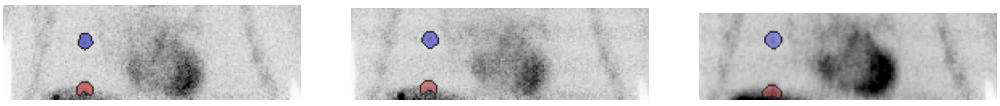

(a) Full 60-s + MA **(b)** Overlapping + MA **(c)** Overlapping + MC

Figure 5.16: Masks of lung lesions under three reconstruction conditions. Top lesion is blue, bottom lesion is red. Lesion segmentation is approximately the same in all conditions.

Segmented lesion masks: Liver

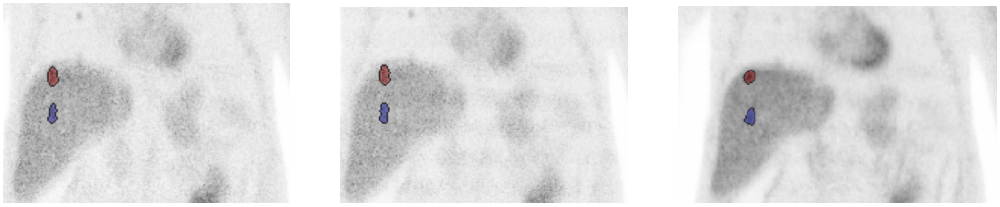

(a) Full 60-s + MA **(b)** Overlapping + MA **(c)** Overlapping + MC

Figure 5.17: Masks of liver lesions under three reconstruction conditions. Bottom lesion is blue, top lesion is red. Image quality and segmentation improve from (a) to (c).

Detectability Metrics

Table 5.8: CNR – Liver and Lung Lesions for medium BMI phantom

Reconstruction	Liver bottom	Liver top	Lung bottom*	Lung top
Full 60-s (no MA)	14.67	17.92	4.88	5.87
Full 60-s + MA	3.78	3.61	7.17	4.01
Overlap + MA	3.17	3.70	8.02	3.63
Overlap + MC	7.16	11.58	17.24	5.21

**Values for the bottom lung lesion are considered unreliable due to segmentation errors that caused the region-growing algorithm to expand into the liver.*

Table 5.9: CRC – Liver and Lung Lesions for medium BMI phantom

Reconstruction	Liver bottom	Liver top	Lung bottom*	Lung top
Full 60-s (no MA)	0.28	0.34	0.09	0.11
Full 60-s + MA	0.08	0.08	0.19	0.11
Overlap + MA	0.08	0.09	0.17	0.08
Overlap + MC	0.07	0.12	0.26	0.08

**Values for the bottom lung lesion are considered unreliable due to segmentation errors that caused the region-growing algorithm to expand into the liver.*

Table 5.10: Volume (mm^3) – Liver and Lung Lesions for medium BMI phantom

Reconstruction	Liver bottom	Liver top	Lung bottom*	Lung top
Full 60-s (no MA)	656.00	600.00	3504.00	2808.00
Full 60-s + MA	2320.00	4288.00	2984.00	3144.00
Overlap + MA	2600.00	3408.00	2776.00	3656.00
Overlap + MC	3320.00	3328.00	4160.00	3546.00
Ground-truth volume	523.60	523.60	523.60	523.60

**Values for the bottom lung lesion are considered unreliable due to segmentation errors that caused the region-growing algorithm to expand into the liver.*

Discussion

The segmented images of the lung and liver lesions obtained through the region growing algorithm are reported in Figure 5.16 and Figure 5.17, respectively. These highlight how motion correction improves the definition of the lesion borders, making their identification clearer. Figure 5.16 displays both upper and lower lung lesions in three reconstruction conditions: (i) full-60s with artifacts, (ii) overlapping without motion correction, and (iii) overlapping with motion correction. While segmentation improves with correction, visual identification does not change substantially. The second lung lesion, in particular, presents an unreliable shape. Figure 5.17 illustrates both lower and upper liver lesions in the same reconstruction conditions.

The results obtained once again show how the presence of motion artifacts significantly compromises the quality of PET images, negatively affecting the contrast metrics and the segmented volume of the lesions. Overall, it is clear from both the images presented and the metrics that the quality has worsened compared to the first phantom studied. The reason is mainly due to the adipose tissue present in the phantom, which causes a greater attenuation of photons in the body tissues. As a result, the images appear with greater noise.

In the liver, motion correction results in a noticeable CNR improvement for both lesions, though values remain below those achieved in the ideal reconstruction. For example, the lower liver lesion's CNR increases from 3.17 (uncorrected reconstruction) to 7.16 after motion correction, a value that is approximately half of that obtained under ideal condition (14.67). A similar pattern is observed for the upper liver lesion. There are no notable differences in values between the full 60-s reconstruction with motion artifacts and the uncorrected overlapping reconstruction, with value clustered around 3.17 and 3.78. The CRC shows only partial recovery, especially for the lower lesion, indicating that the tumor-to-background ratio cannot be fully recovered. Segmented volumes remain significantly overestimated, and in the case of the lower liver lesion, motion correction unexpectedly increases the volume. This behavior could be partially justified by the threshold used for the region growing algorithm. While in the cases without motion correction the threshold is set at 70% for the first lesion and 60% for the second lesion, for the motion corrected case the threshold decreases to 60% and 50%, respectively.

As for lung lesions, their identification is complex. For the upper lung lesion, motion correction improves the CNR from 3.63 to 5.21, approaching the reference value of 5.87. However, the CRC remains low and similar to uncorrected cases. Segmented volumes for lung lesions are substantially overestimated, with the reference reconstruction volume nearly four times the ground truth, suggesting that the region growing algorithm has included a large portion of healthy tissue as pathological. In general, the metrics obtained in the lungs are worse due to the low background activity, which hampers lesion-to-background discrimination. Lesions do not present values higher than the background, leading the region growing algorithm to include an increasingly larger part of the lung. By contrast, for the lower lesion the results seem to confirm a better trend. For example, the CNR in case of motion correction reaches a value of 17.24, even exceeding the ideal reconstruction (4.88). The CRC also shows a clear improvement (from 0.17 to 0.26), far higher than the ideal condition (0.09). This could suggest that for this lesion the workflow was very effective, offering better results even than the artifact-free image. However, visual analysis reveals that the segmentation mask is incorrectly located, shifted toward the liver. This misplacement explains why both CRC and CNR are higher: the liver has higher background activity, leading to greater region intensities, and thus greater contrast compared to the lung background.
In summary, motion-corrected reconstructions allow an improvement in the contrast metrics (CNR and CRC), even though the overestimation of the segmented volumes remains a significant issue. The results also suggest that the increase in BMI leads to a worse lesion segmentation, becoming a major limitation in validating this workflow for the general population. Generally, upper lesions show more reliable segmentation and metric improvement, while lower lesions, especially in the lungs, are more affected by noise and misclassification. The lower lung lesion, in particular, should be excluded from evaluation due to inconsistent and unreliable results.
Overall, the proposed pipeline represents a step forward in improving the diagnostic quality of PET images under physiological motion conditions, but it also highlights persisting limitations.

5.3.3 High BMI phantom

The last phantom analyzed is 184; its BMI is 37.96.

5.3.3.1 Impact of Motion Correction

Similarly to the medium BMI phantom, the high BMI phantom follows the same procedures: full 60-s reconstruction without motion correction and an overlapping reconstruction with motion correction. In this case, the BMI is even higher than the other two phantoms, resulting in an even more degraded image. The comparison in Figure 5.18 clearly shows how the ability to discern lung lesions from healthy tissue becomes significantly more difficult. Lesions appear compressed and poorly defined, almost blending into the background activity. Motion correction improves this

result, although the use of short-time frame reconstruction introduces slight artifacts. These artifacts, previously observed in 0.3125-s reconstruction, are caused by the gap between the detectors and are also present in the overlapping reconstruction. The visibility of these artifacts is exacerbated by the lower photon counts due to attenuation from the increased adipose tissue. A similar issue was observed in the medium BMI phantom, although to a lesser extent due to the more moderate increase in BMI compared to the phantom with low BMI. A greater improvement is seen in the lesion located at the top of the liver, with little improvement in the one at the bottom. As for lung lesions, these are almost imperceptible. The upper lesion is slightly more visible in the second sagittal view, while the lower one is indistinguishable from the liver. Motion correction does not improve their detectability.

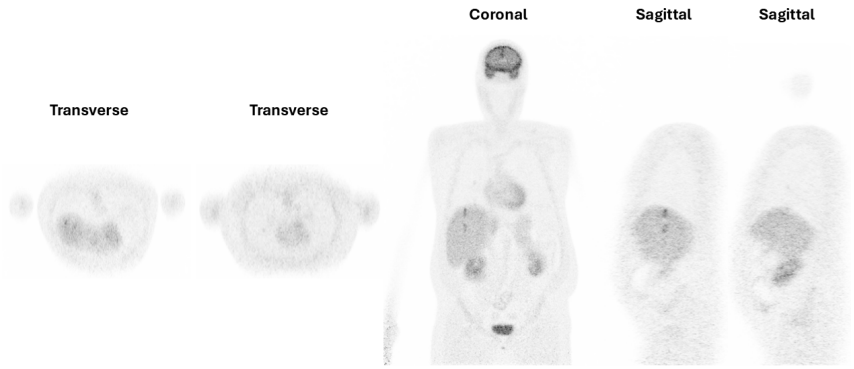

(A) Full 60-s reconstruction with motion

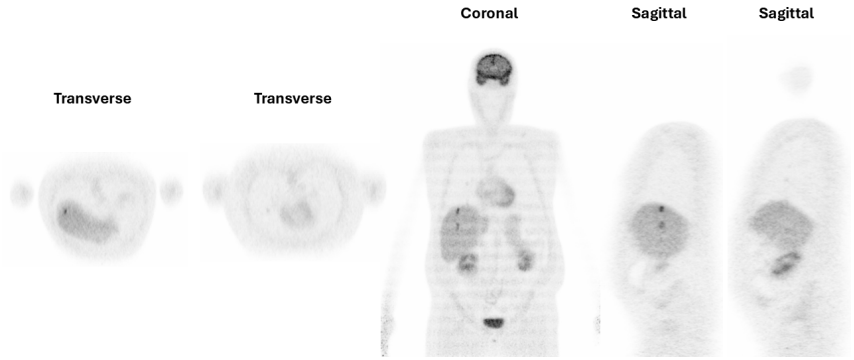

(B) Short-time frame reconstruction after motion correction

Figure 5.18: Impact of motion correction. (A) is the full 60-s reconstruction with motion artifacts but uncorrected. (B) is overlapping reconstruction after motion correction.

5.3.3.2 Lesion Analysis

The final simulation conducted for the validation of the motion correction workflow concerns the high BMI phantom. The processing steps are analogous to those applied to the first two phantoms. The reconstructions performed are:

- Full 60-s reconstruction with motion artifacts
- Overlapping reconstruction without motion correction

- Overlapping reconstruction with motion correction

The threshold values and corresponding maximum intensities used for the two liver lesions and the two lung lesions are reported in Appendix B. For lung lesions, the threshold is set at 40% for all conditions. The segmented images of the lung and liver lesions, obtained through the region growing algorithm, are reported respectively in Figure 5.19 and Figure 5.20, both referring to three reconstruction conditions: (i) full-60s with artifacts, (ii) overlapping without motion correction, and (iii) overlapping with motion correction. The means, standard deviations, and CVs of the background are presented in Tables 5.11 and 5.12, for the liver and lung, respectively. Tables 5.13, 5.14, and 5.15 report the metrics for liver and lung lesions, namely CNR, CRC, and lesion volume, respectively.

Background ROIs Analysis

Table 5.11: Mean, standard deviation (SD) and coefficient of variation (CV) of liver background ROIs — high BMI phantom

Reconstruction Type	SD	Mean	CV
Full 60-s (no MA)	369.77	2789.36	0.132
Full 60-s + MA	624.66	2348.18	0.266
Overlap + MA	7.21	39.30	0.183
Overlap + MC	4.18	39.22	0.107

Table 5.12: Mean, standard deviation (SD) and coefficient of variation (CV) of lung background ROIs — high BMI phantom

Reconstruction Type	SD	Mean	CV
Full 60-s (no MA)	84.10	630.70	0.133
Full 60-s + MA	127.30	572.16	0.222
Overlap + MA	1.60	9.44	0.169
Overlap + MC	1.16	9.85	0.118

Segmented lesion masks: Lung

(a) Full 60-s + MA **(b)** Overlapping + MA **(c)** Overlapping + MC

Figure 5.19: Masks of lung lesions under three reconstruction conditions. Top lesion is blue, bottom lesion is red. Lesion segmentation is approximately the same in all conditions.

Segmented lesion masks: Liver

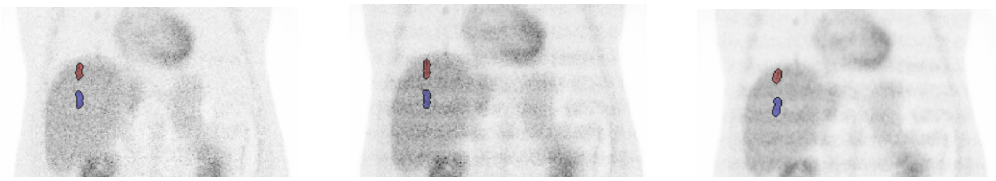

(a) Full 60-s + MA **(b)** Overlapping + MA **(c)** Overlapping + MC

Figure 5.20: Masks of liver lesions under three reconstruction conditions. Bottom lesion is blue, top lesion is red. Image quality and segmentation improve from (a) to (c).

Detectability Metrics

Table 5.13: CNR – Liver and Lung Lesions for high BMI phantom

Reconstruction	Liver bottom	Liver top	Lung bottom*	Lung top
Full 60-s (no MA)	14.67	17.92	4.88	5.87
Full 60-s + MA	2.28	3.53	2.33	2.12
Overlap + MA	2.69	3.80	2.87	2.50
Overlap + MC	4.21	7.53	5.90	3.19

**Values for the bottom lung lesion are considered unreliable due to segmentation errors that caused the region-growing algorithm to expand into the liver.*

Table 5.14: CRC – Liver and Lung Lesions for high BMI phantom

Reconstruction	Liver bottom	Liver top	Lung bottom*	Lung top
Full 60-s (no MA)	0.28	0.34	0.09	0.11
Full 60-s + MA	0.09	0.13	0.07	0.07
Overlap + MA	0.07	0.10	0.07	0.06
Overlap + MC	0.06	0.11	0.10	0.05

**Values for the bottom lung lesion are considered unreliable due to segmentation errors that caused the region-growing algorithm to expand into the liver.*

Table 5.15: Volume (mm^3) – Liver and Lung Lesions for high BMI phantom

Reconstruction	Liver bottom	Liver top	Lung bottom*	Lung top
Full 60-s (no MA)	656.00	600.00	3504.00	2808.00
Full 60-s + MA	2776.00	2080.00	2696.00	3792.00
Overlap + MA	2520.00	2360.00	2600.00	3880.00
Overlap + MC	3960.00	2656.00	5272.00	3880.00
Ground-truth volume	523.60	523.60	523.60	523.60

**Values for the bottom lung lesion are considered unreliable due to segmentation errors that caused the region-growing algorithm to expand into the liver.*

Discussion

The results obtained for this phantom confirm that motion artifacts considerably compromise PET image quality, affecting both visual detectability and quantitative metrics. Compared to the medium BMI phantom, a further degradation is observed, mainly due to the increased BMI, which causes stronger photon attenuation and more pronounced image noise. For the liver lesions, CNR values show an improving trend with motion correction, although they remain well below those of ideal reconstruction. For the bottom lesion, the CNR improves from 2.28 (uncorrected) to 4.21 after motion correction. Similarly, the top lesion improves from 3.53 to 7.53, remaining well below the ideal reconstruction (17.92). In terms of CRC, motion correction does not lead to improvements: CRC values slightly decrease or remain consistently low, indicating incomplete contrast recovery. Segmented volumes are again overestimated, with values exceeding both the ground truth and the reference reconstruction. Interestingly, in this phantom, motion correction results in larger volumes than the uncorrected reconstruction in all lesions. This overestimation is partly linked to lower threshold values in the region growing algorithm during motion correction, reflecting segmentation challenges caused by image degradation.
Regarding lung lesions, motion correction modestly improves the CNR of the upper lesion, almost approaching the ideal value, while the CRC slightly decreases. The lower lung lesion shows marked improvement, with CNR and CRC rising above ideal values. However, despite these promising metrics, visual inspection of the segmented masks reveals that the lesion was likely not correctly identified. The detected region appears displaced toward the liver, a zone of higher background activity, which explains the inflated values of both CRC and CNR. Therefore, this lesion must be considered unreliable for evaluation, as already observed in the previous simulations.
In summary, the motion correction workflow continues to show improvements in image contrast and lesion detectability, but it does not resolve all limitations. In particular, the results underscore that increased BMI negatively affects segmentation accuracy and lesion contrast, making the method less generalizable.

5.3.4 Cross-patient Summary and Effect of BMI

The three simulated phantoms showed different responses to motion artifacts and subsequent correction, influenced by the different BMI. In general, a consistent trend was observed in all three simulations: motion correction improved lesion detectability and image quality. CRC and CNR values increased compared to reconstructions without motion correction in both full 60-s and short-time frames. In the low BMI phantom, the metrics achieved good results in terms of higher CRC and CNR and lower volume. In contrast, for medium and high BMI phantoms, CRC and CNR improved, but lesion volumes were overestimated. This is a rather counterintuitive trend, partly justified by the lower threshold used for segmentation, partly due to reduced photon counts. In particular, the most marked worsening was observed in the high BMI phantom. This confirms that a high body mass index amplifies the

negative effects of motion, due to increased photon attenuation and more pronounced background noise. Furthermore, differences among the phantoms were not limited to BMI. Variations in height result in different lesion positions within the scanner's field of view. Given the non-uniform sensitivity profile of the scanner due to detector gaps, the same anatomical lesion may lie in an area of higher sensitivity in one phantom and in a region of lower sensitivity in another. This can lead to differences in lesion detectability and quantification, independently of BMI or motion-related effects.

Figure 5.21 provides a direct comparison between the metrics obtained after motion correction for the three BMI categories. CNR values show a decreasing trend from low to high BMI, with the upper liver lesion presenting the highest contrast in the low BMI phantom and drastically lower values in the high BMI case. The lung lesion consistently shows low CNR across all phantoms. CRC follows a similar trend: the low BMI phantom reaches the highest value for the liver top lesion, while the high BMI phantom reports the lowest. Liver bottom and lung top lesions show comparable CRC values across phantoms, reaching highest values for the medium BMI phantom. Volume trends also vary: while low BMI phantoms show smaller lesion volumes, medium and high BMI phantoms show overestimated volume, indicating worse segmentation. An exception is noted for the liver bottom lesion, where the low BMI phantom shows the largest volume.

In conclusion, the comparison between phantoms suggests that the motion correction pipeline is effective, but its robustness is limited by phantom-specific factors, such as BMI. The method shows excellent potential in subjects with low BMI, but requires further refinements to ensure reliable performance also in patients with larger body sizes.

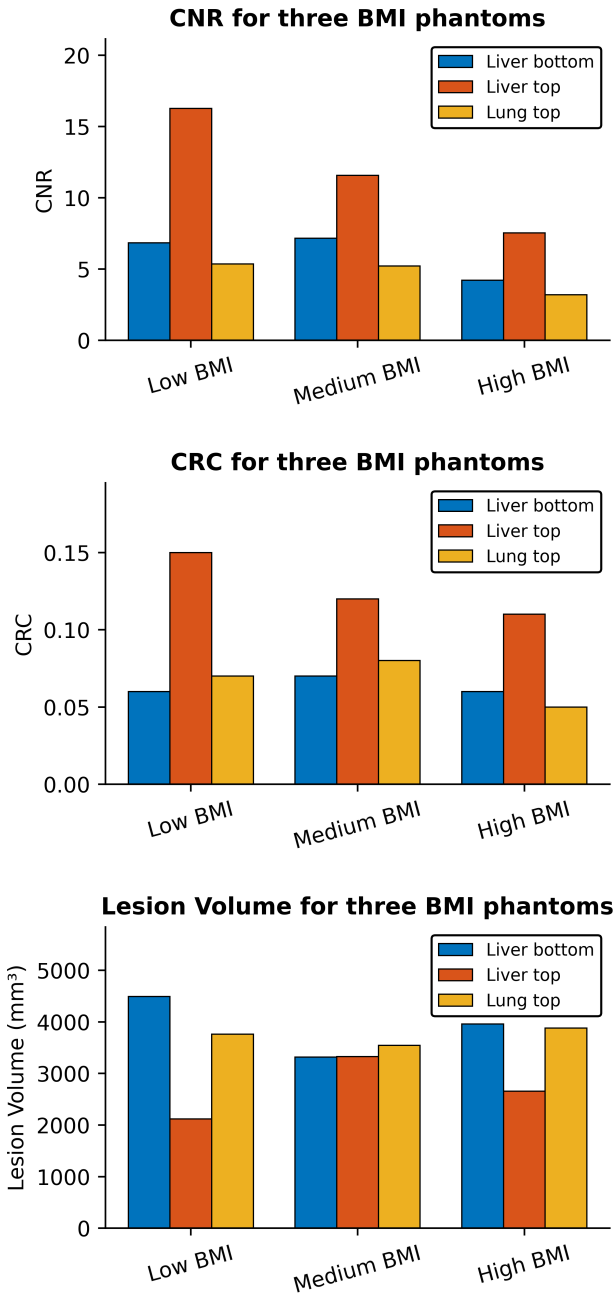

Figure 5.21: CNR, CRC and Lesion Volume for each lesion and for each phantom in reconstructions after motion correction. The lung bottom is discarded since its values are unreliable.

Chapter 6

Conclusions and Future Works

6.1 Summary of Findings

The aim of this work was to test an approach designed to mitigate motion artifacts caused by respiration and cardiac motion in the Walk-Through PET, a dual flat panel scanner, proposed by the MEDISIP Research Group at Ghent University. This novel device offers high throughput, simplified setup, reduced personnel workload, and higher spatial resolution compared to conventional cylindrical PET scanners. In the WT-PET, patients stand upright between two detector panels, which may lead to increased motion.

To address these artifacts, a method based on the reconstruction of short temporal frames was proposed, followed by motion correction obtained by superposing the frames with respect to the initial one (at time 0 s). The corrected frames were then averaged to produce a single image representing the FDG tracer distribution over the full acquisition duration.

Through several reconstructions, different from each other for the duration of the temporal frame, it was possible to identify the configuration yielding the best results. Although shorter frames (0.3125 s) better follow respiratory and cardiac motion, the quality of the resulting image is compromised by noise and the presence of artifacts due to the detector gaps. On the other hand, longer frames (0.9375 s) result in a reduced motion tracking accuracy. For these reasons, the optimal choice occurs with the overlapping reconstruction: each frame lasts 0.9375 s, with a step size of 0.3125 s between consecutive frames.

Several simulations were then analyzed on three phantoms with different BMI values. It was demonstrated that the application of the motion correction pipeline systematically improves image quality, both in visual and quantitative terms. CNR and CRC metrics showed an increase compared to conditions without motion correction. Similarly, a decrease in the volume of the lesions was observed with motion correction. This highlights how lesions are detected more accurately after motion correction.

However, as BMI increases, the post-correction improvements are not as significant. CNR and CRC still show higher values in the corrected images, but volumetric precision is reduced, with a tendency to overestimate the lesion volume. This behavior is

attributed to a greater photon attenuation through human tissues and to a higher background noise.

The results demonstrate the validity of the proposed model and represent a good starting point for developing future motion correction pipelines that are automatic and fast.

6.2 Future Perspectives

The proposed motion correction method represents a first step to compensate for cardiac and respiratory motion in WT-PET imaging. While it has been shown to be accurate and beneficial, there are several possible fields of development.

First, the proposed study evaluates the performance in three different phantoms, each with a different BMI. A subsequent step could be to test different phantoms to better understand the actual validity of the model and, subsequently, extend the application of the proposed workflow to real PET data, in order to verify its effectiveness in clinical settings and evaluate its robustness to inter-subject variability. A further possibility for improvement involves the application of motion correction fields, obtained from short reconstruction frames, to listmode data. This approach would allow to perform a single reconstruction using the corrected listmode data, thus eliminating the need to sum the single frames. Such a strategy could significantly reduce reconstruction times, preserving, or even improving, image quality and quantitative accuracy. This method was also proposed by Jin et al., as demonstrated in [63].
Deep learning-based methods for respiratory and cardiac motion correction have already been proposed in the literature. For example, the study by Lu et al., as demonstrated in [64], presents a comprehensive data-driven method for correcting respiratory motion (uRMC), employing deep learning neural networks, trained on extensive patient datasets, to obtain respiratory signals, create motion-corrected attenuation maps, and enhance the alignment of PET-CT images. The results indicated notable enhancements in diagnostic quality, implying that integrating deep learning approaches into our pipeline could provide a powerful direction for future research.

6.3 Societal Reflection

This thesis aims to address the issue of motion artifacts due to respiratory and cardiac motion in WT-PET. A key advantage of this novel design is the reduced total scan time, resulting in increased patient throughput. The simplified operation potentially increases access to high-quality diagnostic tests. In particular, such a system could be valuable in settings with limited resources, where traditional PET scanners may not be feasible due to cost, size, or staffing requirements.

Through motion correction, this work improves lesion visualization, leading to more accurate and early diagnoses. This has a direct impact on patient outcomes, since early detection frequently results in more efficient and less intrusive medical treatments.
The use of simulated data to validate motion correction techniques, while requiring high energy consumption and computational resources, reduces the need for expensive physical experiments and reduces the environmental impact related to the production of hardware components.
This research is in line with the United Nations Sustainable Development Goals (SDG), in particular health and innovation (SDG 3 and 9), demonstrating how technological advances can responsibly improve the quality and access to medical care, also considering social and environmental aspects [65].
In conclusion, this thesis contributes not only to the advancement of motion correction in PET imaging but also encourages a broader reflection on the role of innovation in promoting equitable and sustainable healthcare. Future implementation of WT-PET systems should continue to prioritize accessibility, ethical deployment, and environmental responsibility to ensure that the benefits of technological progress are widely and fairly distributed.

Appendix A

ANTs Registration Command and Parameters

The command used to perform the registration is shown below:

```
antsRegistration -d 3 \
    -r [$fixed_image, $moving_image, 1] \
    -t SyN[0.1,3,0.0] \
    -m mattes[$fixed_image, $moving_image, 1, 32] \
    -c [100x100x100x50x0,1e-6,5] \
    -s 2x1x0x0x0vox \
    -f 8x6x4x2x1 \
    -u 1 \
    -z 1 \
    -o [${output_prefix}, ${output_prefix}_Warped.nii.gz]
```

The main parameters used explained below:

1. `-d 3` – **Dimensionality**: sets the command to work with three-dimensional (3D) images.
2. `-r [fixed, moving, 1]` – **Initialization**: specifies how the moving image is initially positioned relative to the fixed image. Flag 1 enables automatic initialization via center of mass.
3. `-t SyN[0.1,3,0.0]` – **SyN Transformation**: the symmetric normalization is used for non-linear registration:
    - `0.1`: gradient step for updating the velocity field.
    - `3`: Gaussian smoothing on the velocity field to enforce regular deformations.
    - `0`: regularization applied to the velocity field.
4. `-m mattes[..., 1, 32]` – **Similarity Metric**: Mutual Information (Mattes) is used to compare the fixed and moving images:

- `1`: metric weight, ensuring that Mattes metric is fully applied as the primary method to assess image similarity.
- `32`: number of bins used for the histogram, allowing accurate computation of mutual information.

5. `-c [100x100x100x50x0,1e-6,5]` – **Multi-resolution Optimization Scheme**: specifies when the optimization would stop:
   - `100x100x100x50x0`: number of iterations per resolution level, starting from coarse to fine resolution.
   - `1e-6`: convergence tolerance, indicating the minimal improvement threshold.
   - `5`: number of consecutive evaluations required to reach convergence.
6. `-s 2x1x0x0x0vox` – **Smoothing**: applies decreasing Gaussian smoothing, in voxel units, at each level. Higher smoothing is applied at coarser resolution.
7. `-f 8x6x4x2x1` – **Progressive Downsampling**: reduces image resolution at initial levels to speed up computation.
8. `-u 1` – **Mask Usage**: enables the use of a binary mask to restrict the registration to a specific region of interest.
9. `-z 1` - **Intensity Normalization**: performs intensity normalization prior to registration.
10. `-o [...]` – **Output**: generates the registered image along with the forward and inverse deformation fields. [48]

Appendix B

Threshold Values and Intensity Maxima Used for Lesion Segmentation

B.1 Low BMI phantom

The threshold values and the corresponding intensity maxima for the two liver lesions are reported in Tables B.1 and B.2, while those for the lung lesions are shown in Tables B.3 and B.4. The differences in intensity values can be attributed to the nature of the reconstructions: in some cases, the images were obtained by averaging over multiple frames, resulting in lower intensity values, while the full 60-s reconstructions include all data acquired simultaneously, leading to higher maximum intensities.

Table B.1: Threshold for Bottom Liver Lesion — low BMI phantom

Reconstruction Type	**Maximum Value**	**Threshold (%)**
Full 60-s without motion artifacts	10117.1	50%
Full 60-s with motion artifacts	4878.36	70%
0.9375-s without motion correction	89.3416	60%
0.9375-s with motion correction	99.379	50%
0.9375-s with deblurring	0.579533	50%
Overlap without motion correction	84.8952	60%
Overlap with motion correction	100.499	50%
Overlap with deblurring	0.603093	50%

Table B.2: Threshold for Top Liver Lesion — low BMI phantom

Reconstruction Type	**Maximum Value**	**Threshold (%)**
Full 60-s without motion artifacts	11228.3	50%
Full 60-s with motion artifacts	6139.52	60%
0.9375-s without motion correction	93.6691	60%
0.9375-s with motion correction	130.433	50%
0.9375-s with deblurring	0.808978	50%
Overlap without motion correction	94.7764	60%
Overlap with motion correction	129.358	50%
Overlap with deblurring	0.867511	50%

Table B.3: Maximum Value for Top Lung lesion — low BMI phantom

Reconstruction Type	**Maximum Value**
Full 60-s without motion artifacts	2016.72
Full 60-s with motion artifacts	1801.43
0.9375-s without motion correction	23.828
0.9375-s with motion correction	25.314
0.9375-s with deblurring	0.153851
Overlap without motion correction	26.1477
Overlap with motion correction	27.4434
Overlap with deblurring	0.166604

Table B.4: Maximum Value for Bottom Lung Lesion — low BMI phantom

Reconstruction Type	**Maximum Value**
Full 60-s without motion artifacts	1850.81
Full 60-s with motion artifacts	1619.69
0.9375-s without motion correction	34.1339
0.9375-s with motion correction	28.5646
0.9375-s with deblurring	0.146389
Overlap without motion correction	34.0497
Overlap with motion correction	27.9918
Overlap with deblurring	0.141329

B.2 Medium BMI phantom

The threshold values and the corresponding intensity maxima used in the two liver lesions are reported in Tables B.5 and B.6, while those for the lung lesions are reported in Tables B.7 and B.8.

Table B.5: Threshold for Bottom Liver Lesion — medium BMI phantom

Reconstruction Type	Maximum Value	Threshold (%)
Full 60-s without motion artifacts	10117.1	50%
Full 60-s with motion artifacts	4802.72	70%
Overlap without motion correction	72.9986	70%
Overlap with motion correction	80.7529	60%

Table B.6: Threshold for Top Liver Lesion — medium BMI phantom

Reconstruction Type	Maximum Value of ROI	Threshold (%)
Full 60-s without motion artifacts	11228.3	50%
Full 60-s with motion artifacts	5454.31	60%
Overlap without motion correction	83.0397	60%
Overlap with motion correction	109.002	50%

Table B.7: Maximum Value for Top Lung Lesion — medium BMI phantom

Reconstruction Type	Maximum Value of ROI
Full 60-s without motion artifacts	2016.72
Full 60-s with motion artifacts	1749.25
Overlap without motion correction	24.8809
Overlap with motion correction	26.6339

Table B.8: Maximum Value for Bottom Lung Lesion — medium BMI phantom

Reconstruction Type	Maximum Value of ROI
Full 60-s without motion artifacts	1850.81
Full 60-s with motion artifacts	1849.38
Overlap without motion correction	27.984
Overlap with motion correction	34.7466

B.3 High BMI phantom

The threshold values and corresponding maximum intensities used for the two liver lesions are reported in Tables B.9 and B.10, while the values for the lung lesions are shown in TablesB.11 and B.12.

Table B.9: Threshold for Bottom Liver Lesion — high BMI phantom

Reconstruction Type	Maximum Value	Threshold (%)
Full 60-s without motion artifacts	10117.1	50%
Full 60-s with motion artifacts	4551.33	70%
Overlap without motion correction	71.0184	70%
Overlap with motion correction	69.035	70%

Table B.10: Threshold for Top Liver Lesion — high BMI phantom

Reconstruction Type	Maximum Value	Threshold (%)
Full 60-s without motion artifacts	11228.3	50%
Full 60-s with motion artifacts	5334.51	70%
Overlap without motion correction	77.5884	70%
Overlap with motion correction	91.2903	60%

Table B.11: Maximum Value for Top Lung Lesion — high BMI phantom

Reconstruction Type	Maximum Value
Full 60-s without motion artifacts	2016.72
Full 60-s with motion artifacts	1272.43
Overlap without motion correction	19.1384
Overlap with motion correction	20.1615

Table B.12: Maximum Value for Bottom Lung Lesion — high BMI phantom

Reconstruction Type	Maximum Value
Full 60-s without motion artifacts	1850.81
Full 60-s with motion artifacts	1078.82
Overlap without motion correction	20.6045
Overlap with motion correction	25.8886

Bibliography

[1] Fahim Ul-Hassan and Gary J Cook. “PET/CT in oncology”. English. In: *Clinical Medicine* 12.4 (Aug. 2012), pp. 368–72. ISSN: 1470-2118. DOI: 10.7861/clinmedicine.12-4-368 (cit. on pp. 1–4).

[2] Katherine Lameka, Michael D. Farwell, and Masanori Ichise. “Chapter 11 - Positron Emission Tomography”. In: *Neuroimaging Part I*. Ed. by Joseph C. Masdeu and R. Gilberto González. Vol. 135. Handbook of Clinical Neurology. Elsevier, 2016, pp. 209–227. DOI: https://doi.org/10.1016/B978-0-444-53485-9.00011-8. URL: https://www.sciencedirect.com/science/article/pii/B9780444534859000118 (cit. on pp. 1, 3, 4).

[3] Dennis R Schaart. “Physics and technology of time-of-flight PET detectors”. In: *Physics in Medicine & Biology* 66.9 (2021), 09TR01 (cit. on pp. 1, 5).

[4] Riemer HJA Slart, Charalampos Tsoumpas, Andor WJM Glaudemans, Walter Noordzij, Antoon TM Willemsen, Ronald JH Borra, Rudi AJO Dierckx, and Adriaan A Lammertsma. “Long axial field of view PET scanners: a road map to implementation and new possibilities”. In: *European journal of nuclear medicine and molecular imaging* 48.13 (2021), pp. 4236–4245 (cit. on pp. 1, 14).

[5] Stefaan Vandenberghe et al. “Walk-through flat panel total-body PET: a patient-centered design for high throughput imaging at lower cost using DOI-capable high-resolution monolithic detectors”. In: *European journal of nuclear medicine and molecular imaging* 50.12 (2023), pp. 3558–3571 (cit. on pp. 1, 15–17).

[6] James Wang, Dalton Bermudez, Weijie Chen, Divya Durgavarjhula, Caitlin Randell, Meltem Uyanik, and Alan McMillan. “Motion-correction strategies for enhancing whole-body PET imaging”. In: *Frontiers in Nuclear Medicine* 4 (2024), p. 1257880 (cit. on pp. 1, 18–24).

[7] Sean L Kitson, Vincenzo Cuccurullo, Andrea Ciarmiello, Diana Salvo, and Luigi Mansi. “Clinical applications of positron emission tomography (PET) imaging in medicine: oncology, brain diseases and cardiology”. In: *Current Radiopharmaceuticals* 2.4 (2009), pp. 224–253 (cit. on p. 2).

[8] Haojun Chen, Liang Zhao, Bing Hao, Long Sun, Orit Jacobson, and Hua Wu. “Comparison of 68Ga-FAPI and 18F-FDG PET/CT for detection, staging, and restaging of various kinds of cancer”. In: *Journal of Nuclear Medicine*

61.supplement 1 (2020), pp. 625–625. ISSN: 0161-5505. eprint: https://jnm.snmjournals.org/content. URL: https://jnm.snmjournals.org/content/61/supplement_1/625 (cit. on p. 2).

[9] Yassine Bouchareb, Afrah AlSaadi, Jawa Zabah, Anjali Jain, Aziza Al-Jabri, Peter Phiri, Jian Qing Shi, Gayathri Delanerolle, and Srinivasa Rao Sirasanagandla. "Technological advances in SPECT and SPECT/CT imaging". In: *Diagnostics* 14.13 (2024), p. 1431 (cit. on p. 3).

[10] Magdy M Khalil et al. *Basic science of PET imaging*. Tech. rep. Springer, 2017 (cit. on pp. 3–5, 11, 12).

[11] Astrid AM van der Veldt, Egbert F Smit, and Adriaan A Lammertsma. "Positron emission tomography as a method for measuring drug delivery to tumors in vivo: the example of [11C] docetaxel". In: *Frontiers in oncology* 3 (2013), p. 208 (cit. on p. 3).

[12] Helge Kragh. "Rutherford, radioactivity, and the atomic nucleus". In: *arXiv preprint arXiv:1202.0954* (2012) (cit. on p. 3).

[13] THOMAS LEWELLEN and JOEL KARP. "I. BASIC POSITRON EMISSION TOMOGRAPHY PRINCIPLES". In: () (cit. on pp. 4, 6–8).

[14] Simon R Cherry, Magnus Dahlbom, Simon R Cherry, and Magnus Dahlbom. *PET: physics, instrumentation, and scanners*. Springer, 2006 (cit. on pp. 5–10).

[15] Shan Tong, Adam M Alessio, and Paul E Kinahan. "Image reconstruction for PET/CT scanners: past achievements and future challenges". In: *Imaging in medicine* 2.5 (2010), p. 529 (cit. on pp. 8–10).

[16] Amirreza Mahbod and Eleni Tsakiraki. "Comparison of FBP and iterative methods". In: *Royal Institute of Technology* (2015) (cit. on pp. 8–10).

[17] Geoffrey Currie, Johnathan Hewis, and Stewart Bushong. "Tomographic reconstruction: a nonmathematical overview". In: *Journal of Medical Imaging and Radiation Sciences* 46.4 (2015), pp. 403–412 (cit. on p. 9).

[18] Elaine H Wacholtz. "History and Development of PET". In: *ECEI, CEwebsources. http://www. cewebsource. com/coursePDFs/historyofPET. pdf (page consultée le 22 Février 2012)* (2011) (cit. on p. 12).

[19] Clemens Mingels et al. "Total-body PET/CT or LAFOV PET/CT? Axial field-of-view clinical classification". In: *European journal of nuclear medicine and molecular imaging* 51.4 (2024), pp. 951–953 (cit. on pp. 13, 14).

[20] Antonia Dimitrakopoulou-Strauss, Leyun Pan, and Christos Sachpekidis. "Long axial field of view (LAFOV) PET-CT implementation in static and dynamic oncological studies". In: *European Journal of Nuclear Medicine and Molecular Imaging* 50.11 (2023), pp. 3354–3362 (cit. on pp. 13, 14).

[21] Christos Sachpekidis and Antonia Dimitrakopoulou-Strauss. "Long axial field-of-view (LAFOV) PET/CT in prostate cancer". In: *Seminars in Nuclear Medicine*. Elsevier. 2024 (cit. on p. 13).

[22] Ian Alberts et al. “Clinical performance of long axial field of view PET/CT: a head-to-head intra-individual comparison of the Biograph Vision Quadra with the Biograph Vision PET/CT”. In: *European journal of nuclear medicine and molecular imaging* 48 (2021), pp. 2395–2404 (cit. on pp. 13, 14).

[23] Benjamin A Spencer et al. “Performance evaluation of the uEXPLORER total-body PET/CT scanner based on NEMA NU 2-2018 with additional tests to characterize PET scanners with a long axial field of view”. In: *Journal of Nuclear Medicine* 62.6 (2021), pp. 861–870 (cit. on p. 14).

[24] Stephen Pheasant and Christine M Haslegrave. *Bodyspace: Anthropometry, ergonomics and the design of work*. CRC press, 2018 (cit. on p. 15).

[25] WT-PET. *Immagine prelevata da WT-PET website*. Accessed: 2025-05-07. 2025. URL: `https://www.wt-pet.org/` (cit. on p. 16).

[26] Rabia Aziz, Jens Maebe, Florence Marie Muller, Yves D’Asseler, and Stefaan Vandenberghe. “Quantitative analysis of patient motion in walk-through PET scanner and standard axial field of view pet scanner using infrared-based tracking”. In: *EJNMMI physics* 11.1 (2024), p. 99 (cit. on p. 16).

[27] Chad RRN Hunter, Ran Klein, Rob S Beanlands, and Robert A deKemp. “Patient motion effects on the quantification of regional myocardial blood flow with dynamic PET imaging”. In: *Medical physics* 43.4 (2016), pp. 1829–1840 (cit. on p. 18).

[28] Sadek A Nehmeh and Yusuf E Erdi. “Respiratory motion in positron emission tomography/computed tomography: a review”. In: *Seminars in nuclear medicine*. Vol. 38. 3. Elsevier. 2008, pp. 167–176 (cit. on pp. 19–24).

[29] David Henry, Roger Fulton, Julian Maclaren, Murat Aksoy, Roland Bammer, and Andre Kyme. “Close-range feature-based head motion tracking for MRI and PET-MRI”. In: *2018 IEEE Nuclear Science Symposium and Medical Imaging Conference Proceedings (NSS/MIC)*. IEEE. 2018, pp. 1–3 (cit. on p. 20).

[30] Severin Ionut-Cristian and Dobrea Dan-Marius. “Using inertial sensors to determine head motion—A review”. In: *Journal of Imaging* 7.12 (2021), p. 265 (cit. on p. 20).

[31] H William Strauss et al. “Procedure guideline for myocardial perfusion imaging 3.3”. In: *Journal of Nuclear Medicine Technology* 36.3 (2008), pp. 155–161 (cit. on p. 20).

[32] Chengyu Shi, Xiaoli Tang, and Maria Chan. “Evaluation of the new respiratory gating system”. In: *Precision radiation oncology* 1.4 (2017), pp. 127–133 (cit. on p. 20).

[33] Eero Lehtonen, Jarmo Teuho, Juho Koskinen, Mojtaba Jafari Tadi, Riku Klén, Reetta Siekkinen, Joaquin Rives Gambin, Tuija Vasankari, and Antti Saraste. "A respiratory motion estimation method based on inertial measurement units for gated positron emission tomography". In: *Sensors* 21.12 (2021), p. 3983 (cit. on p. 21).

[34] Thomas Ersepke, Florian Büther, Mirco Heß, and Klaus P Schäfers. "A contactless approach for respiratory gating in PET using continuous-wave radar". In: *Medical Physics* 42.8 (2015), pp. 4911–4919 (cit. on p. 21).

[35] Chen Sun et al. "An objective evaluation method for head motion estimation in PET—motion corrected centroid-of-distribution". In: *Neuroimage* 264 (2022), p. 119678 (cit. on p. 22).

[36] PJ Schleyer, JT Dunn, S Reeves, S Brownings, PK Marsden, and K Thielemans. "Detecting and estimating head motion in brain PET acquisitions using raw time-of-flight PET data". In: *Physics in Medicine & Biology* 60.16 (2015), p. 6441 (cit. on p. 22).

[37] Tianyi Zeng, Jiazhen Zhang, Enette Revilla, Eléonore V Lieffrig, Xi Fang, Yihuan Lu, and John A Onofrey. "Supervised deep learning for head motion correction in PET". In: *International Conference on Medical Image Computing and Computer-Assisted Intervention*. Springer. 2022, pp. 194–203 (cit. on p. 22).

[38] Lalith Kumar Shiyam Sundar et al. "Conditional generative adversarial networks aided motion correction of dynamic 18F-FDG PET brain studies". In: *Journal of Nuclear Medicine* 62.6 (2021), pp. 871–879 (cit. on p. 23).

[39] Spencer Manwell, Ran Klein, Tong Xu, and Robert A deKemp. "Clinical comparison of the positron emission tracking (PeTrack) algorithm with the real-time position management system for respiratory gating in cardiac positron emission tomography". In: *Medical Physics* 47.4 (2020), pp. 1713–1726 (cit. on p. 23).

[40] Sadek A Nehmeh, Yusuf E Erdi, Gustavo SP Meirelles, Olivia Squire, Steven M Larson, John L Humm, and Heiko Schöder. "Deep-inspiration breath-hold PET/CT of the thorax". In: *Journal of Nuclear Medicine* 48.1 (2007), pp. 22–26 (cit. on p. 23).

[41] Joseph G Meier, Carol C Wu, Sonia L Betancourt Cuellar, Mylene T Truong, Jeremy J Erasmus, Samuel A Einstein, and Osama R Mawlawi. "Evaluation of a novel elastic respiratory motion correction algorithm on quantification and image quality in abdominothoracic PET/CT". In: *Journal of Nuclear Medicine* 60.2 (2019), pp. 279–284 (cit. on p. 23).

[42] J Michael Fitzpatrick, Derek LG Hill, Calvin R Maurer, et al. "Image registration". In: *Handbook of medical imaging* 2 (2000), pp. 447–513 (cit. on pp. 25–27).

[43] Medha V Wyawahare, Pradeep M Patil, Hemant K Abhyankar, et al. "Image registration techniques: an overview". In: *International Journal of Signal Processing, Image Processing and Pattern Recognition* 2.3 (2009), pp. 11–28 (cit. on p. 26).

[44] J-Donald Tournier et al. "MRtrix3: A fast, flexible and open software framework for medical image processing and visualisation". In: *Neuroimage* 202 (2019), p. 116137 (cit. on p. 28).

[45] David Raffelt, J-Donald Tournier, Jurgen Fripp, Stuart Crozier, Alan Connelly, and Olivier Salvado. "Symmetric diffeomorphic registration of fibre orientation distributions". In: *Neuroimage* 56.3 (2011), pp. 1171–1180 (cit. on p. 28).

[46] David A Raffelt, J-Donald Tournier, Robert E Smith, David N Vaughan, Graeme Jackson, Gerard R Ridgway, and Alan Connelly. "Investigating white matter fibre density and morphology using fixel-based analysis". In: *Neuroimage* 144 (2017), pp. 58–73 (cit. on p. 28).

[47] MRtrix3 Developers. *mrregister command reference*. `https://mrtrix.readthedocs.io/en/latest/reference/commands/mrregister.html`. Accessed: April 29, 2025. 2024 (cit. on p. 28).

[48] Brian B Avants, Nick Tustison, Gang Song, et al. "Advanced normalization tools (ANTS)". In: *Insight j* 2.365 (2009), pp. 1–35 (cit. on pp. 29, 30, 77).

[49] Derek LG Hill, Philipp G Batchelor, Mark Holden, and David J Hawkes. "Medical image registration". In: *Physics in medicine & biology* 46.3 (2001), R1 (cit. on p. 29).

[50] Karine Assie et al. "Monte Carlo simulation in PET and SPECT instrumentation using GATE". In: *Nuclear Instruments and Methods in Physics Research Section A: Accelerators, Spectrometers, Detectors and Associated Equipment* 527.1-2 (2004), pp. 180–189 (cit. on p. 31).

[51] Sébastien Jan et al. "GATE: a simulation toolkit for PET and SPECT". In: *Physics in Medicine & Biology* 49.19 (2004), p. 4543 (cit. on p. 32).

[52] Thibaut Merlin, Simon Stute, Didier Benoit, Julien Bert, Thomas Carlier, Claude Comtat, Marina Filipovic, Frédéric Lamare, and Dimitris Visvikis. "CASToR: a generic data organization and processing code framework for multi-modal and multi-dimensional tomographic reconstruction". In: *Physics in Medicine & Biology* 63.18 (2018), p. 185005 (cit. on p. 33).

[53] Jens Maebe. "Timing Capabilities and Image Reconstruction for the Walk-Through PET: A Large Flat-Panel PET System with Monolithic Detectors". PhD thesis. Ghent University, 2024 (cit. on pp. 33, 34).

[54] Andreas Markus Loening and Sanjiv Sam Gambhir. "AMIDE: a free software tool for multimodality medical image analysis". In: *Molecular imaging* 2.3 (2003), p. 15353500200303133 (cit. on p. 36).

[55] Akanksha Bali and Shailendra Narayan Singh. "A review on the strategies and techniques of image segmentation". In: *2015 Fifth international conference on advanced computing & communication technologies*. IEEE. 2015, pp. 113–120 (cit. on pp. 36, 37).

[56] Song Yuheng and Yan Hao. "Image segmentation algorithms overview". In: *arXiv preprint arXiv:1707.02051* (2017) (cit. on p. 37).

[57] Silje Kjærnes Øen, Lars Birger Aasheim, Live Eikenes, and Anna Maria Karlberg. "Image quality and detectability in Siemens Biograph PET/MRI and PET/CT systems—a phantom study". In: *EJNMMI physics* 6 (2019), pp. 1–16 (cit. on p. 38).

[58] Joshua D Schaefferkoetter, Jianhua Yan, Therese Sjöholm, David W Townsend, Maurizio Conti, John Kit Chung Tam, Ross A Soo, and Ivan Tham. "Quantitative accuracy and lesion detectability of low-dose 18F-FDG PET for lung cancer screening". In: *Journal of Nuclear Medicine* 58.3 (2017), pp. 399–405 (cit. on p. 39).

[59] MRtrix3 Developers. *MRtrix3 Documentation: `mrtransform`*. Accessed: 2025-04-30. 2025. URL: `https://mrtrix.readthedocs.io/en/dev/reference/commands/mrtransform.html` (cit. on p. 41).

[60] Gajanand Gupta et al. "Algorithm for image processing using improved median filter and comparison of mean, median and improved median filter". In: *International Journal of Soft Computing and Engineering (IJSCE)* 1.5 (2011), pp. 304–311 (cit. on p. 46).

[61] Andrea Gallamini, Colette Zwarthoed, and Anna Borra. "Positron emission tomography (PET) in oncology". In: *Cancers* 6.4 (2014), pp. 1821–1889 (cit. on p. 47).

[62] Pooja Satish, Mallikarjunaswamy Srikantaswamy, and Nataraj Kanathur Ramaswamy. "A Comprehensive Review of Blind Deconvolution Techniques for Image Deblurring." In: *Traitement du Signal* 37.3 (2020) (cit. on p. 52).

[63] Xiao Jin, Chung Chan, Tim Mulnix, Vladimir Panin, Michael E Casey, Chi Liu, and Richard E Carson. "List-mode reconstruction for the Biograph mCT with physics modeling and event-by-event motion correction". In: *Physics in Medicine & Biology* 58.16 (2013), p. 5567 (cit. on p. 74).

[64] Yihuan Lu et al. "Deep learning-aided respiratory motion compensation in PET/CT: addressing motion induced resolution loss, attenuation correction artifacts and PET-CT misalignment". In: *European Journal of Nuclear Medicine and Molecular Imaging* (2024), pp. 1–12 (cit. on p. 74).

[65] Concept Note. *Sustainable development goals*. 2020 (cit. on p. 75).